Coupling of Rydberg atoms to a superconducting coplanar waveguide resonator for a quantum memory device

Dissertation
der Mathematisch-Naturwissenschaftlichen Fakultät
der Eberhard Karls Universität Tübingen
zur Erlangung des Grades eines
Doktors der Naturwissenschaften
(Dr. rer. nat.)

vorgelegt von
Li Yuan Ley
aus Johor Bahru, Malaysia

Tübingen
2018

For the generous helping in my academia research

Mirco Siercke, Helge Hatterman

For the providing of opportunity into coming to Tübingen

Rainer Dumke, József Fortágh

The people of significance in my life

Abstract

This thesis intends to describe the progress in experimental contribution regarding the physical realization of quantum information storage using hybrid systems of ultracold atoms and superconducting microwave resonators.

Ultracold atoms in their ground states are well-isolated quantum systems offering long coherence times. Hence, ensembles of trapped atoms coupling with on-chip microwave resonators are considered as promising systems for the realization of quantum memories. Here, we demonstrate the coupling of magnetically trapped ultracold ^{87}Rb ground state atoms to a coherently driven superconducting coplanar waveguide resonator. When driving the cavity in resonance with the atomic transition, we observed Rabi oscillations between hyperfine states. This showed the capability in coherent controlling of the atomic states through the cavity field. When driving the cavity off-resonance with the atomic transition, the AC stark shift is observed. This showed the microwave field strength in the cavity seen by atoms.

Strong interaction strength of Rydberg atoms in the microwave transition regime has been proposed as an interface during quantum memory writing. Here, we describe the implementation of a Rydberg system into our experimental setup, using two photon excitation for Rydberg atoms creation and field ionization for detection. Stray electric fields on the chip surface are observed and quantified using means of electromagnetically induced transparency. Lastly via weakly driving the resonator, we are capable of achieving transitions between neighboring Rydberg states.

Zusammenfassung

In dieser Arbeit soll der Beitrag des Autors zur experimentellen Realisierung eines hybriden Systems aus ultrakalten Atomen und supraleitenden Resonatoren zur Speicherung von Quanteninformation beschrieben werden.

Ultrakalte Atome im Grundzustand sind isolierte Quantensysteme und ermögliche lange Kohärenzzeiten. Daher werden magnetisch gefangen atomare Ensembles, die mit Mikrowellenresonatoren auf einem Chip gekoppelt werden, als vielversprechende Kanditaten für die Realisation von Quantenspeichern gesehen. Als wichtiger Schritt dahin wird in dieser Arbeit die magnetische Kopplung von ^{87}Rb Atomen an einen supraleitenden Resonator auf der Basis koplanarer Streifenleitung demonstriert. Wenn der Resonator bei der atomaren Resonanzfrequenz getrieben wird, werden Rabi-Oszillationen zwischen atomaren Hyperfeinzuständen beobachtet. Dadurch wird die Möglichkeit aufgezeigt, den Zustand der Atome kohärent durch den Resonator zu kontrollieren. Wird der Resonator hingegen nicht-resonant mit den Atomen getrieben, werden die atomaren Energiezustände durch den AC-Zeeman-Effekt verschoben. Damit lässt sich die Stärke des Mikrowellenfeldes im Resonator rekonstruieren.

Aufgrund ihrer starken Wechselwirkung mit Mikrowellenfeldern wurde vorgeschlagen, Rydberg-Atome als Schnittstelle für einen Quantenspeicher zu verwenden. Im zweiten Teil der Arbeit wird die Implementierung von Rydberg-Atomen im experimentellen Aufbau beschrieben. Rydberg-Zustände werden durch Zwei-Photon-Anregung erzeugt und durch selektive Feldionisation nachgewiesen. Elektrische Störfelder, die durch die Chipoberfläche verursacht werden, werden mit Hilfe elektromagnetisch induzierter Transparenz vermessen. Indem der Resonator schwach mit einer Mikrowelle getrieben wird, ist es letztlich gelungen, Übergänge zwischen benachbarten Rydberg-Zuständen nachzuweisen.

Contents

"I think there is a world market for maybe five computers."

Thomas J. Watson, CEO of IBM, 1943

Chapter 1

Introduction

1.1 From classical to quantum computing

The year was 1936: Alan Turing, in need of a fast computational method for German naval cryptanalysis of the Enigma machine [1], invented the first abstract mathematical notion of a classical computer - known as *Turing machine* [2]. Constructed mechanically, a universal Turing machine [3] can accomplish everything that an actual computer can achieve. Nevertheless, it proves fundamental limitations on the power of mechanical computation [4].

During the year 1945, John von Neumann described the design architecture for electronic digital computer - known as *Von Neumann architecture* [5]. Where processing unit (CPU), memory unit (RAM), storing unit (hard disk), input and output devices (keyboard, monitor screen...) connected via bus are assembled into a universal Turing machine. Development of computer hardware and electronic components advanced in astonishing pace and ever since then [6], every modern day classical computer is designed with Von Neumann architecture.

Classical computers truly revolutionized the world of mankind [7]. It is however far from being perfect. In classical computing, information is stored in bits. Bits can only exist either in 1 or 0, corresponding to on or off state of tiny transistor switches inside the processing unit [8]. One bit has to be process before leaving space to other new bits for operation. This caused classical computing to be highly inefficient in dealing with huge databases [9], making computing processes such as simulation and prediction a lengthy process, and for most of the case not even practical. So the question remains, whether it is possible to find a computing method to solve this problem.

The year was 1982: Richard Feynman proposed an ingenious method in resolving the problem [10]. He conjectured that by exploiting quantum mechanical properties of superposition states, quantum bits or qubits substitution of classical bits will speed up the process of computing. Unlike classical bits, qubits can exist in superposition state of 1 and 0, meaning they can be in multiple states at once [11]. This exhibits inherent parallelism, making quantum computers capable in processing multiple of bits [12], hence information at the same time.

The concept was then further enhanced and universal quantum computer description was presented by David Deutsch in the year 1985 [13]. Together with

development of quantum algorithms [14], quantum computing provide an exponential speed-up compared to the classical computing for various complex problems[1]. For some famous examples: The Deutsch–Jozsa algorithm [16] and Simon's algorithm [17] for black-box problem solving, Shor's algorithm [18] for solving discrete logarithm problems and the integer factorization problems, Grover's algorithm [19] for searching in unstructured databases, and the HHL algorithm [20] for solving systems of linear equations.

The year is 2018: Development of quantum computing as devices is still in its infancy [21]. Practical and theoretical research continues, and involves even national agencies and IT companies [22]. Eventually, the day will come when quantum computers will be able to solve problems efficiently, which are not practically feasible on classical computers. Be prepared.

1.2 The qubit pageant

Any two level quantum system that can be prepared in a superposition state in principle can be a qubit candidate. They have to retain the quantum information long enough such that quantum logic operation can be performed, implicating that the qubit coherent time has to be long enough. This requires qubit to not interact strongly with their surroundings. However, qubits that are isolated from their environments are hard to manipulate. Therefore, it is crucial to find a quantum system that interacts strongly enough so that it can be easily controlled, yet weak enough to have adequate coherence time.

During the past two decades, a range of candidates has appeared to be quite promising [23]. The first to appear was the use of trapped ions [24–28], for which the first quantum logic gate was proposed and experimentally realized in 1995 [29,30]. A trapped ion system is also scalable with the record of 14 entangled ions [31]. Then, using nuclear magnetic spin states of molecules in room temperature liquid [32], researchers successfully implemented Deutsch's quantum algorithm [33] and Shor's algorithm [34]. All optical quantum computing also emerged, using polarization of photons as qubits [35–38]. Semiconductor qubits also had been in the spotlight for couple of years [39–41]. The approach using Rydberg atoms with long dipole-dipole interaction had been also implemented for quantum gates, and entanglement [42–50]. Nitrogen vacancy with long coherence time in room temperature attracted lots of attention ever since [51,52]. Last but not least, superconducting qubits have been the favorite for the many [53–56]. This includes big companies like IBM, Google, Intel and Microsoft [57].

Only time can tell which type of qubit will ultimately be the winner. For now, superconducting qubits are leading [58]. Mainly because it can be strongly coupled to microwave coplanar waveguide resonator [59–61], which can be easily addressed (write in, read out) [62] individually via microwave. Entanglement between superconducting qubits can be done easily using microwave coplanar waveguide as quantum bus [53,63]. In addition, the field for microwave technology [64] and method

---

[1]A quantum computer with n qubits is simultaneously comparable to a classical computer of 2^n bits. [15]

for superconducting chip fabrication [65] is already well established and matured.

However, this is far from being good. To be a good quantum computing device, it has to be capable of scaling to more qubits, and also each qubit has to establish a decent coherence time [66]. For now, the state of the art controllable superconducting qubit is demonstrated up to only sixteen at a time [67], and with a coherence time of just 200μs [68, 69]. Additionally, the mKelvin environment required for controlling superconducting qubits was proven to be hard to maintain and limits potential up-scaling [70]. The problem of short coherence time can be overcome by implementation of quantum memory, we will talk more about quantum memory in the next section.

1.3   Quantum memory

The requirement of a controllable qubit also resulted in the interaction of its surrounding, leading to short coherence time. It is therefore necessary to find another quantum system that stores information on a longer timescale, acting as a memory device [71, 72]. There are other two level quantum systems that interact very weakly with their environment [73]. These isolated systems are ideal for quantum information storing with their long coherence time. However, with their nature of being isolated, it is difficult for the qubits to send quantum information into these systems.

The solution required a common quantum bus, usually a resonator, which acts as a bridge between qubits and the quantum memory device [74]. Each of them (qubits and quantum memory) has to couple strongly with the quantum bus. Therefore, information from the qubit can be passed to the bus and then to the memory and vice versa [75, 76], similar with its classical computer counterpart.

Several different approaches have been shown to create such a coupling between quantum memory devices and a quantum bus. Researchers have demonstrated strong coupling between a superconducting resonator and nitrogen vacancy(NV) centers diamond [77–79]. It was also shown that information of NV center can be stored much longer (1s) inside a nuclear spin [80]. Other strong coupling examples include: The spin of ions in solid states [81] and polar molecules coupling with microwave resonator [82, 83]. Also, the coupling of neutral atoms to optical cavity [84–86] and 3D microwave cavity [87, 88]. Last but not least, the coupling of atoms and NV centers with mechanical oscillator [89, 90].

As mentioned in the last section, the best qubit candidate so far is the superconducting qubits, which is strongly coupled to a coplanar waveguide microwave resonator [91]. It would be therefore desirable for a given quantum memory to strongly couple to coplanar waveguide resonator too [92], creating a hybrid quantum computer system [93–96].

1.4   Atom-resonator coupling

It had been shown that ^{87}Rb atom can be magnetically trapped into a superconducting [97–100] coplanar resonator structure via persistent currents [101–104]. Trapped

$14\mu m$ above the resonator structure at liquid helium temperature, they exhibit a long coherence time of 4s [105][2]. This is still the record holder among all other quantum memory candidates. With an atomic transition frequency in the GHz range [110] similar to superconducting qubits, they are the ideal candidate for quantum memory. In addition to that, the rich energy structure of ^{87}Rb also provides the possibility to convert information from microwave photons to optical photons [84,111] required for quantum communication [112–114]. Here, optical photons that have much less attenuation as compared to microwaves are sent over longer distances.

Light naturally bounces between mirrors, making photons remain inside the resonator. This however will not go on indefinitely, photons will eventually escape the resonator or get absorbed by the medium with a cavity decay rate κ. A resonator is quantified by a quality factor Q, where a higher Q factor signifies longer photons lifetime, thus lower cavity decay rate κ. Strong coupling is said to be achieved if the quantum system (in our case ^{87}Rb) is able to interact with photons within the resonator before they escape. This is measured in coupling strength g. Hence, for strong coupling we need $g > \kappa, \Gamma$. Where Γ is the atomic decay rate [115].

The ^{87}Rb atoms have a ground-state hyperfine splitting energy level at 6.834GHz [110]. The energy levels interact with photons via a magnetic dipole transition, with magnetic coupling strength $g_B = \mu_b \cdot B = \mu_b \cdot \frac{E}{c}$. Here, μ_b is the Bohr magneton, B and E are the corresponding magnetic and electric amplitudes of the electromagnetic waves. This is far too weak to fulfill the condition of strong coupling. Even with collective coupling effect of $g\sqrt{N}$, it is estimated that one needs a very large atom number $N \sim 10^6$ trapped at distance of few μm to a low loss resonator with $Q \sim 10^6$ to reach strong coupling regime [116]. This cannot be realized experimentally yet, since trapping of such a large atom number within μm on a surface is technically demanding, and a Q factor of 10^6 can only be achieved at mKelvin temperatures.

On the other hand, the Rydberg transition states of ^{87}Rb atoms also fall in the GHz range [117]. Transitions between two neighboring Rydberg states($|nS\rangle \rightarrow |nP\rangle$) are based on the electric dipole interactions with electric coupling strength $g_E = n^2 a_o e \cdot E$. Here, n is the principle quantum number of the Rydberg state, a_o is the Bohr radius, e is the electron charge, and E is the electric amplitudes of the electromagnetic waves. For $n = 50$, this results in 6 orders of magnitude increase in interaction strength, making strong coupling possible [118]. However, highly excited Rydberg states are prompting to interact strongly with surrounding E-fields and MW radiation [119]. Also with lifetime of only $\sim 100\mu s$ [120,121], they are not an ideal quantum memory candidates.

Fortunately, with the help of coherent excitation/de-excitation with lasers [122], we are able to make good use of both the long coherence time of ^{87}Rb ground-states and high interaction strengths of its Rydberg states. The advantages of lasers is that they act as a quantum memory switch. The main idea for the quantum information storing process [75, 123, 124] is as follows. During the memory storing, lasers are first used to coherently excite the ^{87}Rb ground-state to a Rydberg state [125–127]. During the lifetime of the Rydberg state, information is released from qubits via photons. The photons then travel along the quantum bus (resonator), and are soon absorbed by Rydberg atom. After that, other lasers are used to coherently de-

---

[2]Other experiments regarding coherence of neutral atoms [106–109].

excites the Rydberg state to the ground-state again. Coherent process assure that information transfered from qubits to ^{87}Rb ground-state.

The importance for the work of this thesis is the ambition to strongly couple Rydberg atoms to a superconducting coplanar waveguide microwave resonator, using atoms as a quantum memory device. This will therefore help in the development of a hybrid quantum computer, making a functioning quantum computer a much more achievable goal.

1.5   Organization of thesis

This thesis is separated into three main categories: First, the author will introduce the atom chip on which the resonator is located. The characterization of the resonator is then discussed. Secondly, using methods of resonant Rabi oscillation and off-resonant MW dressing, the author describes the realization of weak coupling between ^{87}Rb ground-states and the resonator. Lastly, the implementation of Rydberg atoms and its consequences are explained, and the feasibility of MW transitions between neighboring Rydberg states is shown.

Chapter 2

Superconducting Coplanar Waveguide(CPW) Resonator Atom Chip

In this chapter, the atom chip used in the experiment will be further discussed. This chip was designed by Daniel Bothner, Benedikt Ferdinand and Dominik Wiedmayer from the solid state group of Prof. Reinhold Kleiner and Prof. Dieter Koelle, the author takes no part in designing and manufacturing. Hence, more details regarding chip design parameter and fabrication can be obtained at the Appendix B.

In essence, this chip was designed with two purposes in mind. The first is to provide a magnetic trap for trapping and manipulation of neutral atoms [128, 129]. The second is the integration of a CPW resonator, where atom-cavity coupling would takes place.

The theory of atomic chip traps in particular Z-trap, and CPW resonator have long been formulated and are well understood. Hence, it would not be further elaborated and the reader is expected to have basic understanding regarding these topics. Interested readers are advised to read references [130–132].

2.1   Chip Layout

The atom chip is based on the combination of two structures, a superconducting Z-wire, and a superconducting coplanar waveguide resonator with dimension designed such that the resonance frequency is close to the ^{87}Rb ground state hyperfine splitting ($\omega_{\text{Res}} \sim 6.85$GHz) and with a characteristic impedance of 50Ω. Both structures are patterned on top of a sapphire substrate. Niobium is used for the parts that are required to be superconducting, otherwise gold is used for electrical conduction. The chip layout is shown in Figure 2.1. Schematics of the atom trapping region are shown in Figure 2.2.

Previously, it was observed that there are strong parasitic resonances in the CPW cavity if parts of the chip are not grounded electrically. Hence here, the entire chip is grounded with either Niobium or gold. For some areas, gold is preferred due to the experimental procedure; An atomic cloud is guided via optical dipole trap from one side of the chip into the Z-trap. For this regions, gold is a better choice since
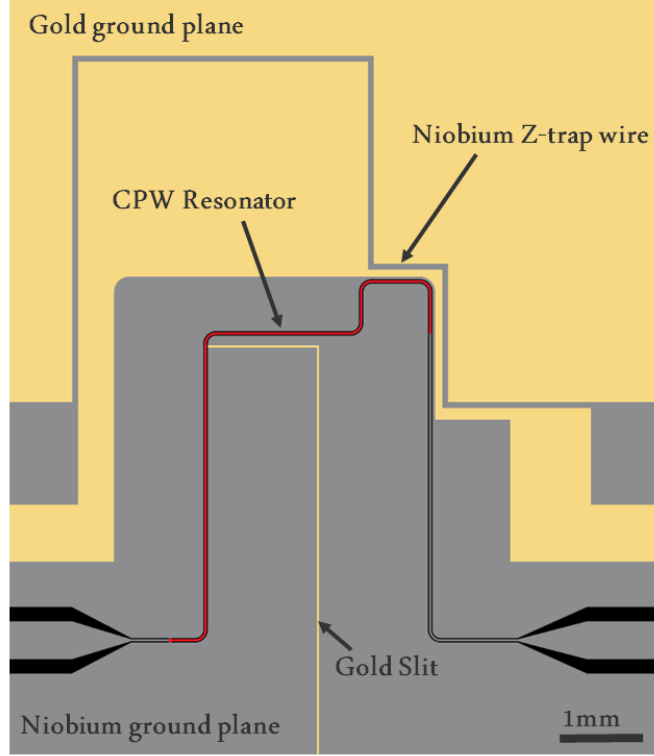
Figure 2.1: Top view of the superconducting atom chip: Consisting of a Z-trap wire and a coplanar waveguide(CPW) resonator with fundamental mode $\omega_{\mathrm{Res}} \sim 6.85\mathrm{GHz}$. The center conductor of CPW resonator is marked with the color red. The entire chip is electrically grounded with either Niobium or Gold planes.

superconducting Niobium will create unwanted magnetic field distortions due to the Meissner effect [133]. Because of this undesirable magnetic field potential and its induced majorana spin flip loss, the atoms transfer efficiency into the Z-trap will be greatly reduced. The remaining area which are not involved in the atom cloud transfer is grounded with superconducting Niobium to maximize the Q factor of the CPW resonator.

2.2   Cavity Parameters

The microwave resonator used on the chip is an inductively coupled half wavelength $\frac{\lambda}{2}$ transmission line cavity. The transmission line cavity length is $l_0 \sim 9.3\mathrm{mm}$ resulting in a fundamental mode resonance frequency at $\omega_{\mathrm{Res}} \sim 6.85\mathrm{GHz}$. It has a center conductor width of S=30μm and ground planes that are separated from the center conductor by a gap of W=16μm, targeting a characteristic impedance of Z=50Ω.

The input and output of the cavity are inductively coupled with two feedline connections between the center conductor and the ground plane, shown in figure 2.3. They are 36μm wide, 16μm long, and 4μm wide, 30μm long respectively. This gives a external resonator linewidth κ_{ex} due to losses of 7kHz and 141kHz (Refer to supplementary material in Appendix B for calculation), with external quality factor
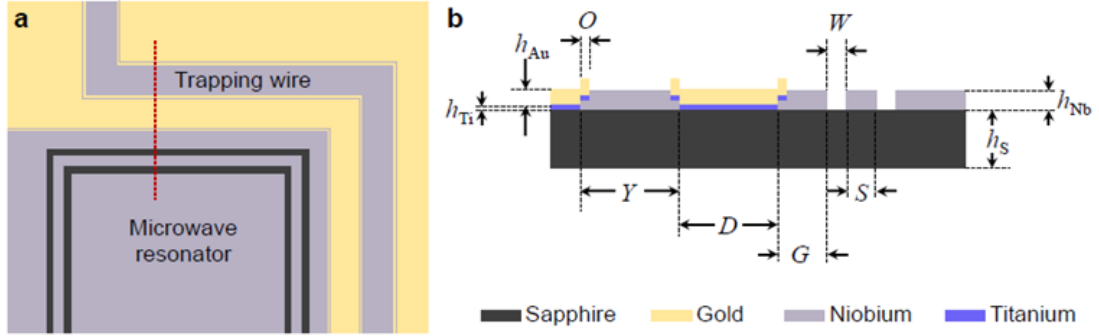
Label	Dimension
h_{Nb}	500nm
h_{Au}	400nm
h_s	330μm
h_{Ti}	4nm
O	10μm
W	16μm
Y	100μm
D	100μm
G	50μm
S	30μm

Figure 2.2: Atom chip layout and parameters: **a** Schematic top view of the trapping region of the atom chip. Z-trap wire and one end of the CPW resonator structure. Two structures are connected by a normal conducting gold layer to ensure a well define ground. **b** Cross sectional view along the red dotted line shown in **a**, depicting all relevant materials and parameters. Here, the Z-trap wire has a width Y=100μm. With the CPW resonator gap W=16μm and the center conductor S=30μm, CPW resonator impedance of 50Ω was achieved. Z-trap wire and CPW resonator was separated with gold layer with distance D=100μm and CPW ground plane G=50μm. To ensure good electrical contact, gold and niobium interfaces were overlapped with O=10μm. Niobium layers had a thickness h_{Nb}=500nm, and gold layers had a thickness h_{Au}=400nm. Thin layers of titanium h_{Ti}=4nm were used for better adhesion between gold layers and the Sapphire substrate, with thickness h_S=330μm.

of $Q = 5 \cdot 10^4$. It will show later in this chapter that the total Q measured is in the range of 10^3, indicating that the majority loss of MW photons is due to the internal quality factor, such as thermal quasiparticles in the superconductor and dissipation in the normal conducting part at the gold-niobium interface.

This can be easier understood with the analogy of an optical cavity, constructed with a damping medium in-between an input and output mirror of different reflectivity. In this case, input mirror has higher reflectivity than the output mirror. The output coupling is designed to be larger such that MW can only be transmitted from the cavity via the output port.
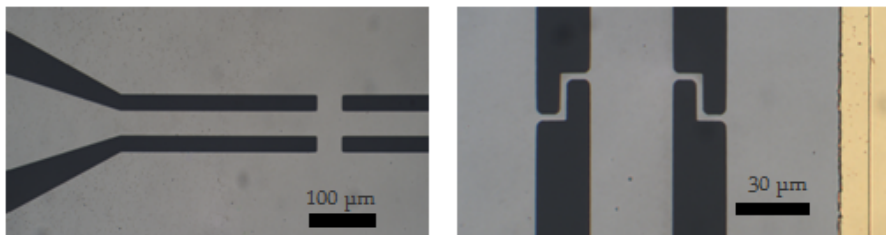

Figure 2.3: **On the left:** Image of the input coupling inductors for the CPW resonator with linewidth $\kappa_{\mathrm{ex}} = 7\mathrm{kHz}$. **On the right:** Image of the output coupling inductors with linewidth $\kappa_{\mathrm{ex}} = 141\mathrm{kHz}$. Refer text for details.

2.3 Installation of the Atom Chip into the Cold Finger Cryostat

The atom chip was glued to the atom chip holder with Cerasolzer as the adhesive component (adhesive to both sapphire and copper). Cerasolzer is an ideal candidate for good thermal conduction in cryogenic and ultra high vacuum environment. The atom chip holder served as the interface between the atom chip and the cold finger cryostat. It was manufactured from high grade copper for its excellent thermal conducting properties.

For gluing of the atom chip into the chip holder. First, the chip holder was heated with a hot plate to above the melting point of Cerasolzer (160c). At the meantime, a thin layer of Cerasolzer was applied under the atom chip with an ultrasonic soldering tip (Model: USS-9210). Then, the atom chip was put above the chip holder and heating of the hot plate was turned off. Cerasolzer in liquid state, then slowly solidified, creating a good affix for the atom chip and the chip holder.

It is crucial for the atom chip to have a well define ground potential. For electric ground conduction of the atom chip, the surrounding of the atom chip was grounded via direct contact with the chip holder. First, with ultra high vacuum (UHV) compatible conductive silver epoxy (EPO-TEK H20E) and then with wire bonding (Model: F&K delvotec NFO 09).

Electrical conducting wire and microwave cables for the Z-trap and resonator were then bonded into the atom chip. The wires were first soldered into a UHV

comparable printed circuit board (PCB) and then wire bonding was made for final connection to the atom chip. PCB was required for the ease of installation of the electrical connections. Wires were then secured with copper clamps and stress-relief grips. Figure 2.4 shown bellow is the chip holder with atom chip and cables attached.
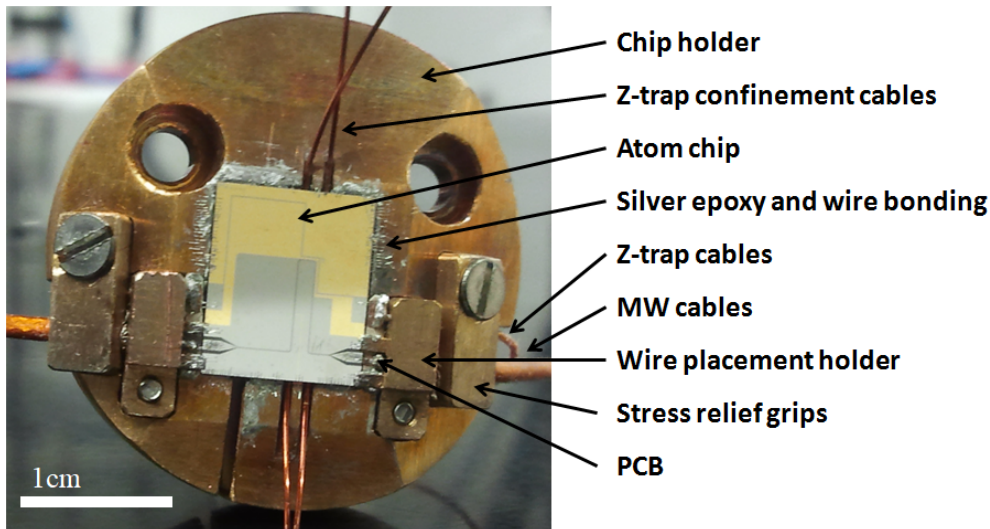

Figure 2.4: Image of the chip holder with atom chip and all the cables installed. Atom chip was glued to the chip holder with Cerasolzer and was electrically grounded by contact with silver epoxy and wire bonding to the chip holder. Two wires parallel to each other were put underneath the chip to give extra confinement for magnetic trapping of atoms (will be discuss in later chapter). Z-trap cables and MW cables were connected to the atom chip with a PCB acting as a buffer region for electrical connections. Cables were secured with holders and stress relief grips.

Thereafter, chip holder was secured to the cold finger extension with two M4 screws. A thin layer of indium was applied between the chip holder and the extension to facilitate thermal conduction. Finally, the whole assembly was attached to the cryostat.

2.4   Measurement of Cavity Properties

To quantify the properties of the CPW resonator: This includes transmission frequency, transmission linewidth and Q-factor. The transmission spectrum was measured with a network analyzer (E5071C ENA Vector Network Analyzer). The helium flow cryostat (Model ST-400, Janis research company) used was cooled to below Niobium critical temperature via continuous transfer of liquid helium-4 from a 100L storage tank. The temperature of the atom chip can be tuned by adjusting the flow rate of liquid helium and can be further stabilized with a cryogenic temperature controller (Model 340, Lakeshore company).

High MW attenuation inside the vacuum chamber was expected. It was estimated that the system had 10dB loss coming from the MW cables and a further 40dB loss from the atom chip's dielectric substrate. For this reason, a low noise

cryogenic amplifier (CITCRYO1-12A-1, Caltech microwave research group) was connected at the output of the CPW resonator for signal amplification purposes. For maximum amplification of 30dB, the drain voltage was set to V_D=1.2V and both the gate voltage at $V_{G1, G2}$=0.3V. Shown in figure 2.5.

Figure 2.5: Cryogenic low noise amplifier (CITCRYO1-12A-1, Caltech microwave research group) used in the setup. The amplifier was connected to the output of the CPW resonator. Due to the requirement of its cryogenic operating temperature, it was located ~5cm above the atom chip holder, attached on the side of the cold finger cryostat. For all cavity transmission measurements, the amplifier was set to maximum amplification of 30dB, with the drain voltage set to V_D=1.2V and both the gate voltage at $V_{G1, G2}$=0.3V.

Scheme of the CPW resonator transmission spectrum measurement setup was shown as following in figure 2.6. The CPW resonator and cryogenic low noise amplifier were located inside the vacuum chamber, with cryogenic temperature set by the Lakeshore temperature controller. Microwave were fed into the vacuum chamber via a pair of UHV Microwave feed-through. A Network analyzer generates MW signal and then analyzed the returned MW signal. Hence, by varying the MW frequency, the transmission properties of the CPW resonator can be characterized.

The transmissions profile of the cavity fundamental mode was shown in figure 2.7. Transmissions profile measured with the network analyzer were fitted with the Lorentz distribution (also known as Cauchy distribution):

$$f(\omega) = I\left[\frac{\kappa^2}{(\omega - \omega_{\mathrm{Res}})^2 + \kappa^2}\right] \tag{2.1}$$

Where I is the height of the transmission peak, κ is the linewidth of the cavity transmission, and ω_{Res} is the resonator resonant frequency. With κ and ω_{Res} known, Q factor can be calculated with equation Q $= \omega_{\mathrm{Res}}/\kappa$
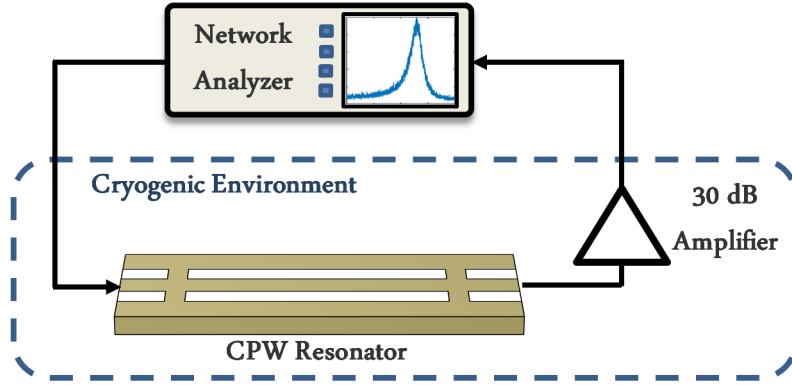
Figure 2.6: Scheme of the transmission measurement setup. The CPW resonator and the amplifier were kept in cryogenic environment inside the vacuum chamber. The temperature of the cryogenic environment was controlled and stabilized using a temperature controller (Model 340, Lakeshore company). Microwaves were fed into the system via a pair of UHV Microwave feed-through, with SMA interface. The transmission properties of the CPW resonator then were characterized by the network analyzer (Model: E5071C ENA).
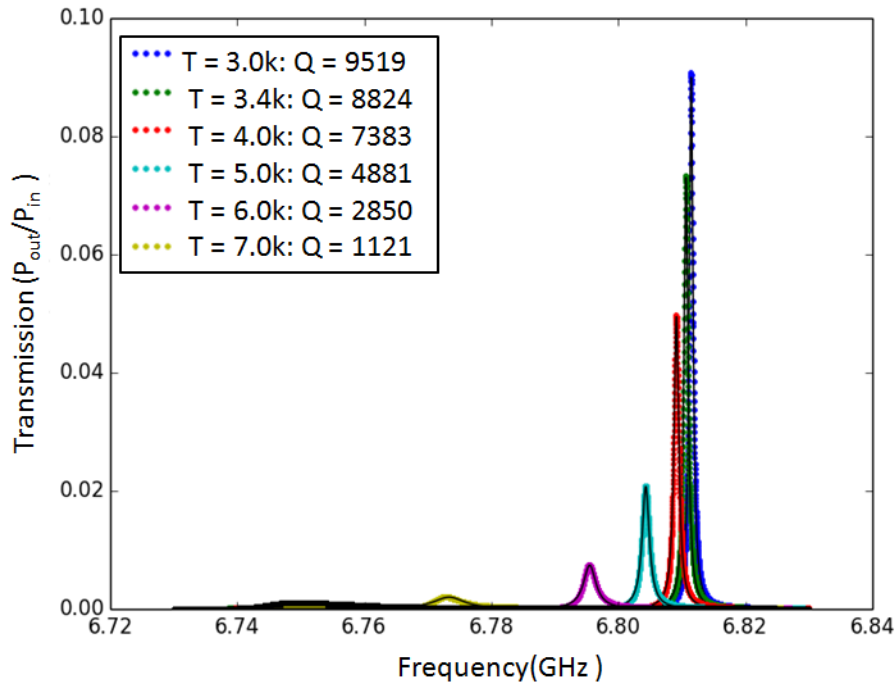
Figure 2.7: Fundamental mode of the coplanar waveguide (CPW) cavity transmission spectra with its corresponding measured temperature. The Dotted lines are the fitting using Lorentz distribution. Inlet shows the temperature color scale and Q factor of the CPW cavity.

In chapter 4, Coupling of Rydberg atoms to a CPW cavity, higher harmonic mode of our CPW cavity was utilized for Rydberg atom-cavity coupling. Here, the transmission spectra for 3rd harmonic mode was shown in figure 2.8.
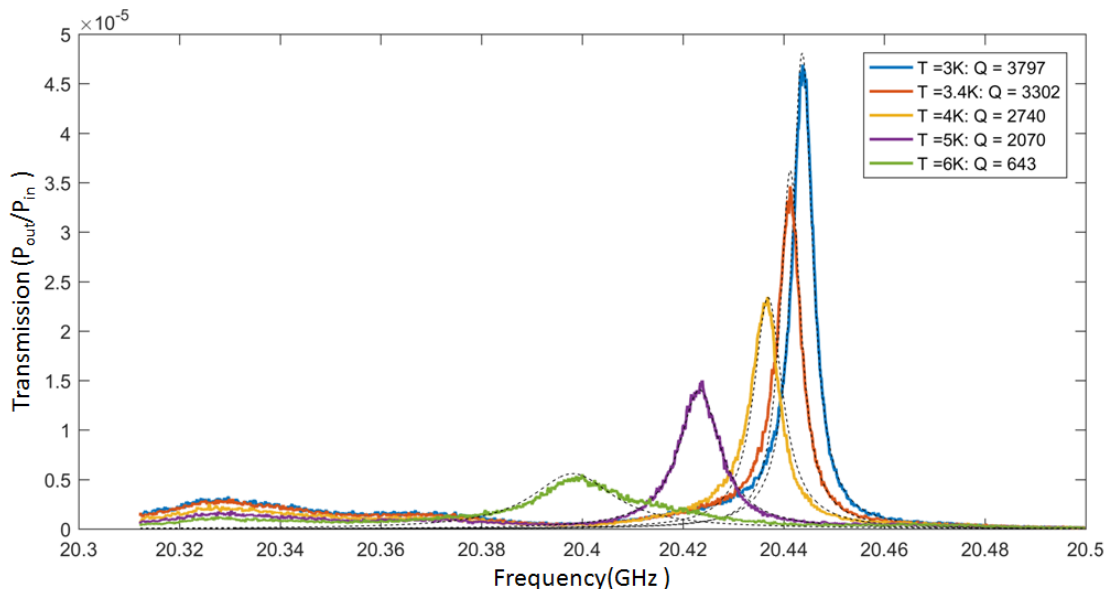
Figure 2.8: 3rd harmonic mode of coplanar waveguide(CPW) cavity transmission spectra with its corresponding measured temperature. Inlet shows the temperature color scale and Q factor of the CPW cavity.

Note that the measurements in this section were obtained before the baking of the vacuum chamber. The resonance frequency of the CPW resonator was slightly shifted after the baking. Reader should not compare the parameter obtained in this section with coming section/chapters.

It was by now obvious that transmission spectra of the CPW resonator were temperature dependence. In the following section we will discuss more in detail regarding this matter.

2.5 Cavity Temperature Dependence

Since the density of superconducting Cooper pairs and the London penetration depth $\lambda_{\rm L}$ of a type-I superconductor is temperature dependent. The cavity resonance frequency $\omega_{\rm Res}$ and linewidth κ are expected to be temperature dependence. The relation for temperature T of a superconducting CPW cavity and its resonant frequency $\omega_{\rm Res}$ is as follows:

$$\omega_{\rm Res}(T) = \frac{\omega_{\rm Res0}}{\sqrt{1 + \frac{L_k(T)}{L_0}}}, \tag{2.2}$$

where L_0 is the inductance of the cavity without the kinetic contribution and $\omega_{\rm Res0}$ is the resonance frequency for $L_k = 0$. L_k the kinetic inductance is:

$$L_k(T) = \chi_g \mu_0 \lambda_{\rm L}(T), \tag{2.3}$$

where χ_g is a geometrical factor, taking into account the spatial distribution of the superconducting current density. In the samples, $h_{\rm Nb} = 500\,{\rm nm}$ and typically London penetration depth $\lambda_{\rm L}(T = 0) \sim 100\,{\rm nm}$. The temperature dependence of $\lambda_{\rm L}$ is given by:

$$\lambda_{\rm L}(T) = \frac{\lambda_{\rm L}(T = 0)}{\sqrt{1 - \left(\frac{T_s}{T_c}\right)^4}} \tag{2.4}$$

with the sample temperature T_s and the superconducting transition temperature T_c. In addition, the relation of temperature of a superconducting CPW cavity and its resonant linewidth is as follows:

$$\kappa(T) = \kappa_0 + \kappa_1 \left(\frac{T_s}{T_c}\right)^4 \cdot \left[1 - \left(\frac{T_s}{T_c}\right)^4\right]^{-\frac{3}{2}} \tag{2.5}$$

with a temperature independent contribution κ_0 and the scaling factor κ_1. Here, $\kappa_0 = 2\pi \cdot 850\,{\rm kHz}$ and $\kappa_1 = 2\pi \cdot 3.25\,{\rm MHz}$ were used.

Figure 2.9 shows the transmission spectra, resonant frequency $\omega_{\rm Res(T)}$ and linewidth $\kappa(T)$ of the CPW cavity with different temperature value.

In order for the measurements to fit better in figure 2.9 with the analytical curve, the chip temperature $T_{\rm chip}$ from the measured temperature $T_{\rm m}$ was offset by $\sim$1.05K. This makes sense because the cryostat sensor thermometer is located $\sim$10cm away from the chip itself. Temperature gradient over such a distance was expected.

In a nutshell, the lower the temperature of a CPW cavity, the lower the kinetic inductance. With lower kinetic inductance, a higher resonant frequency can be achieved. Likewise, the lower the temperature of a CPW cavity, the lower the quasiparticle induced losses. With lower quasiparticle induced losses, a narrower resonant linewidth can be achieved[1]. Visa versa.

---

[1]Similar with an optical cavity, where kinetic inductance is the equivalent of the refraction index in the dispersion medium and losses in the cavity resulting in a broader linewidth.
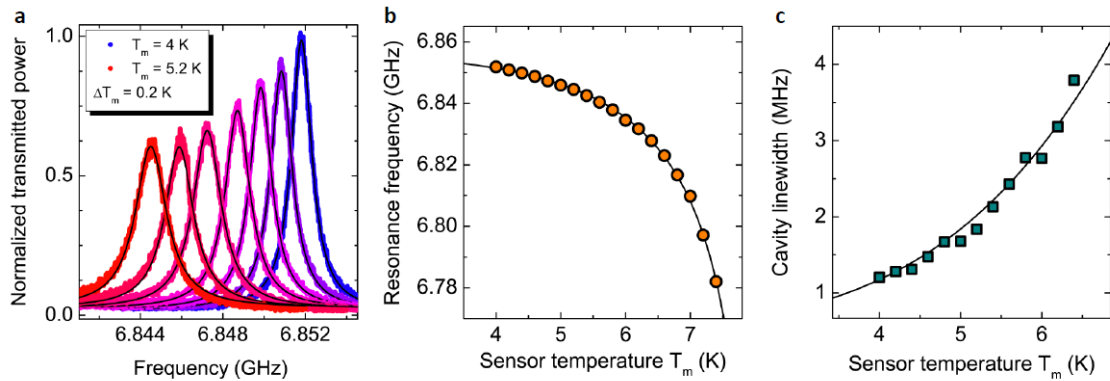
Figure 2.9: Temperature dependence of the cavity parameters. **a.** Cavity transmission spectra measured with a network analyzer. Resonance frequency shifts toward to lower and linewidth to larger values. **b.** Cavity resonance frequency vs sensor temperature, fitted with equation 2.2. **c.** Cavity linewidth vs sensor temperature, fitted with equation 2.5.

2.6   Coupling Strength of single atom to single cavity MW photon

Considering the ultimate goal of coupling a single atom with a single MW cavity photon. Here, the magnetic field and coupling rate distribution between a single photon and single atom in our CPW cavity were simulated.

The root mean square of the zero point fluctuation amplitude current I_{zpf} from a MW photon at the current antinode is given by the relation:

$$\frac{1}{2}\hbar\omega_{Res} = \frac{\lambda_0}{4}L'I_{zpf}^2 \tag{2.6}$$

For the CPW resonator, inductance per unit length is $L' = 409\,\text{nH/m}$ (kinetic inductance L_k is negligible), $\omega_{Res} = 2\pi \cdot 6.84\,\text{GHz}$ and resonance wavelength $\lambda_0 \approx 18.7\text{mm}$, resulting in I_{zpf}=33.5nA. With the current I_{zpf} known, the magnetic microwave field zero point fluctuation amplitude distribution $|B| = |B_{zpf}|$ can be simulated using software 3D-MLSI [134]. Likewise, the spatial distribution of the coupling strength between a single ground state atom and a single photon in the CPW resonator can be simulated, with the equation:

$$g_0 = \frac{|B_{zpf}(x,y)| \cdot |\mu|}{\hbar} \tag{2.7}$$

with the magnitude of the dipole transition matrix element $|\mu| = 0.25\mu_b$. Figure 2.10 shows the simulated result.

Rydberg atoms interact with MW photons via a much stronger electric dipole transition with electric coupling strength $g_E = n^2 a_o e \cdot E$. Comparing it with the magnetic dipole transition with magnetic coupling strength $g_B = \mu_b \cdot B = \mu_b \cdot \frac{E}{c}$, a
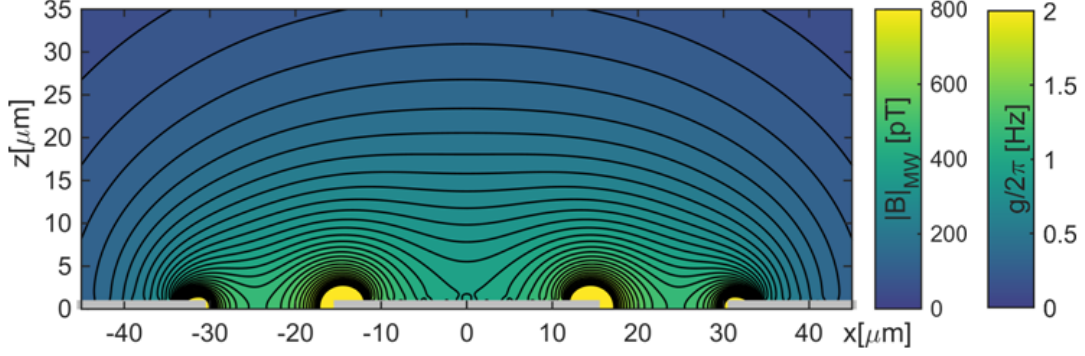
Figure 2.10: Magnetic microwave field zero point fluctuation amplitude $|B| = |B_{\mathrm{zpf}}|$ and its corresponding single-photon single-ground state atom coupling rate obtained from $|B|$. With a typical atom trapped distance of 20μm, we will achieve a ground state atom coupling rate of $g_0/2\pi \sim 0.5$Hz.

factor of $\frac{g_{\mathrm{E}}}{g_{\mathrm{B}}} \sim \frac{n^2}{\alpha}$ improvement in the single atom coupling rate can be achieved[2]. By switching a ground state atom into a Rydberg state with $n > 50$, coupling strength in the $\sim$MHz range in the vicinity of CPW resonator can be achieved and the strong coupling regime will be reached[3].

2.7 Chapter Closing

In this chapter, one of the key components of the experiment - the CPW resonator was presented. All measurements that will be mentioned in the thesis took place in this CPW resonator. The dimension of the CPW resonator is designed in a way that its resonance frequency ω_{Res} is close to the resonance frequency of another key component - the atom ω_{atom}. Further fine tuning of the resonance frequency ω_{Res} can be achieved via temperature adjustment. Last but not least, the weak coupling strength between a single ground state atom and a single cavity photon was simulated. In the next chapter, the author will show the experimental realization of the coupling between ground state atoms and CPW resonator.

---

[2]Refer to Chapter 1 for notation. Here, $a_o = \frac{\hbar}{m_e c \alpha}$ where m_e is the electron rest mass, c is the speed of light and α is the fine structure constant. Also, $\mu_b = \frac{e\hbar}{2m_e}$, this gives $\frac{g_{\mathrm{E}}}{g_{\mathrm{B}}} \sim \frac{n^2}{\alpha}$ as shown in the text.

[3]Strong coupling condition, cavity coupling rate > cavity decay rate ($g > \kappa$), where the Rydberg atoms decay rate is negligible compare to cavity photon decay rate.

Chapter 3

Coupling of Ground-state Atoms to a Superconducting Coplanar Waveguide(CPW) Resonator

In the first half of this chapter, the preparation of the atomic ensemble for atom-cavity coupling was described. The system had been set up for years. The author was therefore taken no part in designing and setting up of the optical system, vacuum chamber and the experimental control. More information regarding the system can be obtained from the predecessor of this research group [106, 133, 135, 136].

The second half of this chapter contained the description for two main experiments. First, the measurement of Rabi oscillations between two of the ^{87}Rb hyperfine ground states is presented by coherently driving the microwave(MW) cavity. Secondly, the MW field in the cavity is measured using the AC stark shift of the ^{87}Rb hyperfine ground states. In these two experiments, the author demonstrated that ^{87}Rb atoms only interact with the MW fields within the cavity, giving proof of the atom-cavity coupling.

Readers are recommend to have basic knowledge on the topics of light-atom interaction, laser cooling and atomic physics to better understand this chapter [137].

3.1 Atomic Ensemble Preparation

3.1.1 Experimental System

Vacuum system

The vacuum system was consisted with a 2D-MOT chamber and an experimental main chamber. The 2D-MOT chamber had a background pressure of $\sim 10^{-8}$mbar, this pressure was mainly the contribution of continuous loading of the Rb gas with two dispensers connected in series, excess Rb and background gases were pumped away using an ion pump(20L/s). The main chamber was separated with the 2D-MOT chamber by a differential tube of $\sim$1mm in the inner minimum diameter. The main chamber had a vacuum pressure of $\sim 10^{-11}$mbar, the pressure was maintained by ion pump(60L/s) with additionally a Titanium-sublimation pump that

were turned on once a couple of years. Most of the magnetic coils located inside the main chamber, for that, current were sent into the coils via electrical feed-through. MW feed-through for CPW resonator and high voltage (HV) feed-through for Rydberg atom ionization located on the top of the vacuum chamber, closed to the liquid helium feed line for cryostat. Figure 3.1 shown bellow were the parts of the vacuum chamber.
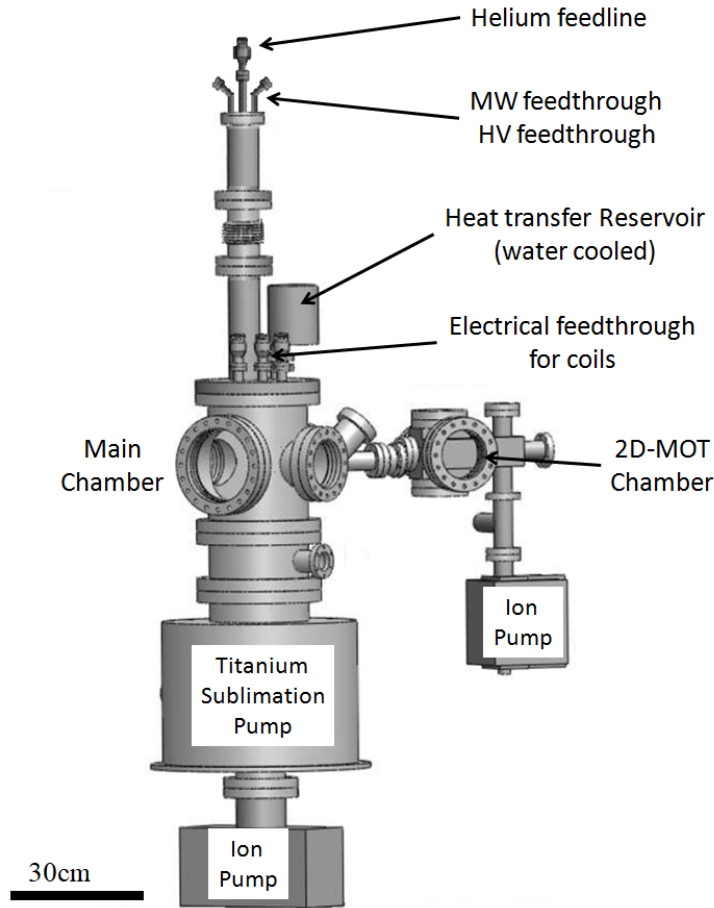
Figure 3.1: External view of the vacuum chamber, consisted of a main chamber and a 2D-MOT chamber. Vacuum in both chamber were maintain by ion pump, with an additional Titanium sublimation pump for the main chamber. Pressure for 2D-MOT chamber was $\sim 10^{-8}$mbar and 3D-MOT chamber was $\sim 10^{-11}$mbar. Currents for magnetic trapping were sent into the vacuum chamber using electrical feedthrough. Coils were thermally attached to outside of the chamber via copper pipes and were water cooled in the heat transfer reservoir. MW required for driving CPW resonator were sent in via MW feedthrough. HV for Rydberg atom ionization were sent into the chamber cia HV feedthrough. Both (MW and HV feedthrough) located on the top of the vacuum chamber, close by to the liquid helium feed line for cooling of the atom chip to cryogenic temperature. Figure was modified from Danial Cano PHD thesis [133].

Magnetic Traps in Main Chamber

Here, we take a closer look of the design inside the chamber. Slow atoms from 2D-MOT were loaded into the 3D-MOT. Then, Sisyphus cooling take place, followed by optical pumping to a magnetically trappable state. Atoms were then trapped in the B-field minimum created from the MOT coil. This minimum B-field was then shifted towards to the Ioffe coils via ramp down the MOT coils current and ramp up the transfer coil current in an adiabatic manner. To create a conservative magnetic trap for RF cooling, Ioffe wire and Ioffe coils were turned on. Atoms were RF cooled to ∼1uk before loading into the dipole trap. Shown in figure 3.2 is the interior of the main vacuum chamber.
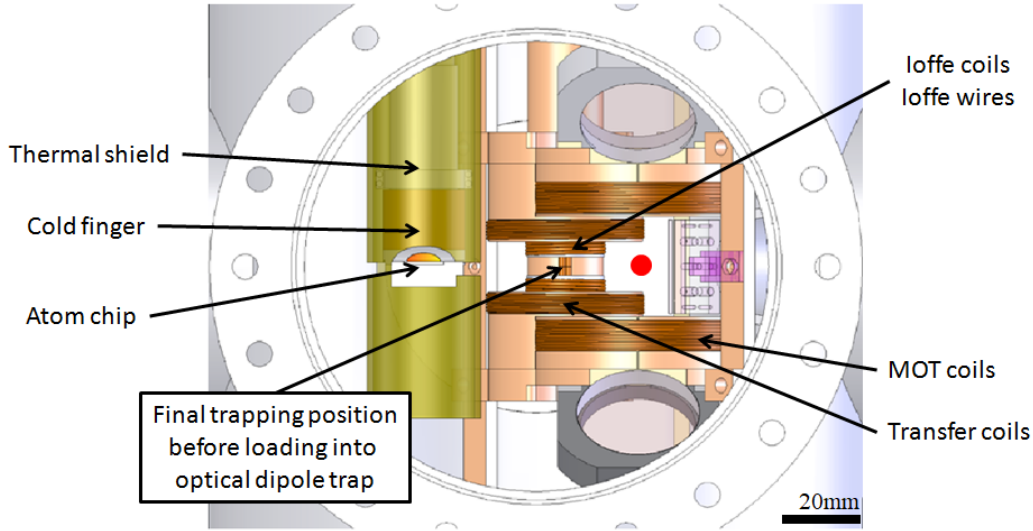
Figure 3.2: Interior view of the vacuum chamber. Atoms were loaded from the 2D-MOT into the 3D-MOT (MOT position shown in red). This was followed by sub-Doppler cooling and then optical pumping. Atoms, then trapped in the minimum quadrupole B-field created by the MOT coils. Atoms were then further magnetically transferred into Ioffe trap for RF cooling before loaded into an optical dipole trap.

Transferring into Atom Chip

Atoms were transferred from Ioffe trap to atom chip Z-trap via optical dipole trap. Here, single Gaussian focus beam was used. The focusing lens for the optical dipole trap were located on top of a mechanical translation stage, where the focus point of the beam (ODT) was free to move from the Ioffe trap to above the chip. After the dipole trap moved to above the chip, the Z-trap current was slowly ramp up together with the bias B-field in y-direction. This created a B-field minimum for atoms trapping on the atom chip. Lastly, intensity of the ODT was then ramp down, atom transfer from Ioffe trap to atom chip trap was complete. Figure 3.3 illustrates this process.
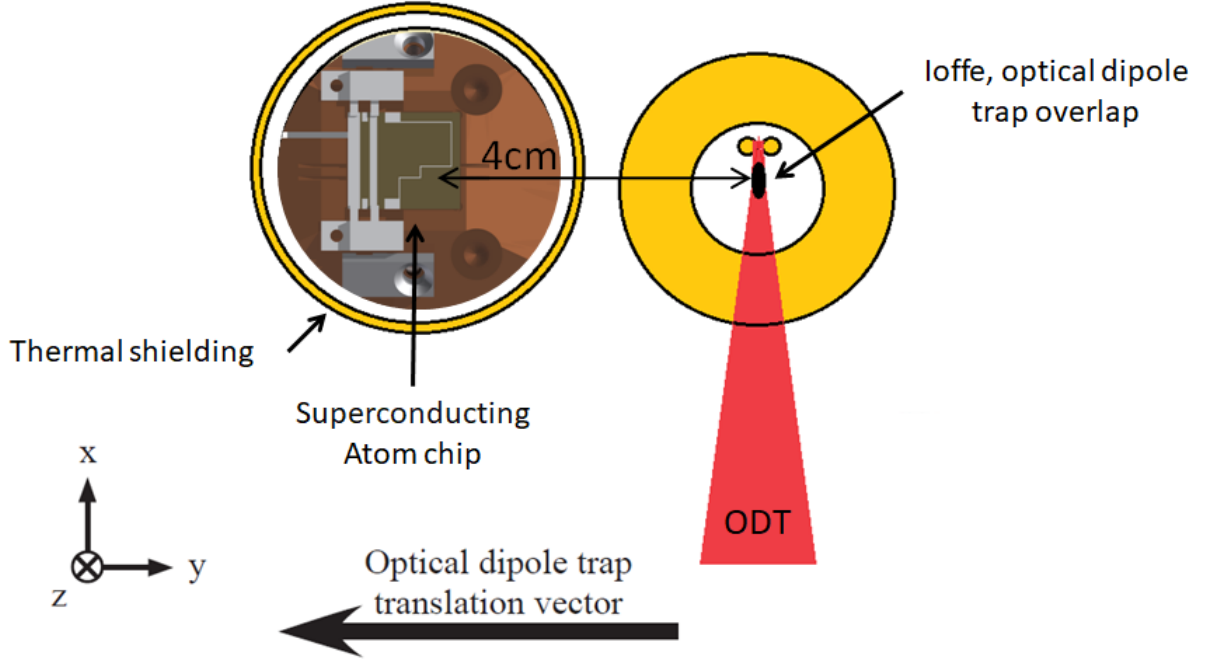
Figure 3.3: The atom chip and Ioffe trap were located on the same horizontal level (x-y plane) with separation of ~4cm. A fiber laser with wavelength of 1064nm was focused into a minimum beam width of ~20μm, creating an optical dipole trap (ODT). Atoms were pre-cooled using RF evaporation method to ~1μk range, hence, only 150mW was required for the ODT (transfer efficiency 80%). Focusing lens of the ODT was located on a mechanical translation stage, where focus point of the ODT was free to move between the Ioffe trap and atom chip Z-trap. Loading from Ioffe trap into atom chip Z-trap was done simply by shifting the ODT to above the atom chip, then turning on Z-trap current and bias B-field to create a Z-trap for loading into atom chip.

Atom Chip Z-trap Manipulation

The Z-wire on the atom chip was located away from the CPW resonator by ~200μm. To transport atoms form the Z-trap into the CPW resonator, we utilized the Z-trap rotation via changing the vector of the bias B-field.

The magnetic field produced by a Z-wire can be approximated as a magnetic field produced by running current to an infinitely long wire, $B(z, y) = \frac{\mu_0 I}{2\pi\sqrt{z^2+y^2}}$, where μ_0 is the permeability of free space, I is the current running along the wire, and $\sqrt{z^2 + y^2}$ is the distance radially away from the wire. With an external bias field applied to the Z-trap, a B-field minimum will occur due to magnetic field cancellation at the point(z,y). By slowly varying the vector of the bias B-field, B-field cancellation point(z,y) can be manipulated. Figure 3.4 illustrates the idea behind the Z-trap rotation.
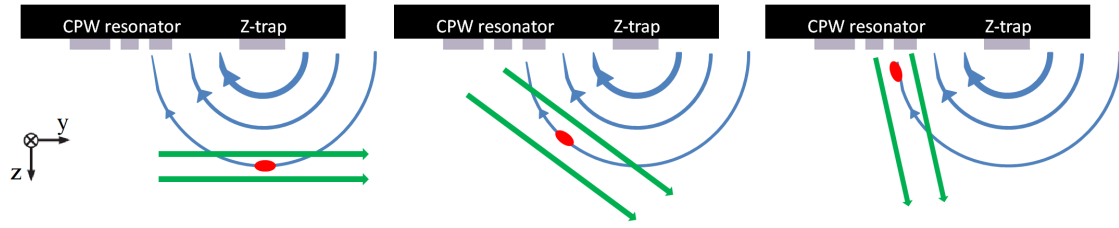
Figure 3.4: Z-trap rotation process from left to right. Figure above shows the side view of the atom chip structures. Magnetic field produce by the Z-trap(blue) and a bias B-field(green) propagating on the y-direction produced a field minimum(red) above the Z-wire for atoms trapping . By slowly introducing a bias B-field component in the z-direction, field minimum can be shifted towards to the CPW resonator.

Trapping of Atomic Ensembles in a CPW Resonator

It had been shown in chapter 2, that MW field strength decay rapidly away from the CPW resonator. In favor of a decent atom-cavity coupling rate, it is therefore necessary to trap atoms in the proximity of these fields. This can be accomplished by taking advantage of persistent currents in a superconducting loop. Persistent currents can be generated by magnetic flux freezing during the normal conducting-superconducting crossing [138, 139].

A closed superconducting loop around the CPW resonator gap is formed using one side each of the CPW resonator input/output coupling inductors(Figure 2.3), the ground plane and the center conductor. For this reason one side of the super-conducting ground plane is strategically cut through using a slit of gold such that only one superconducting closed loop can exist(Can be seen in figure 2.1).

The magnetic field induced from the persistent currents in this loop, together with a homogeneous bias magnetic field produces a B-field minimum within the CPW resonator gap for the ease of magnetic trapping of neutral atoms [140] as presented in the figure 3.5. The trapping distance from the chip can be finely tuned by the amount of flux trapped in the loop and by adjusting the magnitude of the homogeneous bias field.
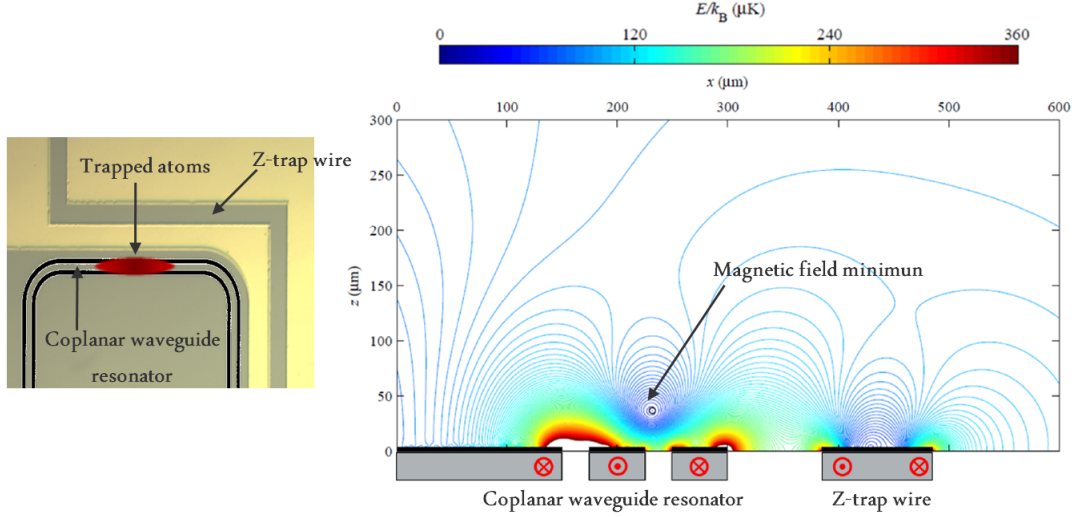
Figure 3.5: **On the left:** Top view of trapping region, atoms are trapped using persistent supercurrents around the cavity gap and an external bias b-field. Together with two parallel confinement wires under the chip, the atomic ensemble can be trapped close to the position of the antinode in the resonator. **On the right:** Simulation of the magnetic field distribution with a bias field perpendicular to the chip. Here, a cut trough of the chip is shown instead, with a magnetic field minimum shown within the gap of CPW resonator. This simulation was taken from Dominik Wiedmaier's Master-Thesis.

State Selective Adsorption Imaging

At the end of the ground-state atom-cavity interactions, it was required to probe the ^{87}Rb ground-state atom number for both $5^2S_{1/2}\ |F=1\rangle$ and $5^2S_{1/2}\ |F=2\rangle$ state denoted by $|F=1\rangle$, $|F=2\rangle$. Here, we used the absorption imaging method [141]: The number of atoms in $|F=2\rangle$ were measured by shining resonant imaging light to the $5^2S_{1/2}\ |F=2\rangle\ \rightarrow\ 5^2P_{3/2}\ |F=3\rangle$ transition. The shadow, then cast on a CCD camera and optical depth detected was used to determine the atomic number. For detection of atomic number in $|F=1\rangle$, atoms were then pumped from $|F=1\rangle\ \rightarrow\ |F=2\rangle$ using re-pumping light to the $5^2S_{1/2}\ |F=1\rangle\ \rightarrow\ 5^2P_{3/2}\ |F=2\rangle$ transition, before detected by imaging light. Figure 3.6 shown the imaging light axis for the state selective detection.
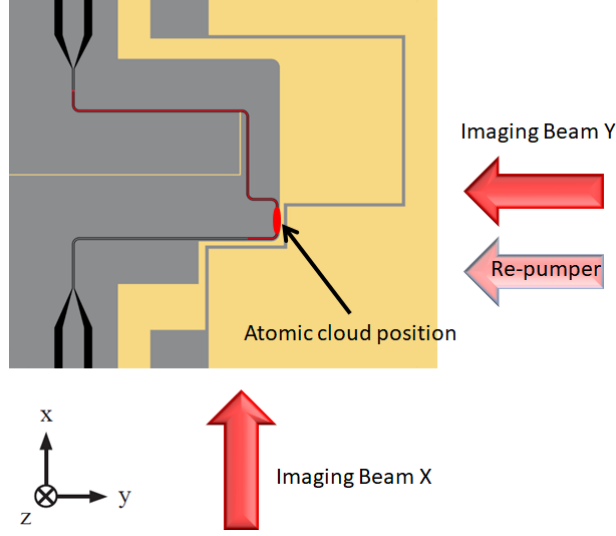
Figure 3.6: Imaging light axis used for the state selective detection for ^{87}Rb ground-state atom of $5^2S_{1/2}$ $|F = 1\rangle$ and $5^2S_{1/2}$ $|F = 2\rangle$. The atom number in $|F = 2\rangle$ were measured by shining resonant imaging beam Y to the $5^2S_{1/2}|F = 2\rangle \rightarrow 5^2P_{3/2}|F = 3\rangle$ transition. Then, the re-pumper light that was resonance with the $5^2S_{1/2}|F = 1\rangle \rightarrow 5^2P_{3/2}|F = 2\rangle$ transition pumped the atoms from $|F = 1\rangle \rightarrow |F = 2\rangle$. Finally, imaging beam X was used for probing the remaining atoms. Atom number can be determined by measuring the optical depth casted on a CCD camera. With this scheme, atom number in both $|F = 2\rangle, |F = 1\rangle$ states can be measured in a single experiment cycle.

Figure 3.7 shows the absorption imaging of a typical atomic ensemble prepared above the CPW resonator using imaging beam Y.
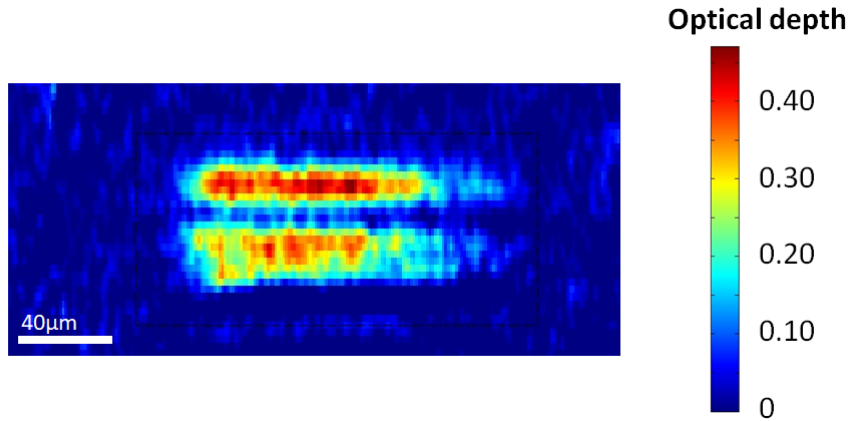
Figure 3.7: Absorption imaging of the atomic cloud. Imaging light is reflected on the atom chip, hence two atom clouds are seen as the result of mirror image. Shown here are $5\cdot10^4$ atoms in state $|F = 2\rangle$ magnetically trapped $\sim20\mu$m above the CPW resonator.

3.1.2 Atomic Ensemble Preparation Procedure

2D & 3D Magneto-optical trap (Duration: 4 s)

    2D-MOT: Cooling power: 45 mW   Re-pumper power: ~1.5 mW
    3D-MOT: Cooling power:200 mW   Re-pumper power: ~1.5 mW
    Cooling laser detuning Δ = -15 MHz away from $5P_{3/2}$ (F = 3)

Sub-Doppler cooling (Duration: 4 ms)

    Cooling laser detuning Δ = -54 MHz away from $5P_{3/2}$ (F = 3)
    Atom number: ~10^8 Temperature: ~50 μk

Optical Pumping to $5S_{1/2}$ (F = 1, mf = -1) magnetic trappable state (Duration: 100 μs)

    Optical pumping power: ~200 μW

Magnetic trapping in MOT coil and transfer to Ioffe trap (Duration: 3 s)

RF evaporative cooling in Ioffe trap (Duration: 9 s)

Loading from Ioffe trap into ODT (Duration: 200 ms)

    Atom number: ~10^6 Temperature: ~2 μk

Optical transport to the atom chip Z-trap (Duration: 700 ms)

Z-trap rotation into CPW resonator persistant super current trap

    Atom number: ~10^5 Temperature: ~2 μk

RF evaporative cooling in the CPW resonator

    Atom number: ~10^4 Temperature: ~800 nk

Atom-cavity interaction

    Rabi oscillation with cavity MW photons
    MW dressing with cavity photons

State selective Imaging for $5S_{1/2}$ (F = 1) and $5S_{1/2}$ (F = 2)

    Imaging light power: ~150 μW
    re-pumping light power: ~100 μW

Figure 3.8: The general procedure for a single experimental cycle. Duration of the phases are written in brackets. Some parameters required for scheduled optimization are listed for referencing purposes. Only the procedure for the atom chip Z-trap loading and onwards (Steps included in the dotted box) will be described here in this section.

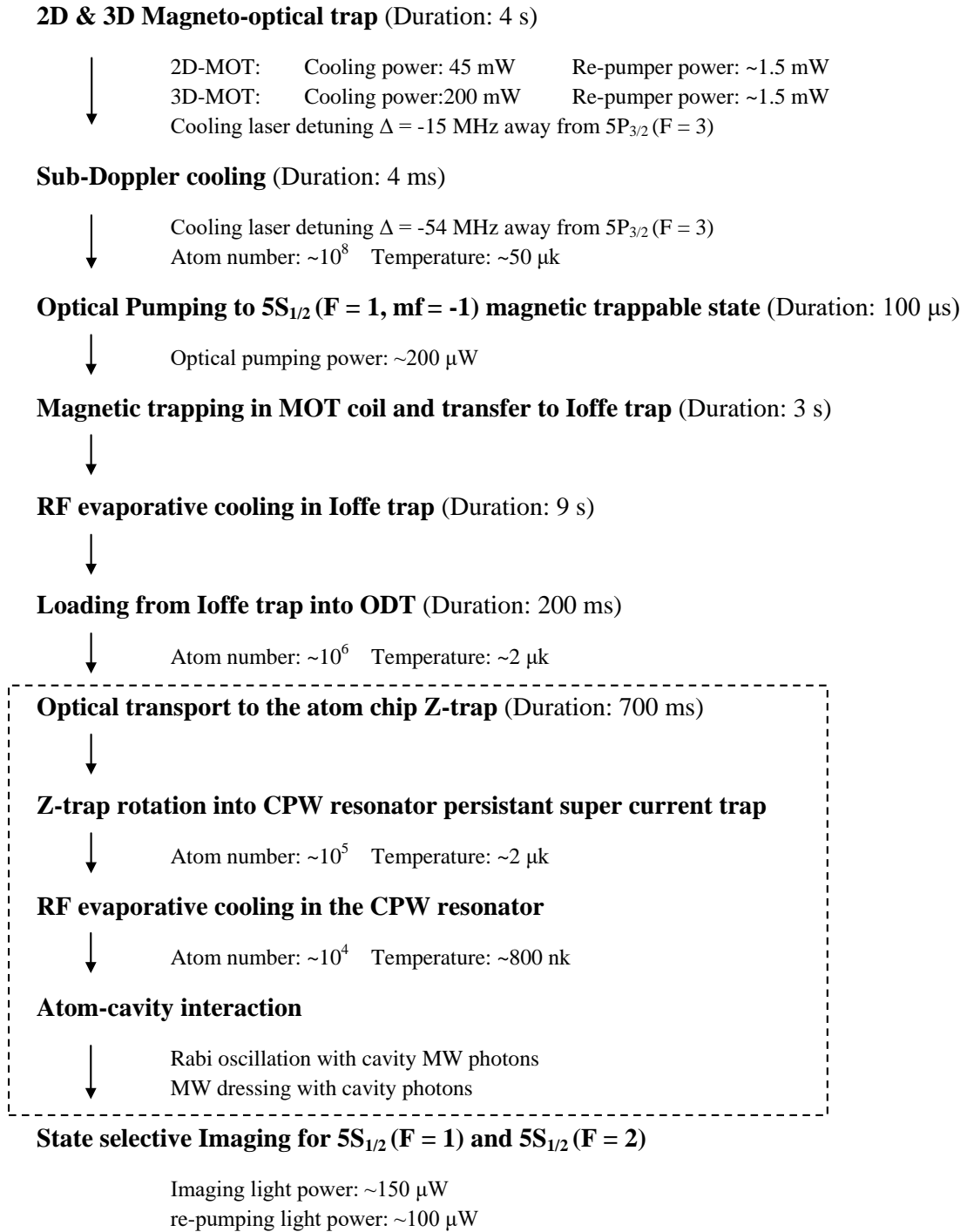The process of the atomic cloud preparation remain unchanged (MOT loading ↦ Sub-Doppler cooling ↦ optical pumping ↦ magnetic quadrupole trapping ↦ magnetic transfer ↦ Ioffe trap ↦ RF cooling ↦ Optical dipole trapping) and will not be further described in this thesis, readers are advice to refer to [133, 136] for more details. Figure 3.8 shown was the experimental procedure. Here, we continue with the discussion at the point where atoms were already trapped in the atom chip Z-trap.

Trapping Parameters in the Atom Chip

The bias B-field in the system was controlled by three pairs of coils (x, y, z axis) in Helmholtz configuration located outside the vacuum chamber. Bias coil current converted to B-field were calibrated as 3.31 G/A, 4.9 G/A and 2.35 G/A correspondingly for x-axis, y-axis and z-axis. A flux was stored in the superconducting CPW resonator loop by having the bias B-field in the z-axis set to 1.175G during the normal conducting to the superconducting transition stage. It was shown in chapter 2, that there were two wires running in parallel under the atom chip. These two wires served to provide extra confinement along the x-axis.

Atoms were loaded from the ODT to the Z-trap by overlapping the ODT with the Z-trap magnetic field minimum. The overlapped position of the ODT and Z-trap was $\sim 250\mu$m above the chip. ODT was then turned off in 200ms time for the transfer process to be complete. Since a weak x-axis bias B-field of 0.66G was turned on during the transfer process from ODT to Z-trap. The atoms still maintained a definite spin for the Z-wire magnetic trapping. At this trapping point, the Z-trap current was set to 0.4A, with the y-axis bias B-field set to 1.715G. A weak B-field in the z-axis were set to 0.33G to compensate with the earth magnetic field.

For better transfer efficiency of the Z-trap into the CPW resonator, the initial position of Z-trap rotation was crucial. Because of this, Z-trap minimum was raised close to the chip by lowering the Z-wire current to 0.35A and increasing the y-axis bias field to 0.4A. Also, confinement current was turn on to 0.8A. At this point atoms were trapped $\sim 100\mu$m above the Z-trap.

The rotation of the Z-trap started by increasing the bias B-field to 2.6G in the z-axis. Atoms were slowly shifted towards the CPW resonator. During the end of the rotation, Z-wire current was ramp down to zero. The combination of the persistent current in the CPW resonator loop, the bias B-field and the confinement wire were capable of creating a B-field minimum at a distance of $\sim 20\mu$m above the CPW resonator gap. Bias B-field in x-axis was set to 2.2G such that the trap minimum in the CPW resonator gap reached the magic magnetic trapping point of 3.2G.

Atoms trapped in the CPW resonator gap had a temperature of $\sim 2\mu$k. It was then reduced to ~ 800nk by the method of RF evaporation cooling, via driving the Z-wire with a RF ramp from 3MHz to 2.4MHz and with a constant amplitude V_{pp} of 1V.

This was the standard procedure for preparing the atomic ensembles for the atom-cavity coupling experiment. Figure 3.9 summarized the entire process in details.

Z - Trap after loaded from ODT

Z-trap current: 0.4 A
Confinement wire Current: 0 A
Bias B-field x-axis coil current: 0 A
Bias B-field y-axis coil current: 0.35 A
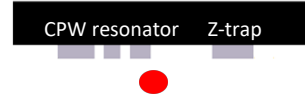Bias B-field z-axis coil current: 0.1416 A
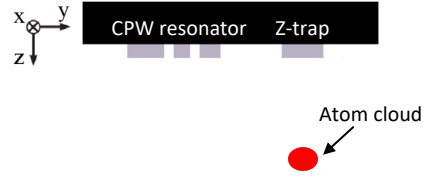
Z - Trap re-positioning (Duration: 500 ms)

Z-trap current: 0.35 A
Confinement wire Current: 0.8 A
Bias B-field x-axis coil current: -0.025 A
Bias B-field y-axis coil current: 0.4 A
Bias B-field z-axis coil current: 0.1416 A

Z - Trap rotation (Duration: 500 ms)

Z-trap current: 0.27 A
Confinement wire Current: 0.4 A
Bias B-field x-axis coil current: -0.045 A
Bias B-field y-axis coil current: 0.3 A
Bias B-field z-axis coil current: 1.1 A

Z - Trap rotation into CPW resonator gap (Duration: 500 ms)

Z-trap current: 0.0 A
Confinement wire Current: 0.8 A
Bias B-field x-axis coil current: -0.66 A
Bias B-field y-axis coil current: 0 A
Bias B-field z-axis coil current: 1.1 A
Flux trapped via bias B-field z-axis coil current: 0.5 A
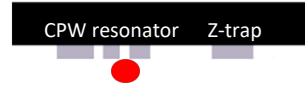
RF evaporative cooling in the CPW resonator (Duration: 2 s)

Frequency ramp: $3.0\text{MHz} \rightarrow 2.4\text{MHz}$
RF power V_{pp}: 1V
Final temperature: ~800 nk
Atom number: ~10^4
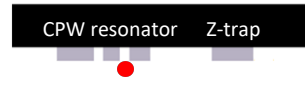
Atoms-cavity interaction experiment

Figure 3.9: Shown in figure is the procedure of atoms transfer from Z-trap to the persistent current trap in the CPW resonator gap. The Atoms were re-positioned in the Z-trap to facilitate maximum transfer efficiency into the resonator. Then, a bias B-field was slowly applied in the Z-axis to facilitate the rotation of the Z-trap. Finally, a persistent current trap was formed by using the flux trapped in the CPW resonator loop and the bias B-field. RF cooling was then applied to achieve a lower cloud temperature. Only then atoms-cavity experiments were conducted. All parameters used where listed, with the duration of the phases written inside the parentheses. Drawn on the right side, shows the side view of the atom chip. The pictures illustrated the position of the atom cloud (red) in each step (Drawn not to scale).

3.2 Coherent Control of Atomic States with Cavity Field

3.2.1 Rabi Oscillations of ^{87}Rb hyperfine ground state

Interaction of a two-level atom with radiation

When the two hyperfine state $|1\rangle$ and $|2\rangle$ with wave function shown as bellow[1]:

$$\Psi(r,t) = c_1 |1\rangle e^{-i\omega_1 t} + c_2 |2\rangle e^{-i\omega_2 t} \tag{3.1}$$

Where $\omega_{1,2}$ is the frequency corresponded energy state $E_{1,2}$ of $|1\rangle$ and $|2\rangle$, and normalization requires that the two coefficients $c_{1,2}$ satisfy:

$$|c_1|^2 + |c_2|^2 = 1 \tag{3.2}$$

Interacts with a electromagnetic radiation described with electric dipole Hamiltonian:

$$H_I(t) = er.\mathrm{E}_0 \cos(\omega t) \tag{3.3}$$

Where E_0 is the amplitude of the EM wave and $-er$ corresponds to the energy of an electric dipole in the electric field. Substituting equation 3.1 into time-dependent Schroedinger equation:

$$i\hbar \frac{\delta \Psi}{\delta t} = H\Psi \tag{3.4}$$

With total Hamiltonian $H = H_0 + H_I$ with $H_0 = E_2 - E_1$. This leads to:

$$i\dot{c_1} = \Omega \cos(\omega t) e^{-i\omega_0 t} c_2 \tag{3.5}$$

$$i\dot{c_2} = \Omega^* \cos(\omega t) e^{-i\omega_0 t} c_1 \tag{3.6}$$

Where $\omega_0 = \omega_2 - \omega_1$, and Rabi frequency Ω is defined by:

$$\Omega = \frac{\langle 1| er.E_0 |2\rangle}{\hbar} = \frac{e\mathbf{r_{1,2}}|E_0|}{\hbar} \tag{3.7}$$

where

$$\mathbf{r_{1,2}} = \langle 1| r |2\rangle \tag{3.8}$$

Rotating Wave Approximation and Rabi Flopping

To solve for the two time-dependent coefficients $c_1(t)$ and $c_2(t)$, we need to make further approximation. Equation 3.5 and 3.6 can be rewrite as:

$$i\dot{c_1} = c_2 \left\{ e^{i(\omega_0 - \omega)t} + e^{-i(\omega_0 + \omega)t} \right\} \frac{\Omega}{2} \tag{3.9}$$

$$i\dot{c_2} = c_1 \left\{ e^{-i(\omega_0 - \omega)t} + e^{i(\omega_0 + \omega)t} \right\} \frac{\Omega^*}{2} \tag{3.10}$$

---

[1]We follow the derivation shown in Atomic physics text book from Christopher J.Foot [142]

Here, we assume the rotating-wave approximation where the term with $(\omega_0 + \omega)t$ oscillates very fast and therefore averages to zero over the interaction time. This lead to:

$$i\dot{c}_1 = c_2 \left\{ e^{i(\omega_0 - \omega)t} \right\} \frac{\Omega}{2} \tag{3.11}$$

$$i\dot{c}_2 = c_1 \left\{ e^{-i(\omega_0 - \omega)t} \right\} \frac{\Omega^*}{2} \tag{3.12}$$

The solution of this differential equation with initial condition $c_1(0) = 1$ and $c_2(0) = 0$ gives the probability of being in the upper state as:

$$|c_2(t)|^2 = \frac{\Omega^2}{\Omega^2 + (\omega - \omega_0)^2} \sin^2\left(\frac{\sqrt{\Omega^2 + (\omega - \omega_0)^2}}{2} t \right) \tag{3.13}$$

For the resonance cast with $\omega = \omega_0$, we got:

$$|c_2(t)|^2 = \sin^2\left(\frac{\Omega t}{2} \right) \tag{3.14}$$

Similarly the probability of being in the lower state is:

$$|c_1(t)|^2 = \cos^2\left(\frac{\Omega t}{2} \right) \tag{3.15}$$

Hence, when a two-level system interacts with a continues EM waves. The population oscillates between this two level. This known as Rabi flopping.

Rabi Oscillations of the ^{87}Rb hyperfine ground state

The derivation shown above assume that the two-level system interacts with the EM wave via electric-dipole interaction. For the case of the ^{87}Rb hyperfine ground state, they interact via magnetic dipole interaction $H_I = \vec{\mu} \cdot \vec{B}_{\mathrm{MW}}$. Fortunately the physics is still the same, when the hyperfine splitting of $|1, -1\rangle$ and $|2, 0\rangle$ interact with a continuous resonant MW, the population of these two states will undergo Rabi flopping with relation shown in equation 3.14 and 3.15. The frequency of this oscillation is similar as equation 3.7 and it is given by:

$$\Omega_0 = \frac{\vec{\mu} \cdot \vec{B}_{\mathrm{MW}}}{\hbar} \tag{3.16}$$

where Ω_0 is called Rabi frequency. $\vec{\mu}$ is the atomic magnetic moment and $\vec{B}_{\mathrm{MW}}$ is the amplitude of B-field MW component. Thus, a higher Rabi frequency measured indicates a stronger component in field amplitude and vice versa.

Rabi Oscillations De-phasing

Rabi oscillations however, will not go on indefinitely in real world scenarios. The hyperfine levels of ^{87}Rb are subjected to fluctuation, de-phasing occur between these energy levels and the EM field. The inhomogeneity in EM field strength will also lead to de-phasing. Hence, the resulting Rabi oscillation is a damped oscillation. A longer coherence time indicated a better isolated atomic ensembles.

3.2.2 Cavity Driven Single-photon Rabi Oscillation

Experimental Procedure

Here, we continue from the part where the atoms were prepared in the CPW resonator. Before the atom-cavity experiment were conducted, about 10^4 atoms in state $|1, -1\rangle$ were magnetically trapped at distance $\sim 20\mu$m above the resonator gap via persistent current and bias field. Further confinement in the x-axis was achieved via driving current into the confinement wires, mentioned in the end of section 3.1.2.

Bias magnetic field calibration: [87]Rb ground states had a first order Zeeman splitting of 0.7MHz/G for $|1, -1\rangle$ state. The $|2, 0\rangle$ state is independent of the first order linear Zeeman shift and splitting between the state $|1, 0\rangle$ and $|2, 0\rangle$ had been accurately known as 6.834682GHz [110]. It was required for the offset of the magnetic trap minimum to be prepared at 3.2G^2. In the experiment, the B-field was offset to $\sim$3.2G via changing the bias field in x-axis.

Bias magnetic field was calibrated to 3.2 G as follow: A short MW pulse of 20μs was driven into the cavity with the MW power of 10dBm. The MW frequency was set on resonance with respect to state $|1, -1\rangle \leftrightarrow |2, 0\rangle$ at 3.2G. The energy splitting between the state was calculated to be 6.83242GHz. Then, the magnetic field were set to be the scanning variable. When B-field was scanned to 3.2G, resonant condition was achieved and maximum atoms number at $|F = 2\rangle$ will be measured using absorption imaging technique. We achieved a 3.2G offset B-field via running current of -0.66A into x-axis bias field coils.

Measurement technique for one photon Rabi oscillation For single photon Rabi oscillation measurement: Temperature of the cavity was stabilized at 6.7k. MW photons with frequency $\omega_0 = 2\pi \cdot$ 6.83242GHz (Resonance with $|1, -1\rangle \leftrightarrow |2, 0\rangle$ at 3.2G) were fed directly into cavity via the microwave SMA connection feedthrough. We used a constant input power of 10dBm and switching of Rabi oscillations time was done using MW switch (Model: Mini-Circuits ZASWA-2-50DR). Rabi oscillation time t_{rabi} was set to increase with increment of 5μs for each experiment cycle. Maximum t_{rabi} time was set such that at least a full Rabi flopping was observed. The frequency of the Rabi flopping was then measured. Shown in figure 3.10 is the level scheme used for the cavity driven Rabi oscillation.

---

[2]Reason for a magic offset field at $\sim$3.2 Gauss will be explained in the case of two-photon Rabi oscillation
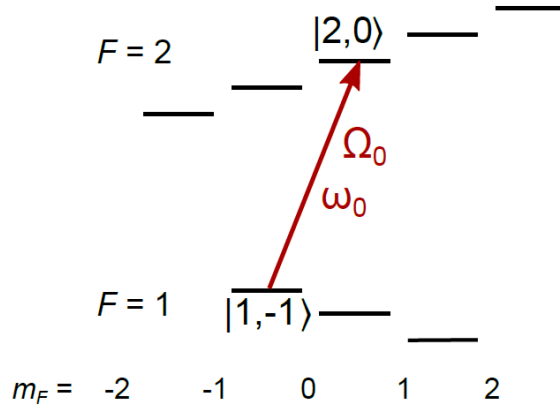
Figure 3.10: The level scheme for the cavity driven one-photon Rabi oscillation with ^{87}Rb hyperfine ground-state. Magnetic field offset is set to 3.2G. With the first order Zeeman shift of 700kHz/G, we calculated the resonance frequency to be $\omega_0/2\pi$=6.83242GHz for $|1,-1\rangle \to |2,0\rangle$ transition. The MW photons were fed directly into the CPW resonator, and the relation between Rabi oscillation frequency and cavity temperature was investigated.

Observation and Discussion

Rabi oscillations between the two hyperfine ground states were measured by absorption imaging method. A set of Rabi oscillations was measured with the cavity temperature set from 6.7K to 7.0K. For each temperature, Rabi oscillation recorded was temperature dependent and had a frequency ranging from 10kHz to 40kHz as shown in figure 3.11

This is the first evidence that atoms were coupled with MW cavity photons and can be understood as follow. Figure 3.11 shows the temperature dependence of cavity resonance frequency ω_{cav} and its corresponding width $\pm\kappa$ obtained from transmission data. The closer the cavity resonance frequency ω_{cav} to the driving frequency ω_0, the more MW photons can transmit into the cavity. Moreover, the more MW field in the cavity, the higher the Rabi frequency Ω_0.

Ideally, the maximum Rabi frequency was expected to take place when $\omega_{\mathrm{cav}} = \omega_0$. This could not be realized in the setup, because for $\omega_{\mathrm{cav}} = \omega_0 = 2\pi \cdot 6.83242$GHz, the cavity temperature should be set at 7.2K. At this temperature the SC persistent current is too weak to support a stable magnetic trap for atoms.
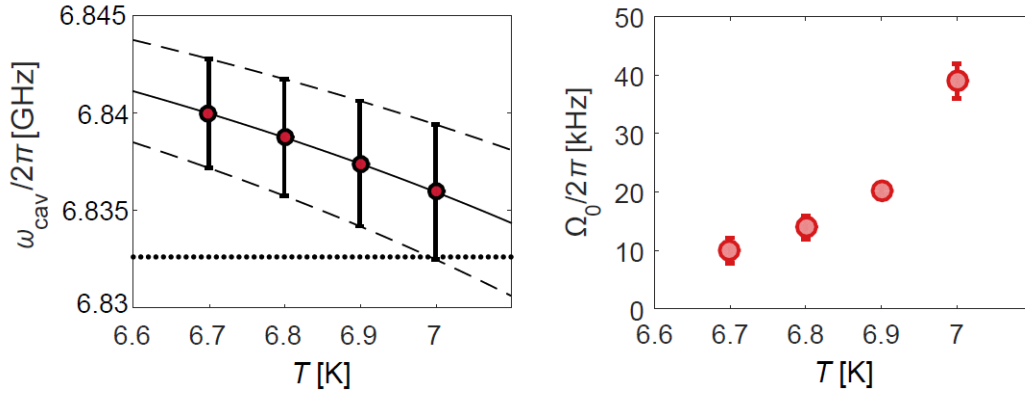
Figure 3.11: **Left :** Temperature dependence of the cavity resonance frequency ω_{cav}. The circles and error bars indicate the peak and the width ($\pm\kappa$) of the cavity line obtained from the resonator transmission data. The solid and dashed lines indicate the temperature dependence of the cavity frequency and linewidth.(Refer to Chapter 2 for details).The horizontal dotted line indicates the driving frequency ($\omega_0/2\pi$=6.83242GHz), corresponding to the atomic resonance $|1,-1\rangle \rightarrow |2,0\rangle$. **Right :** Temperature dependence of the Rabi frequency Ω_0. While the cavity is driven at the same frequency ω_0 for all measurements, microwave intensity inside the cavity changes with temperature, leading to changes in the Rabi frequency Ω_0.
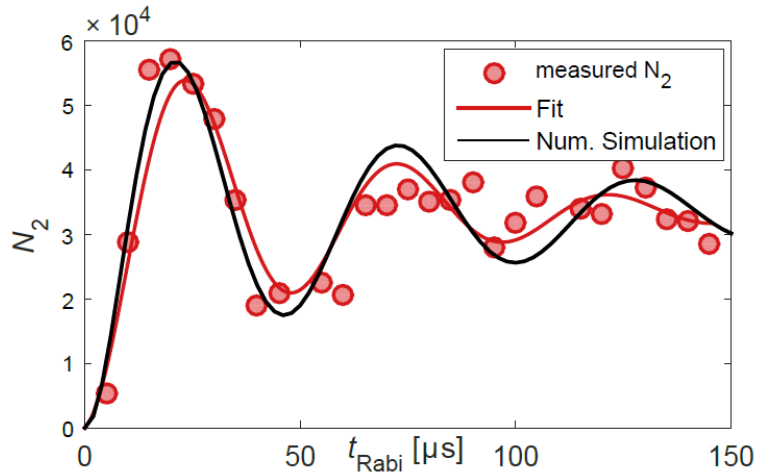
Figure 3.12: The figure shows single-photon Rabi oscillation measurement for temperature T=6.9K. Red circles are the measurement data points. The red line is the fitting using a damped sinusoidal function. The black line is the numerical simulation by assuming de-coherence is primarily contributed by the inhomogeneity of a MW cavity field seen by the stationary atomic ensemble. We observe a damping in the single-photon Rabi oscillations with a time constant of $\tau \approx 50$ μs.

Figure 3.12 shows one of the Rabi oscillation obtained with a cavity temperature of 6.9K. A short coherence time of only $50\mu s$ was measured. This was caused by the

inhomogeneity of MW cavity field[3] seen by the atoms and first order Zeeman shift that only subjected to state $|1,-1\rangle$ (not to state $|2,0\rangle$). In the next section, this problem would be tackled and a Rabi oscillation scheme with a longer coherence time will be provided.

3.2.3 Cavity Driven Two-photon Rabi Oscillation

Advantages of two-photon Rabi Oscillation for ground-state ^{87}Rb

For a good qubit memory devices, beside the basic requirement of having a long coherence time, it was also required to have a decent trapping lifetime. This was not possible with the single photon Rabi oscillation scheme, due to the magnetic untrappable upper state $|2,0\rangle$. Here, we considered the case where both states are a magnetic trappable state $|1,-1\rangle$ and $|2,1\rangle$. Both of the states had the same first order linear Zeeman shift of 0.7MHz/G, hence their relative shift is only given by quadratic Zeeman shift. It was essential for atoms to be prepared in a magnetic field with a trap minimum at the offset magic B-field point of B_m=3.23G. At this magic point, the differential offset point between that $|1,-1\rangle$ and $|2,1\rangle$ was minimized and the magnetic shift can be calculated using Breit-Rabi formula [110]:

$$\Delta E_{\text{shift}} = 431(\text{B} - \text{B}_m)^2 \tag{3.17}$$

As we can easily compare: In the case of using $|1,-1\rangle \leftrightarrow |2,0\rangle$ single photon interaction, 100mG in B-field fluctuation will lead to a 70kHz fluctuation in phase. Where for the case of $|1,-1\rangle \leftrightarrow |2,1\rangle$ two photon interaction, the same 100mG in B-field fluctuation will only lead to $\sim$4Hz of phase fluctuation. Because of this, two photon interaction with $|1,-1\rangle$ and $|2,1\rangle$ states were much more reluctant to magnetic field fluctuation caused de-coherence, making it suitable for a qubit memory device.

Experimental Procedure

In order to have magnetic dipole transition between state $|1,-1\rangle$ and $|2,0\rangle$, two-photon transition were required (single photon magnetic dipole transition rule: $\Delta m_f = \pm 1$). This was achieved in the experiment by driving combination of a single MW photon with a single RF photon. Shown in figure 3.13 was the scheme used for two-photon Rabi oscillation.

MW + RF two-photon transition   Here, MW was fed into the cavity with frequency ω_{MW} and RF with frequency ω_{RF} fed from Z-trap wire, with a detuning of $\Delta = 2\pi \cdot 300$kHz to the intermediate state $|2,0\rangle$. ω_{MW} was detuned by $-\Delta$ with respect to $|1,-1\rangle$ and $|2,0\rangle$, and additionally, ω_{RF} that was detuned by $+\Delta$ with respect to $|2,0\rangle$ and $|2,1\rangle$. The total frequency combined ($2\pi\cdot6.834682$GHz) of the MW and the RF was still on resonant with state $|1,-1\rangle$ and $|2,1\rangle$. MW power input to the cavity was still 10dBm while RF amplitude fed into the Z-wire was V_{pp}=2V.

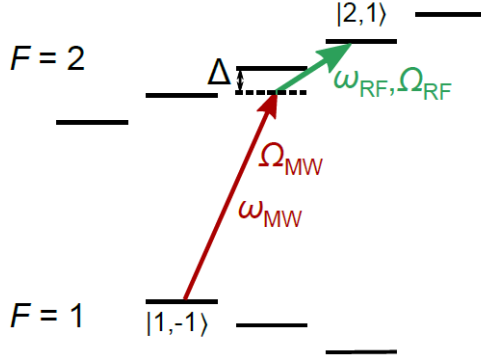[3]MW cavity field decay rapidly away from the chip surface, refer to Chapter 2.6 for the MW field distribution.

Figure 3.13: The level scheme for the cavity driven two-photon Rabi oscillations with ^{87}Rb hyperfine ground-state $|1,-1\rangle$ and $|2,1\rangle$. The cavity was driven with the MW ω_{MW} (red) and an additional external RF ω_{RF} (green) fed from Z-trap wire, with a detuning of $\Delta = 2\pi \cdot 300$kHz to the intermediate state $|2,0\rangle$. 10dBm of MW power were used in the cavity input while V_{pp} of 2V in RF amplitude was fed into Z-wire.

Measurement technique for two-photon Rabi oscillation Measurement technique was similar with the case of single-photon Rabi oscillation. The different being that there was an extra RF wave now. The MW and RF were switch on simultaneously via MW switch (same model for the RF switch, Mini-Circuits ZASWA-2-50DR). Atoms were hold in the persistent trap for the entire experiment time. During the holding time, MW and RF were turned on for t_{Rabi}. Finally, atoms number were measured and experimental cycle was repeated. The t_{Rabi} started with zero and increased by increment of 500μs for each experimental cycle. Experiment was consider completed where measurement points were good enough for fitting with the Rabi flopping equation.

Observation and Discussion

For this experiment, two-photon Rabi oscillation frequency were measured. More importantly, this measurement provided the $\pi/2$ pulse timing required in the Ramsey interference experiment (will be discussed in the coming section). Hence, unlike the case with one-photon Rabi oscillation, we did not change the cavity temperature as one of the measurement parameter here.

Rabi oscillation in this three level system looks complicated at first. However, given the condition of rotating wave approximation and if the intermediate state $|2,0\rangle$ was not populated, Rabi oscillation can be simplified to a two-level system consist of only state $|1,-1\rangle$ and $|2,1\rangle$, with Rabi frequency [143]:

$$\Omega_{2Ph} = \frac{\Omega_{MW}\Omega_{RF}}{\Delta} \tag{3.18}$$

This was achieved in the experiment by making sure the detuning is much more than both of the driving fields Ω_{MW} and Ω_{RF} ($\Delta \gg \Omega_{MW}, \Omega_{RF}$)[4].

---

[4]Recall that $\Delta = 2\pi \cdot 300$kHz, and $\Omega_{MW,RF} \sim 2\pi \cdot 10$kHz
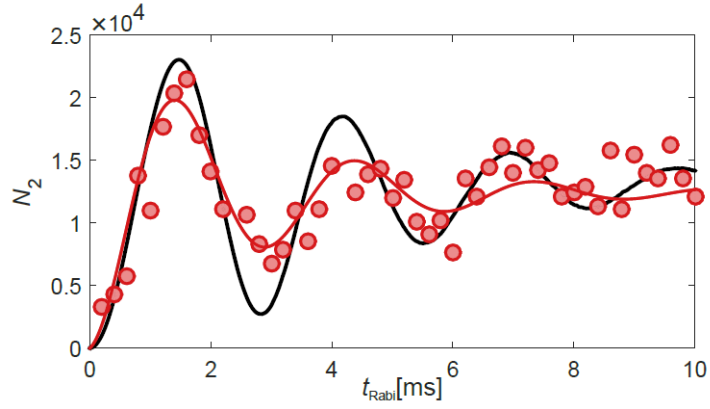
Figure 3.14: The figure shows two-photon Rabi oscillation measurement. Red circles are the measurement data points. Red line is the fitting using a damped sinusoidal function. Black line is the numerical simulation by assuming de-coherence is primarily contributed by the inhomogeneity of a MW cavity field seen by oscillating atomic ensemble in the magnetic trap. Two-photon Rabi oscillation with an improved coherence time of $\tau \approx 5$ms was observed.

Figure 3.14 shows the Rabi oscillation using two-photon transition. There was an improvement by a factor of 2 orders from changing single-photon to two-photon Rabi oscillation scheme, with $\Omega_{2\text{Ph}} = 2\pi \cdot 340$Hz. Improvement was expected due to the much lesser de-phasing of the two states $|1, -1\rangle$ and $|2, 1\rangle$ relative to the B-field. MW field inhomogeneity from the cavity was still the limiting factor for the relatively short coherence time ($\tau \approx 5$ms).

3.3 Direct Sensing of the Cavity Field Using Ultracold Atoms

Resonant Rabi oscillation measurement indicated that the ^{87}Rb ground state atoms are coupled with cavity MW photons. Here, this was further proven with a different experiment method via off-resonant cavity MW dressing.

3.3.1 AC Stark Shift

When a two level system interacts with an off resonant light ω_{dress}, the two level system will experience a shift in energy level δ_{dress}. This shift in energy is proportional to the light intensity Ω_{dress}^2 and inversely proportional to the detuning Δ. It is commonly known as AC Zeeman stark shift:

$$\delta_{\text{dress}} = \pm \frac{\Omega_{\text{dress}}^2}{\Delta} \tag{3.19}$$

For the case of ^{87}Rb ground state and a dressing cavity MW with linear polarization, there are 3 of these two-level states involved in AC stark shift for $|1, -1\rangle$ and $|2, 1\rangle$. Hence all of these AC stark shifts have to be taken into consideration for the total shift δ_{dress} in two-photon transition frequency $|1, -1\rangle \rightarrow |2, 1\rangle$ to be accurately known, shown in Figure 3.15.
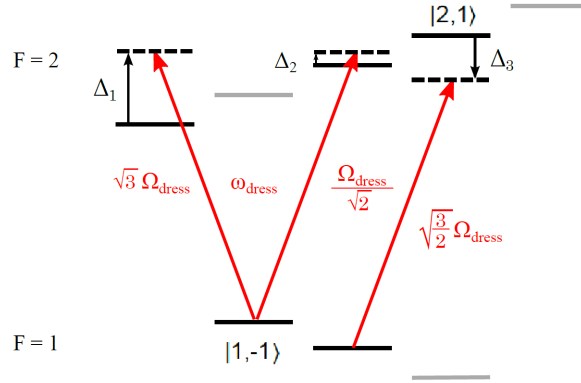
Figure 3.15: The level scheme for the off resonant dressing with the MW cavity field. Here we used linear polarized Ω_{dress} with the $\sigma+$ and $\sigma-$ components. All of the involved AC stark shifted states $\Delta_{1,2,3}$ with interaction strength $\sqrt{3}$, $1/\sqrt{2}$, $\sqrt{3/2}$ correspondingly have to be taken into consideration for the total shift between the states $|1, -1\rangle \leftrightarrow |2, 1\rangle$ to be known.

The total shift $|1, -1\rangle \leftrightarrow |2, 1\rangle$ is formulated to be [144]:

$$\delta_{\text{dress}} = -\Omega_{\text{dress}}^2 \cdot \left(\frac{3}{\Delta_1} + \frac{1/2}{\Delta_2} + \frac{3/2}{\Delta_3} \right) \tag{3.20}$$

3.3.2 Ramsey Interferometry

The Ramsey Fringes

In the case for Rabi oscillation, atoms interacted with a continues beam of radiation, this resulted in Rabi flopping. We now investigate what will happen if atoms interact with two separate radiation pulses, with a waiting time in between.

Consider now, the atoms interacted with radiation from time $t = 0$ to $t = t_\mathrm{p}$ and again from $t = t_\mathrm{Ramsey}$ to $t = t_\mathrm{Ramsey} + t_\mathrm{p}$. Shown in figure 3.16
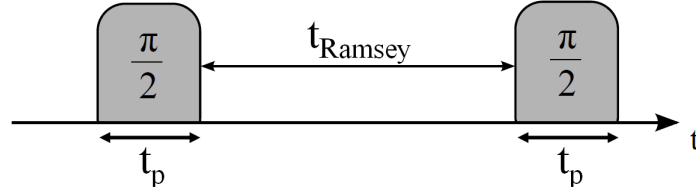
Figure 3.16: Time sequence for a Ramsey Interference. A two-level system interacted with $\pi/2$ pulse radiation from time $t = 0$ to $t = t_\mathrm{p}$ and again from $t = t_\mathrm{Ramsey}$ to $t = t_\mathrm{Ramsey} + t_\mathrm{p}$, with a separation time of $t = t_\mathrm{Ramsey}$.

Integration of equation 3.6, using initial condition $c_2(0) = 0$ and rotating wave approximation, we got [142]:

$$c_2(t) = \frac{\Omega^*}{2}\left\{\frac{1 - \exp[i(\omega_0 - \omega)t_\mathrm{p}]}{\omega_0 - \omega} + \exp[i(\omega_0 - \omega)t_\mathrm{Ramsey}]\frac{1 - \exp[i(\omega_0 - \omega)t_\mathrm{p}]}{\omega_0 - \omega}\right\}$$

(3.21)

The second pulse produced a similar term with a phase factor $\exp[i(\omega_0 - \omega)t_\mathrm{Ramsey}]$. The amplitude of the excited state $|c_2|^2$ gives:

$$|c_2|^2 = \left|\Omega\frac{\sin\{(\omega_0 - \omega)t_\mathrm{p}/2\}}{(\omega_0 - \omega)}\right|^2 + \left|1 + \exp[i(\omega_0 - \omega)t_\mathrm{Ramsey}]\right|^2$$

(3.22)

$$= \left|\frac{\Omega t_\mathrm{p}}{2}\right|^2\left[\frac{\sin((\omega_0 - \omega)(t_\mathrm{p}/2))}{(\omega_0 - \omega)(t_\mathrm{p}/2)}\right]^2\cos^2\left(\frac{(\omega_0 - \omega)t_\mathrm{Ramsey}}{2}\right)$$

(3.23)

Let's simplify the equation by using $\delta = \omega_0 - \omega$, where δ is the frequency detuning of the radiation from the two-level system. With $t_\mathrm{p} = \pi/2$-pulse and small δ, we got:

$$|c_2|^2 \approx \cos^2\left(\frac{\delta t_\mathrm{Ramsey}}{2}\right)$$

(3.24)

This showed that for a Ramsey interference, the population of the states oscillate with the frequency of the detuning. This oscillation was called Ramsey fringes. The Ramsey interference method provides a beat measurement between the frequency separation of a two level system and the radiation field.

Experimental Procedure

$\pi/2$ **pulse calibration** $\pi/2$-pulse is the timing for a pulse width, for which an atom initially in ground state $|0\rangle$ are put to a superposition of $(|0\rangle + |1\rangle)/\sqrt{2}$. For our case, a $\pi/2$-pulse put $|1, -1\rangle \rightarrow (|1, -1\rangle + |2, 1\rangle)/\sqrt{2}$. Duration of the $\pi/2$-pulse can be determine from two-photon Rabi oscillation measurement. For the Ramsey interference experiment, $\pi/2$-pulse of 500μs was used. (Note: From figure 3.14, atoms took 2.8ms to complete a Rabi cycle. An ideal $\pi/2$-pulse should had a pulse width of 700μs, this parameter do not need to be exact for the Ramsey fringes measurement.)

Measurement technique for Ramsey Interference Here, Ramsey interference method was employed to investigate the magnitude of the AC Zeeman stark shift δ_{dress} contributed by the cavity MW dressing. For that, dressing MW photons were fed into the cavity continuously with fixed power of 10dbm and with a dressing frequency ω_{dress}. For the $\pi/2$-pulse required in Ramsey pulse sequence, two-photon $\pi/2$-pulse were used using RF driven in Z-wire and MW driven via microwave antenna located outside the vacuum chamber, with frequencies of ω_{RF} and ω_{extMW} correspondingly. The parameter for RF and MW used for $\pi/2$-pulse were kept the same with two-photon Rabi oscillation measurement, with the only difference being that the ω_{RF} was detune for -2π·500Hz. Each Ramsey fringes measurement was done with the initial waiting time t_{Ramsey} starting at 3ms with increment of 200μs for each experiment cycle, and stop at a t_{Ramsey} where the Ramsey fringes were good enough for fitting. The same procedure then repeated with another dressing frequency ω_{dress} ranges from 2π·6.834GHz to 2π·6.848GHz. Identical measurement was conducted with cavity temperature set at 6.2k, 6.4k, 6.6k, and 6.8k. Figure 3.17 summarized the parameter used for the Ramsey interference measurement.

Observation and Discussion

The Ramsey interference method provides a beat measurement between the frequency separation of a two level system (in our case, $|1, -1\rangle \leftrightarrow |2, 1\rangle$) and the driving field ($\omega_{\mathrm{RF}} + \omega_{\mathrm{extMW}}$). For an example shown in Figure 3.18, the two-photon detuning with respect to the atomic transition frequency $|1, -1\rangle \rightarrow |2, 1\rangle$ was set to -2π·500Hz. Without the MW dressing, this will result in a measured Ramsey interference frequency $\omega_{\mathrm{Ramsey}}/2\pi$ of -500Hz. The presence of a dressing MW Ω_{dress} in the cavity shifts the atomic transition frequency to -2π·500Hz + δ_{dress}. AC stark shift δ_{dress} can then be easily obtained and MW dressing intensity can be calculated using equation 3.20. Hence, the Ramsey interference method provides the direct measurement of MW intensity in the CPW resonator.
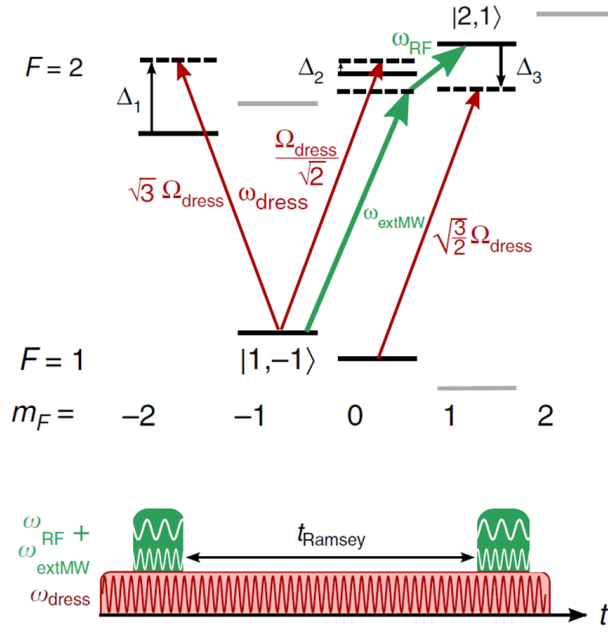
Figure 3.17: **Top:** Level scheme of the ^{87}Rb ground-state manifold. The external MW and RF frequencies used for driving the two-photon transitions for the Ramsey scheme (green) and the off-resonant coupling of the cavity field to the relevant states are shown(red). **Bottom:** Atoms were prepared in a superposition state of $|1, -1\rangle$ and $|2, 1\rangle$ with a two-photon $\pi/2$-pulse using RF fed into Z-wire and MW fed into an external antenna with frequencies ω_{RF} and ω_{extMW} correspondingly (green). After a variable waiting time t_{Ramsey}, a second $\pi/2$-pulse was used and population in the two states ($|1, -1\rangle$, $|2, 1\rangle$) was measured to obtain Ramsey fringes. Dressing MW with frequency ω_{dress} was fed into the cavity throughout the Ramsey sequence (red).
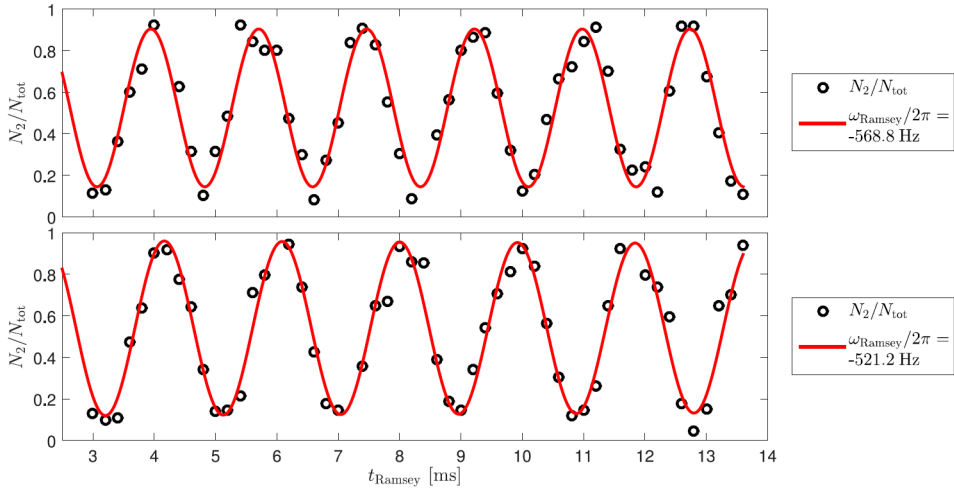
Figure 3.18: Examples of Ramsey fringes for two different MW cavity dressing frequencies ω_{dress}. Black circles are measurement points of Ramsey interference with different waiting time t_{Ramsey}. Red lines are fitting with a sinusoidal wave. Inlet shows the fitted Ramsey frequency ω_{Ramsey}. **Top:** $\omega_{\mathrm{dress}}/2\pi$= 6.838GHz yielding a shift of $\delta_{\mathrm{dress}}/2\pi$=-68.8Hz. **Bottom:** $\omega_{\mathrm{dress}}/2\pi$= 6.843GHz yielding a shift of $\delta_{\mathrm{dress}}/2\pi$=-21.2Hz

Probing the Off-resonant Cavity Field with Ultracold Atoms Sets of δ_{dress} with a variation of cavity temperatures (6.2k, 6.4k, 6.6k, and 6.8k) and cavity MW dressing frequencies ω_{dress} were measured. The intensity of the cavity MW dressing Ω^2_{dress} was calibrated using equation 3.20. Figure 3.19 displays the relation between δ_{dress} measured and its corresponding dressing intensity Ω^2_{dress}. Similar patterns between the measured dressing intensities Ω^2_{dress} and the measured transmission spectra of the MW resonator were observed. This can only mean that atoms are interacting with only the MW photons in the cavity, giving further proof of the atom-cavity coupling. There was a small shift between the Lorentzian fits and the measured transmission spectra, this have to be further investigated.
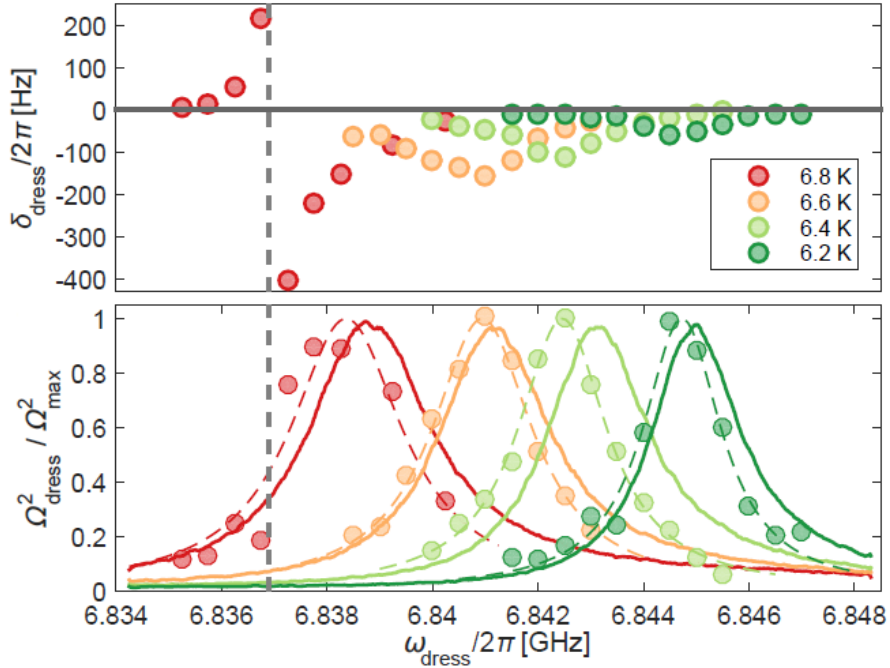
Figure 3.19: **Top:** Measured AC stark shift δ_{dress} versus frequency of the MW cavity dressing field ω_{dress} in the superconducting microwave resonator for different chip temperatures. Dispersion curve measured (red circles) occurred because of $|1,0\rangle \rightarrow |2,1\rangle$ resonant transition, where $\Delta_3=0$ in Figure 3.15. **Bottom:** Calculated microwave intensity Ω^2_{dress} based on the measurements of δ_{dress} (top) by using equation 3.20. The colour dashed lines are Lorentzian fits to the data points. The solid lines are the measured transmission spectra of the microwave resonator.

3.4 Chapter Closing

In this chapter, coupling of ground state ^{87}Rb atoms to a CPW resonator via methods of resonant excitation and off-resonant MW dressing was presented. Due to the low single-ground state atom single-photon coupling strength of $g \sim 2\pi \cdot 0.5$Hz, coupling effect can only be observed by driving of the cavity field. This leads to high photon number[5] ($n_\text{photon} \gg N_\text{atom}$), where cavity field behaves as a classical wave. Hence atoms coupled individually and no collective effect can be exploited with this condition.

Furthermore, short coherent time in the experiment will be a limitation of creating high fidelity superposition state. The inhomogeneity seen by atomic ensemble can in principle reduce by cooling it further, producing smaller cloud size. There are also experiments that demonstrated a more robust scheme of Rabi pulses using optimal control theory [145, 146] to optimize for a longer coherence time.

Coupling strength g by all means can also be increased by trapping atoms closer to CPW resonator or by adopting a CPW resonator with a smaller mode volume such that B-field density per photon is higher. With the same reasoning, other resonator structures such as lumped element resonators which have a much smaller mode volume can be used for enhancement of coupling strength too.

Coupling ground-state atoms to the cavity, although is still in weak coupling regime, is interesting in its own. Phenomena such as superadiance [147], collective effects [148], enhancement of the coherence time, the effect of thermal photons [149] on lifetime and more can be observed in this regime. Numerous experiments can still be accomplished by using ground state ^{87}Rb atoms.

The aim for strong coupling regime is set to be the priority. In next chapter, the author will demonstrate by switching from a ground-state atoms to a Rydberg state, he is one step closer to achieving this goal.

---

[5]It was estimated that with Rabi Oscillation of 20kHz via resonant driving of MW fields, there were $\sim 10^9$ cavity photons.

Chapter 4

Towards Coupling of a Single Rydberg Atom to a Coplanar Waveguide(CPW) Resonator

In this chapter, the implementation of Rydberg atoms in the experimental setup will be shown. As mentioned before in the thesis, Rydberg atoms have electric dipole allowed transitions in the MW range. Compared with magnetic dipole transitions in ^{87}Rb ground-state atoms, electric dipole transitions give an improvement of $\frac{1}{\alpha}$ in transition strength, where α is the fine-structure constant. In addition to that, the scalability n^2 in the dipole moment indicates that the high principle quantum number n in Rydberg atoms will be a significant contribution factor in coupling strengths too.

The outcome of utilizing Rydberg atoms (n>50) is an amazing improvement of single-atom coupling strength from sub-Hz to $\sim$MHz. However the advent of Rydberg atoms also involves some complication. High polarizability make Rydberg atoms highly sensitive to surrounding electric fields. It will be later shown in this chapter, the presence of unwanted strays electric fields on the chip surface will ultimately prevent the creation of Rydberg atoms with very high quantum number n.

Firstly, Electromagnetically Induced Transparency(EIT) as a technique for surface stray E-field measurement [150] will be presented, followed by detection of single Rydberg atom through E-field ionization. Finally, the feasibility of driving MW transitions between neighboring Rydberg states via cavity photons will be shown.

4.1 Electromagnetically Induced Transparency(EIT)

4.1.1 Experiment setup

One of the common methods to create Rydberg atoms is via two-photon optical excitations. We adopted this method for our EIT experiment, using collimated 780nm and focused 480nm laser light. A compensation electrode plate is located $\sim$4mm under the chip for creation of arbitrary E-field in the Z-direction. As shown in figure 4.1:
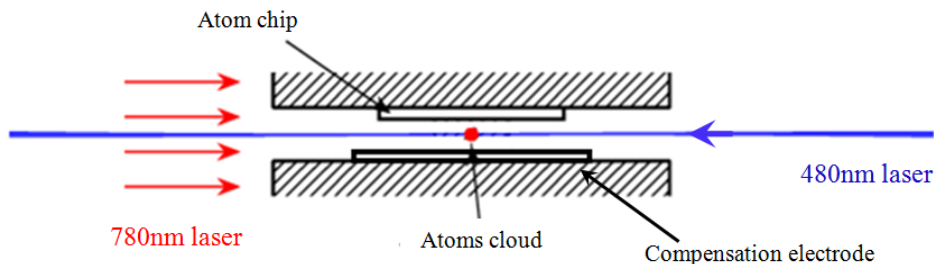
Figure 4.1: Experimental setup for Electromagnetically Induced Transparency(EIT). Collimated 780nm(red) and focused 480nm(blue) laser light that propagates in the opposite direction is directed to the atomic cloud. A compensation electrode plate is located $\sim$4mm under the chip for creation of arbitrary E-field. (Figure drawn not to scale)

EIT Laser Parameter A 780nm laser with 150μW and $\sim$1cm in diameter, was already available as imaging light in our setup, resonance with the $5^2S_{1/2}$(F=2) $\rightarrow 5^2P_{3/2}$(F=3) transition. The 480nm light was set to be on resonance with $5^2P_{3/2}$(F=3) to the desired Rydberg states $nS_{1/2}$ or $nD_{3/2,\,5/2}$, frequency was calibrated using a wavemeter (Model: High Finesse WS7-60). Our 480nm laser was acquired from the frequency doubling of a 960nm high power laser. The 480nm laser light had laser power of 20$\sim$30mW (power depends slightly on blue laser frequency) and was focused into focus width of $\sim$50μm, Shown in figure 4.2:

EIT Concept There are two common ways of explaining the effect of EIT [151]. The most popular explanation being the quantum destructive interference between excitation pathways yielded the transparency [152]. Here, we used the dress state picture for explanation [153]. When both 780nm and 480nm lasers were on resonance with their corresponding states (480nm laser intensity $\gg$ 780nm laser intensity), the intermediate states will experienced Autler-Townes splitting [154], shown in figure 4.3.
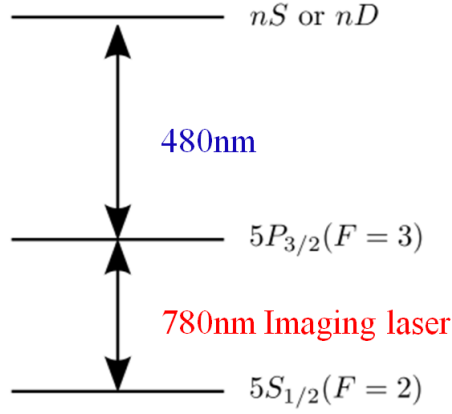
Figure 4.2: Three level cascaded scheme for Electromagnetically Induced Transparency(EIT). 780nm Imaging light is on-resonant with $5^2S_{1/2}$(F=2)$\rightarrow$$5^2P_{3/2}$(F=3) while 480nm light will set to be on resonant with $5^2P_{3/2}$(F=3) to the desire Rydberg state.

Figure 4.3: Autler-Townes splitting picture. Both blue and red lasers were on resonance with their corresponding states, with frequency ω_c and ω_p (left). In the case where the Rabi oscillation of the blue laser was much higher than red laser, $\Omega_c \gg \Omega_p$. A dress state $|e\rangle \pm |i\rangle$ was formed with an energy spliting of $\hbar\Omega_c$ (right). Now, the red laser with ω_p was detune from resonance level, resulting in less adsorption from the medium. Hence, the transparency.

The splitting prevented the absorption for the 780nm lasers. The lack of absorption of the imaging laser (780nm) will creates a transparency within the vicinity in the atom cloud, such as shown in Figure 4.4. This is a handy method for assuring resonance condition for the 480nm laser light.

Figure 4.4: One of the first Electromagnetically Induced Transparency (EIT) observed in the setup, using $30S_{1/2}$ Rydberg state for excited state, $5^2P_{3/2}$(F=3) for intermediate state and $5^2S_{1/2}$(F=2) for ground state. The atom cloud was released from the optical dipole trap after shifted under the atom chip. Imaging light (780nm red laser) and 480nm laser light was turned on (via triggering AOM) simultaneously after time-of-flight of 10ms, with exposure time set to 100μs. EIT was observed 1mm under the chip, this was the focusing point of the 480nm blue laser.

4.1.2 DC stark shift

The DC Stark effect is the shifting and splitting of spectral lines of atoms due to the presence of an external DC electric field. Polarizability α_0 of Rydberg atoms scale with n^7, making it highly sensitive to stark shift:

$$\Delta E = -\frac{1}{2}\alpha_0 F^2 \tag{4.1}$$

Take note that the equation for quadratic stark shift is valid only for small E-fields with low orbital quantum number $l = 0$.

Calibration of the Compensation Voltage   By varying the electric field F via voltage applied V to the compensation plate, DC stark shift ΔE can be measured using EIT method. A stark map simulation, which is the numerical calculation of Rubidium Rydberg Stark spectra [155] by means of direct diagnolization of the energy matrix was available from the work of Dr. Jens Grimmel [156][1]. By comparing the DC stark shift measurements with the stark map, compensation voltage V can be calibrated with the electric field F, shown in figure 4.5:

---

[1]This method will not be discussed in this thesis. Please refer to PHD thesis of Dr. Jens Grimmel for detail explanations.

Figure 4.5: Measurement of DC stark shift for $30S_{1/2}$ using EIT positioned 1mm under the chip. 780nm laser is on resonant with $5^2S_{1/2}$(F=2)$\rightarrow$$5^2P_{3/2}$(F=3) and blue circles are measurement points of 480nm detuning ΔE for maximum transparency to equivalent E-field(F). The red color line is quadratic fitting using equation 4.1 while the green color line is Stark shift calculation obtained by direct diagonalisation of the Hamiltonian. Both methods fit well in the low E-field region and no measurable stray E-field is detected at this position. Calibration of electric potential V applied to compensation electrode plate to E-field is V=0.36F. In agreement with formula F=V/d, with separation d of $\sim$4mm between chip (grounded) and electrode plate.
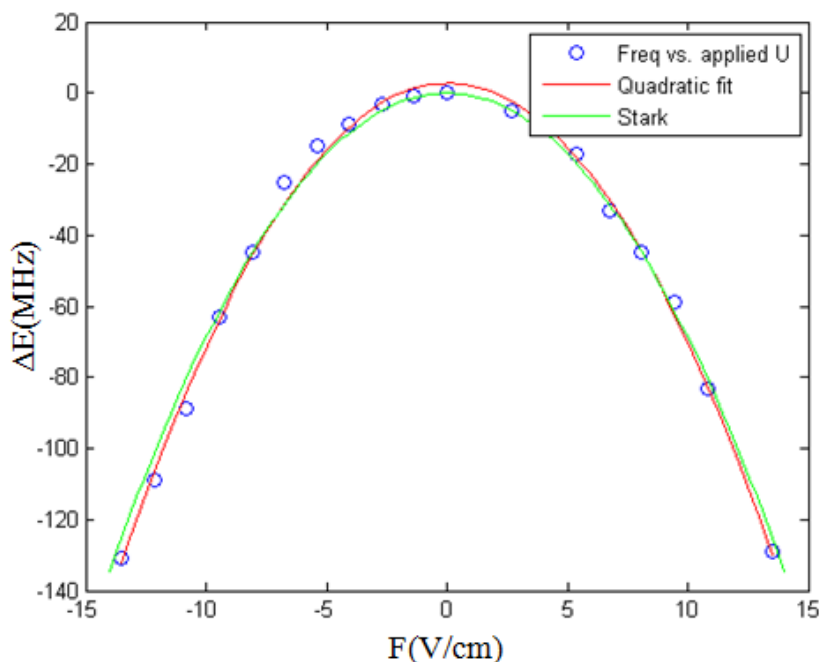
4.1.3   Stray Electric fields Close to Chip Surface

Moving the EIT closer to the CPW resonator   To create EIT close to the CPW resonator, atomic ensemble was trapped above the CPW resonator gap using the procedure mentioned in chapter 3. The difference here being that the final Z-wire current was set to 0.22A instead of 0A, and there was no final RF evaporation cooling to increase the atom number. Without a current running in the Z-wire, there was no defining electric potential of the Z-wire, and the EIT excitation linewidth was observed to be broadened (in $\sim$300MHz range for 39D Ryd-state). This was also the reason where atomic ensemble was trapped $\sim$40μm above the CPW resonator now (instead of 20μm with 0A in Z-wire, mentioned in chapter 3, figure 3.7). Then, 480nm focused light was shifted to $\sim$40μm above CPW resonator (focused into the atom cloud). EIT can only be observed in this position with the blue laser detuned and with compensation potential turn on, as shown in figure 4.6.

The DC Stark shift measurement was then repeated at this position. Figure 4.7 shows the DC Stark shift measurement using $36S_{1/2}$.
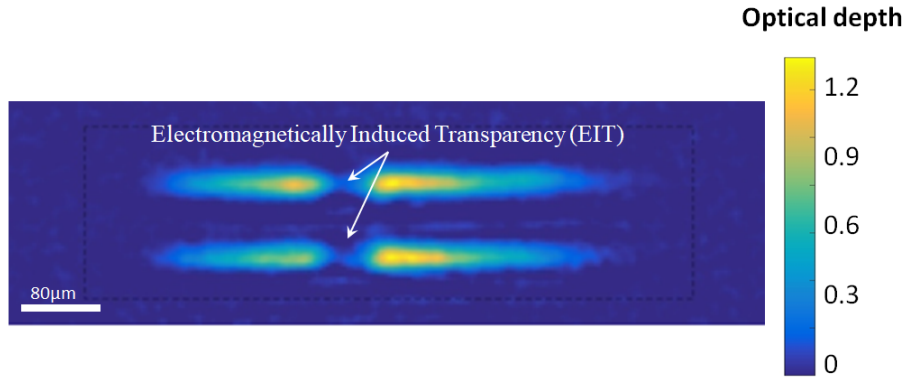
Figure 4.6: The figure shows 10^5 atoms trapped $\sim 40\mu$m above the coplanar waveguide (CPW) resonator, with reflection absorption imaging method. The EIT was observed using $36S_{1/2}$ Rydberg state for excited state, $5^2P_{3/2}$(F=3) for intermediate state and $5^2S_{1/2}$(F=2) for ground state. The EIT condition was fulfilled only when blue laser was detuned. This indicates the presence of background bias electric fields in the vicinity.
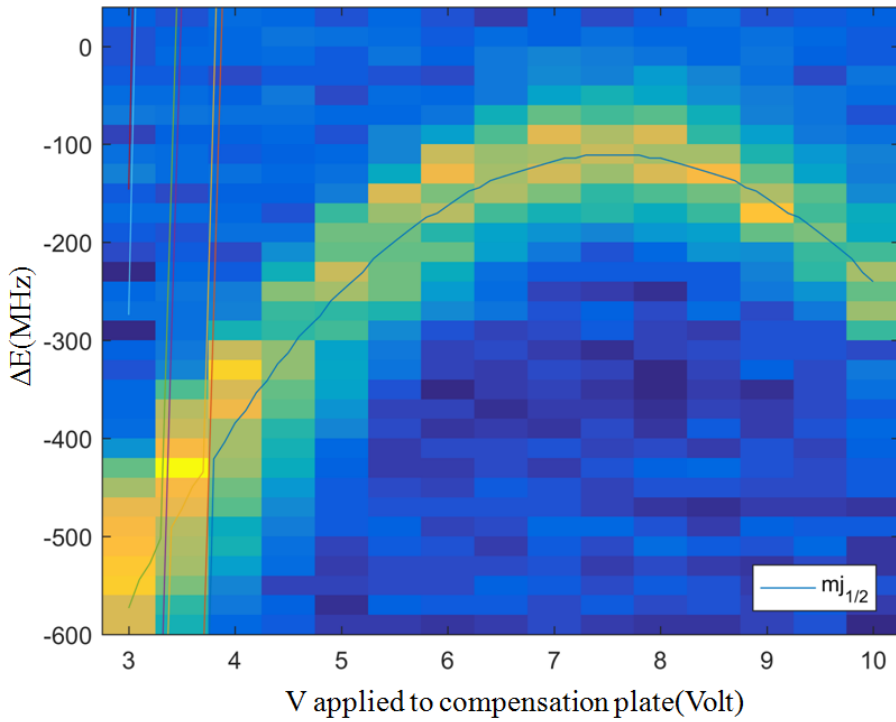
Figure 4.7: Figure shows measurement of Rydberg state $36S_{1/2}$ stark shift against compensation potential V with color scale. Yellow shows strong EIT transparency and blue indicate no EIT. Minimum detuning occurs at compensation potential of 7.5V with $\Delta E \sim$ -120MHz and width of $\sim$100MHz. Solid curve is the fitting of $m_j = 1/2$ sub-state from stark map, stark map is shown in the following figure 4.8.
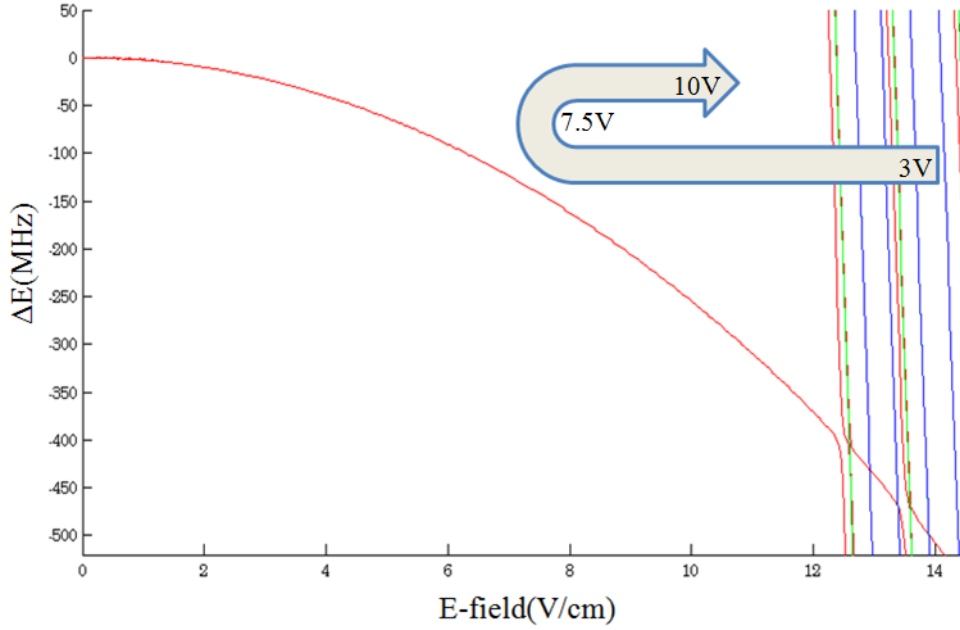
Figure 4.8: Figure shows here is the $36S_{1/2}$ stark map shown as fitting in the figure 4.7. Grey color arrow indicates the magnitude of compensating potential V shown as x-axis in the figure 4.7 from 3V⇒10V, electric field compensation started with compensation potential at 3V, to an optimum compensation potential ≈7.5V resulting in the minimum electric field, and then overcompensation of electric field for compensation potential >7.5V. Detuning for minimum electric field occur at $\Delta E \sim$ -120MHz, correspond to $\sim$ 7V/cm of remaining stray electric field at the EIT position. EIT width of $\sim$100MHz indicates a strong E-field gradient of about 2V/cm over the 480nm beam focus size ($\sim$50μm).

Observation and Discussion EIT was observed only when the compensation E-field F was turned on and with detuning of the 480nm laser. This indicates the presence of background bias electric fields in the vicinity. The existence of E-fields close to the proximity of the chip is primarily due to adsorbates of Rubidium that are deposited on the chip surface over time [157, 158]. Since the compensation electrode plate in our setup is only capable of offsetting the E-fields component perpendicular to the chip, the remaining orthogonal component is uncompensated. In the next section, this uncompensated E-field of $\sim$7V/cm will be shown to set a boundary for the candidate of Rydberg state for cavity coupling.

4.2 Selection of a Rydberg State Pair for Cavity Coupling

Limitation in going into higher Rydberg state Figure 4.9 displays as an example of how the stark map for a highly excited Rydberg state generally looks like. As seen, the energy levels quickly turn into a chaotic region in relatively low E-field. Due to Rydberg states mixing within this region with other higher Rydberg states, a reduction in coupling strengths will occur. Also, the Rydberg energy levels ΔE change greatly with only a small variation in the E-field, making Rydberg states in this region prompt to de-phasing. Hence, the excitation of Rydberg state into these regions have to be avoided.
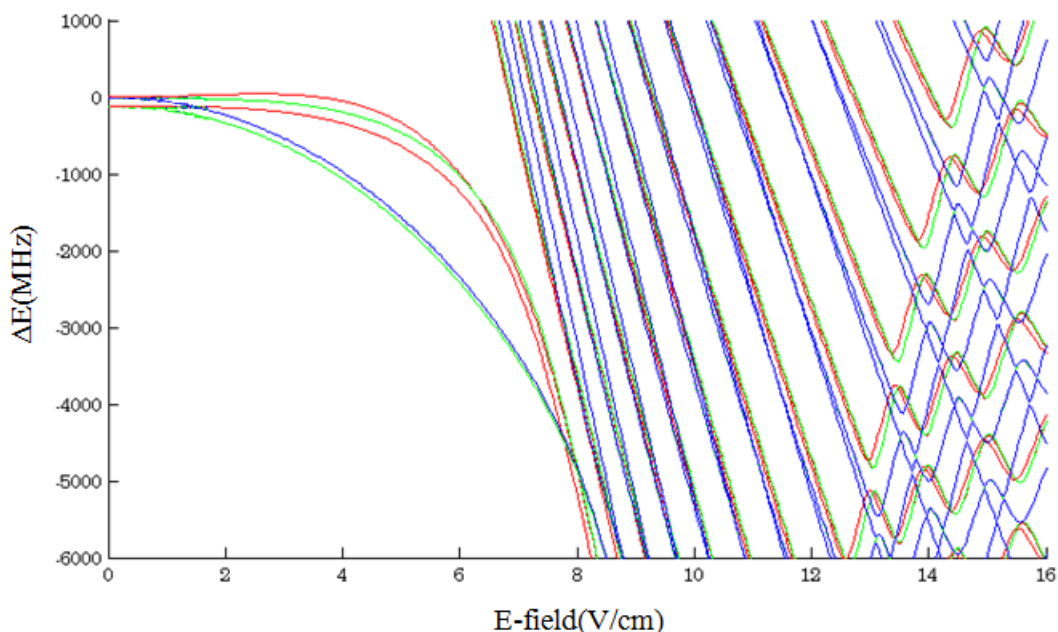
Figure 4.9: Stark map of the $46D_{3/2,\ 5/2}$ Rydberg state. State mixing starts at the E-field region of 8V/cm. This region has to be avoided due to decrease in coupling strength. With our stray E-field strength of $\sim$7V/cm, this will be the highest Rydberg state we can use for cavity coupling.

Choosing the Rydberg State Since coupling to the cavity is our main objective here, we need to prepare Rydberg state that has a dipole allowed transition within range of the cavity resonant frequency $\omega_{\text{Ryd}} \approx \omega_{\text{Cav}}$. The 3rd harmonic of our CPW resonator with $\omega_{\text{Cav}} \sim$20.5GHz was used, as already acknowledged in Chapter 2. Given with the stray E-field of $\sim$7V/cm and requirement of neighboring Rydberg transition frequency $\omega_{\text{Ryd}} \sim$20.5GHz, the only choice left is the $39D_{5/2} \leftrightarrow 38F$ Rydberg state pair, with energy diagram shown in figure 4.10.
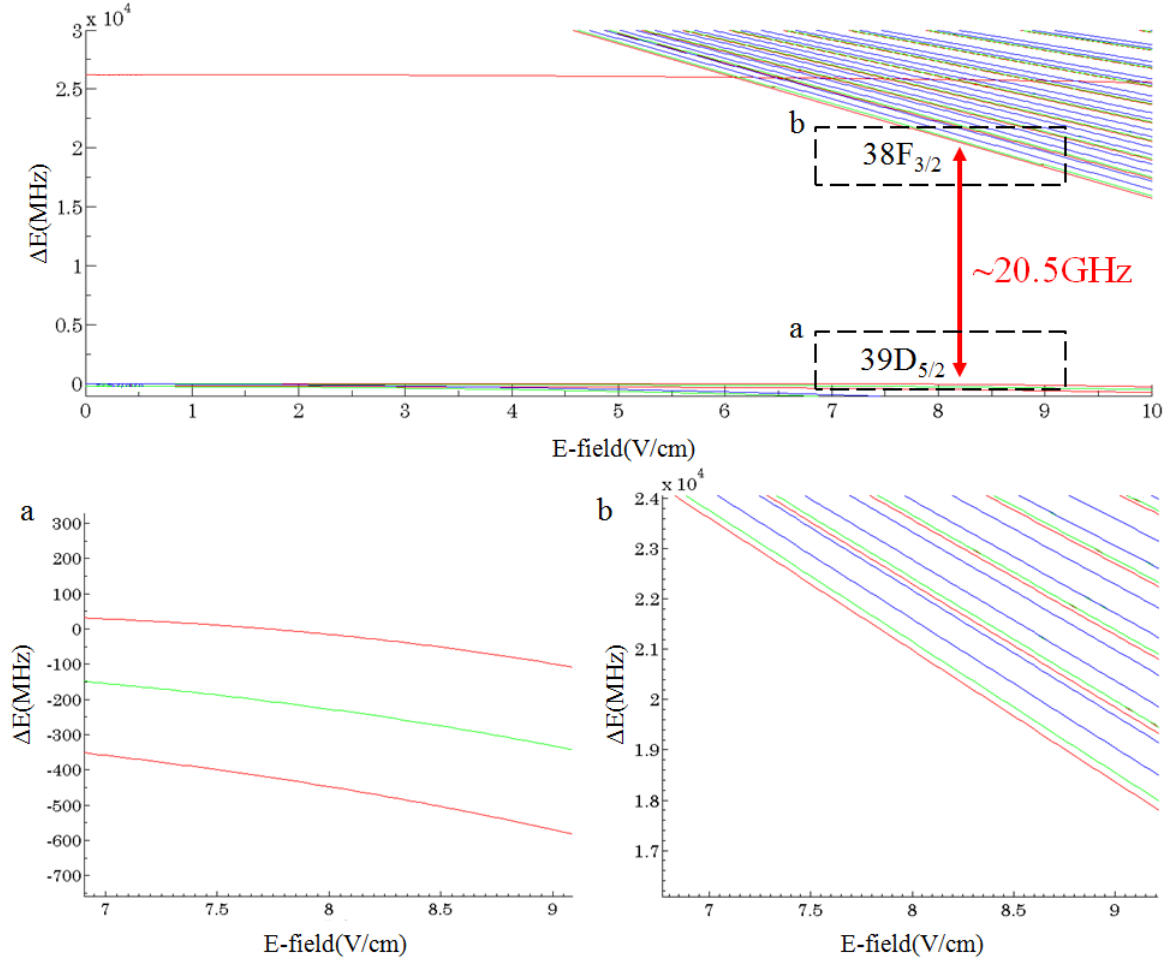
Figure 4.10: The $39D_{5/2}$ Rydberg state is chosen for atom-cavity coupling in our experiment. Given the condition of E-field $\sim$7V/cm and a neighboring state $38F_{3/2}$ with electric dipole transition frequency of $\omega_{\mathrm{Ryd}} \approx \omega_{\mathrm{Cav}} \sim$20.5GHz, shown in the top figure with red arrow. The two dotted boxes labeled as **a** and **b** show the region of interest for atom-cavity coupling. Enlarge pictures are shown in the bottom figure with **a** and **b** correspond to $39D_{5/2}$ and $38F_{3/2}$ Rydberg state.

Stark shift measurement for 39D Rydberg state To ascertain the laser frequency detuning ΔE with its equivalent E-field, the Stark shift measurement of $39D$ state (Shown in figure 4.11), and its corresponding Stark map (Shown in figure 4.12) was shown.
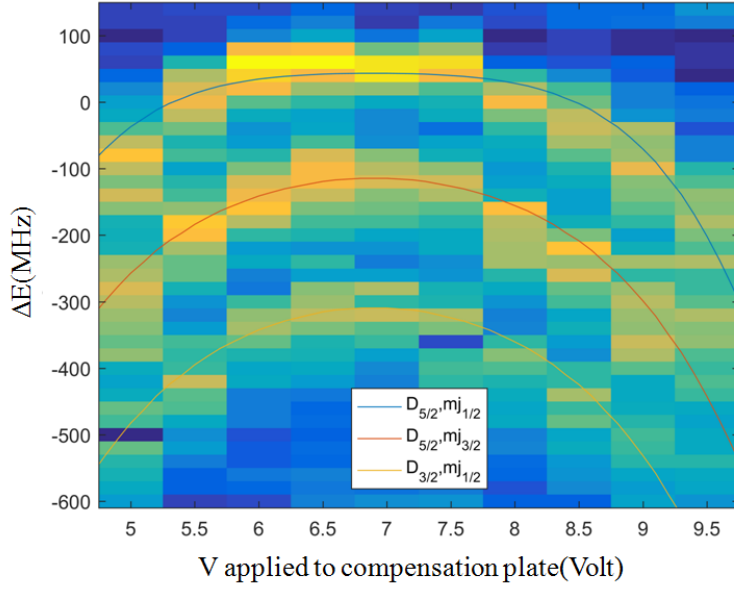
Figure 4.11: The Stark shifts measurement of 39D Rydberg state with color scale. Yellow shows strong EIT transparency and blue indicates no EIT. Only the three least Stark-shifted states are shown here, with inlet showing the marker for $|m_j|$.
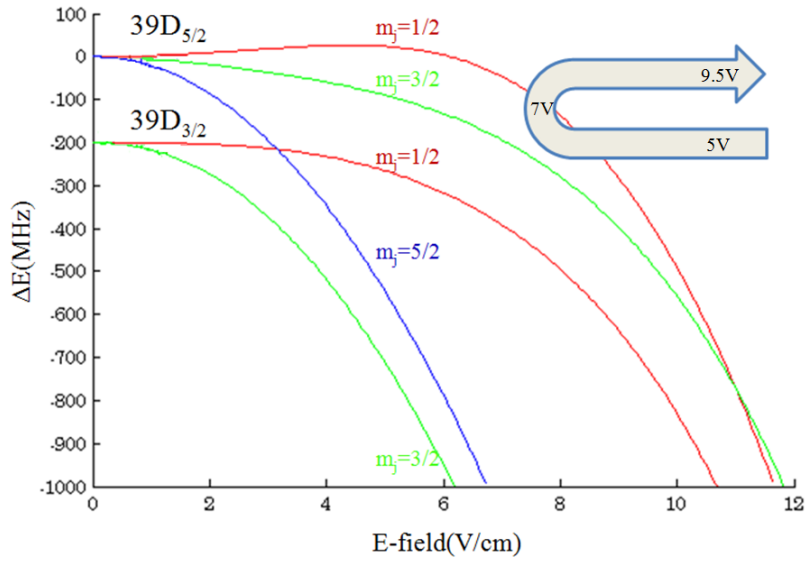
Figure 4.12: 39D stark map shown as fitting in the figure 4.11. Gray color arrow indicates the magnitude of compensating potential V, shown as x-axis in the figure 4.11 from 5V⇒9.5V, electric field compensation started with compensation potential at 5V, to an optimum compensation potential ≈7V resulting in the minimum electric field, and then overcompensation of electric field for compensation potential >7V. This reconfirmed the minimum stray E-field as ∼7V/cm. Note that there is a small difference in optimum compensation potential compare to figure 4.8, this is due to the stray electric field long term drift which has not yet been quantified.

50

4.3 Single Rydberg Atom Excitation and Detection

Laser Parameter   Excitation of ground-state atoms to Rydberg atoms is rather straight forward. Merely a small modification was required for our EIT scheme. Here, 780nm red laser and 480nm blue laser are detuned from the intermediate state $5P_{3/2}$ by Δ=160MHz, with laser power of $\sim$5mW and $\sim$30mW correspondingly. To avoid undesirable Rydberg-Rydberg interaction, $\leqslant$1 Rydberg atom on average was created at a time. Hence, the excitation time of only 1μs is required. Both 780nm and 480nm laser were triggered via AOM simultaneously. Shown as follows in figure 4.13:
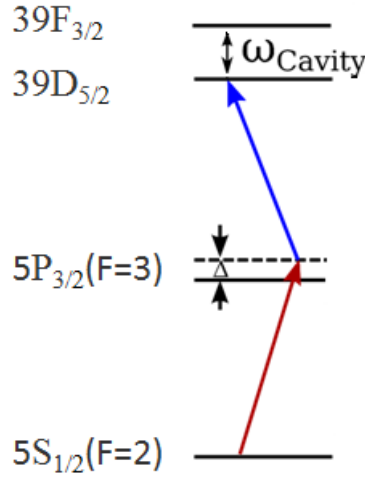
Figure 4.13: Driving a ground state atom to $39D_{5/2}$ Rydberg state via two-photon excitation. The 780nm red laser and the 480nm blue laser are detuned from the intermediate state $5P_{3/2}$ by Δ=160MHz. The length of laser pulses is reduced to 1μs to create a single Rydberg atom at a time. Further interactions with cavity photons at frequency ω_{cavity} can be discovered by detection of the $38F_{3/2}$ Rydberg state.

4.3.1 Selective Field Ionization(SFI)

Detection of single Rydberg atoms is highly efficient with the selective field ionization(SFI) method [159]. In SFI, a Rydberg atom is subjected to a time-dependent increasing electric field. Eventually, the field strength is large enough to rip the electron away from the atom, ionizing the Rydberg atom. Depending on the specific states, Rydberg atoms in different quantum states and therefore at different time will ionize at different field strengths. The positively charged ion is then accelerated by the field and hits a detector, which then produces a signal. Figure 4.17 shows an example for SFI measurement demonstrated using $34D_{5/2}$ and $36S_{1/2}$ state.

Experimental Apparatus and Details

We applied selective field ionization method for Rydberg atoms detection in our setup, the experimental layout was shown in figure 4.14 and figure 4.15
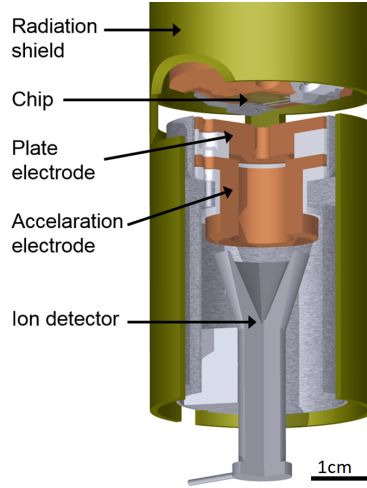
Figure 4.14: In the SFI detection scheme, the plate electrode is ramped from the compensation potential to above ionization potential for Rydberg atom ionization. Acceleration electrode provides further accelerates and guides the ion into the detector. The ion detector is an electron avalanche tube where signal get amplified and detected as a current pulse.
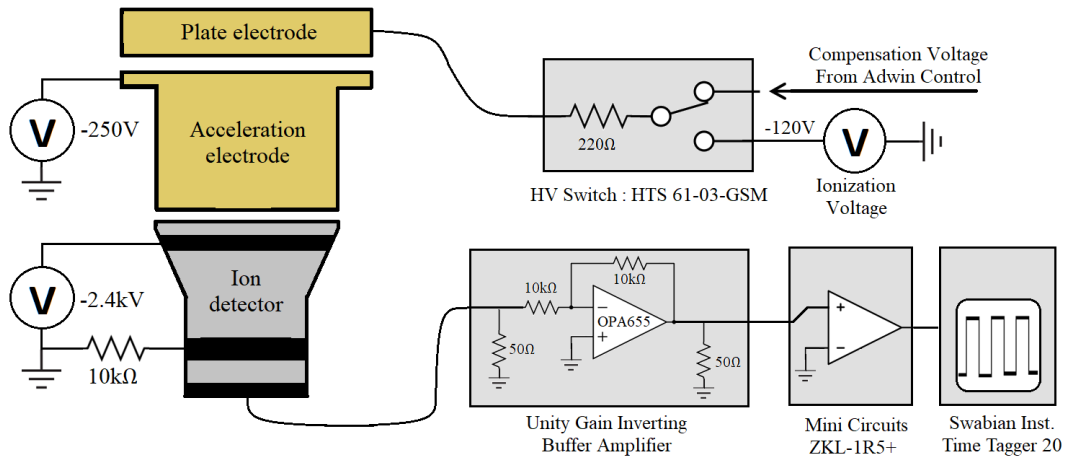
Figure 4.15: Electronic equipment layout for the Rydberg field ionization measurement. The plate electrode is connected either to the compensation voltage or the ionization voltage using a high voltage (HV) switch. The switching was controlled via ADwin digital output. The acceleration electrode and ion detector are set at a fixed voltage of -250V and -2.4kV correspondingly. The signals from the ion detector are then increased through a series of amplifiers before getting recorded by a time-to-digital converter (time tagger). Refer to text for more details.

Shown in figure 4.15 is the electronic layout for the Rydberg field ionization measurement. The plate electrode was used for compensation of the E-field during excitation of Rydberg atoms, and only switched to ionization voltage (-120V) during Rydberg ionization. For this reason, the plate electrode was connected to a HV switch made by the electronic workshop (model: HTS 61-03-GSM). The switch was capable of switching between positive V and negative V, where we set our compensation voltage (+7.5V) using the ADwin analog output and ionization voltage (-120V) using a benchtop power supply (model: Voltcraft VSP26534E). The ionization E-field ramping rate was controlled via the resistance inside the HV switch, which we set to 220Ω. This gave the voltage ramp from +7.5V $\rightarrow$ -120V within 3μs.

The acceleration electrode and the ion detector were connected to a HV power supply individually, made by electronic workshop (model: HV-Nr-7479), each set to -250V and -2.4kV. To improve the detection signal strength, the lower electric potential in the ion detector was slightly biased away from the electric ground potential (0V) with a 10kΩ HV resistor.

For our measurement data acquisition, a time tagger (time-to-digital converter, it records the arrival time of a pulse) was employed (model: Swabian Inst. Time Tagger 20). The tagger only addresses a pulse when it's greater than +1V. For this reason, two amplifiers were used for signal inversion and amplification. First, a unity gain inverting buffer amplifier was used to invert the ion signal into a positive value. This buffer amplifier used an inverting amplifier configuration, consisting of a pair of 10kΩ resistors and an operational-amplifier (OPA655), with input and output impedance set to 50Ω by resistors. Secondly, the signal was then amplified by a high gain amplifier (model: Mini Circuits ZKL-1R5+). Together with these two amplifiers, a single ion signal with initial value of -25mV can be amplified to +1V. Figure 4.16 shown was a single ion signal after the amplification.

The recorded ion signals time from the tagger were then stored in a computer for data analysis.
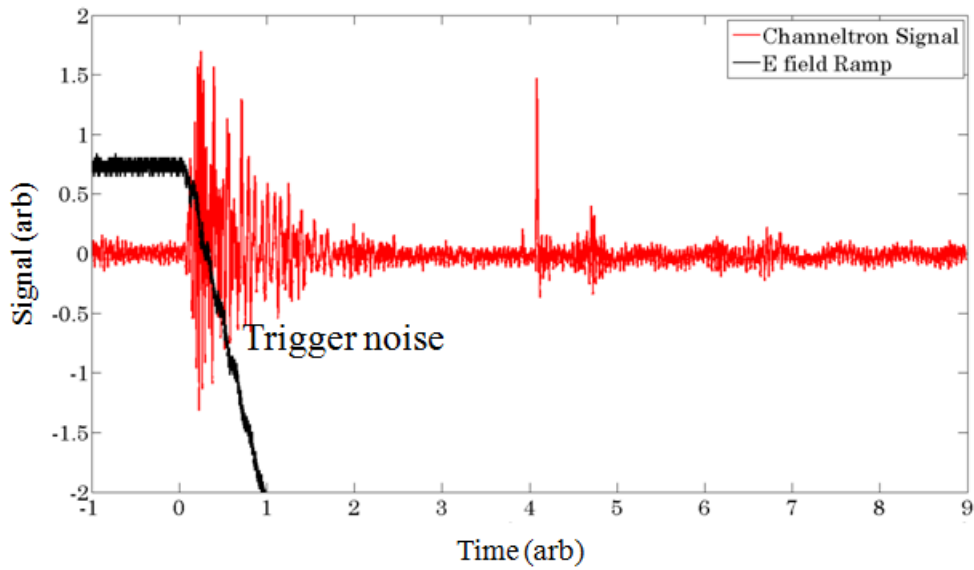
Figure 4.16: Demonstration of a single Rydberg atom detection. Compensation E-field(black) is ramped to a high negative value at T=0 using a HV switch, ionizing the Rydberg atom. This created a trigger noise(red) in the signal line that damps away quickly, not affecting the readout. The ion is then detected as a pulse at T=4.
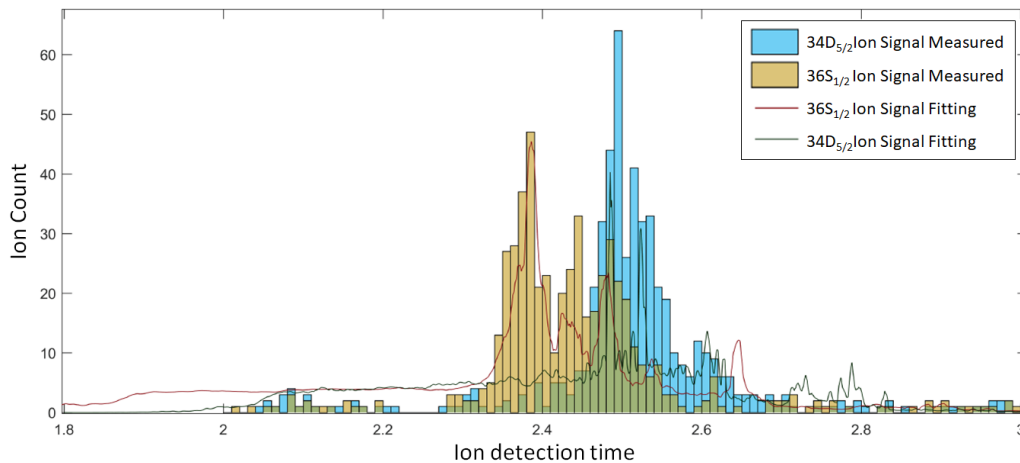
Figure 4.17: The figure demonstrates a single Rydberg atom detection. Compensation E-field(black) is ramped to a high negative value at T=0 using a HV switch, ionizing the Rydberg atom. This created a trigger noise(red) in the signal line that damps away quickly, not affecting the readout. The ion is then detected as a pulse at T=4.

4.3.2   Limitation in Selective Field Ionization(SFI)

The classical ionization E-field for 39D and 38F is 160V/cm and 155V/cm correspondingly. This small separation in the ionization E-field makes it hard to differentiate the states in time scale[2]. Moreover, the classical ionization E-field does not show the whole picture of the ionization process. If the time evolution in E-field for both 39D and 38F states were taken into consideration, both Rydberg states will evolve into the same path during the E-field ramping, making ionization of these two states indistinguishable in time[3], shown in figure 4.18. Even with optimized shaped E-field ramping [160], detection time of these two states could not be separated. Figure 4.19 shows the simulated optimized E-field ramping and ion detection for both Rydberg states.
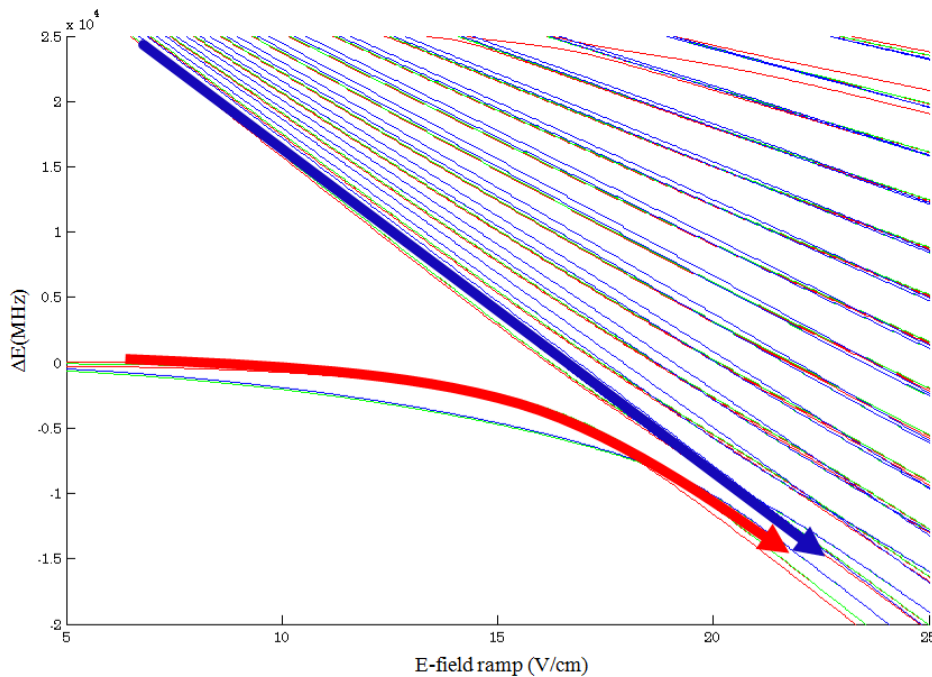
Figure 4.18: Here shows the state evolution during the ramping of ionization field. Blue arrow indicates 38F Rydberg state and the red arrow indicates 39D Rydberg state. Both states eventually evolve into the same path, resulting in similar ion detection time.

---

[2]In a typical experiment, E-field was ramped from 0→200V/cm within 3μs, ionization time separation calculated using classical ionization limit for 39D and 38F is ∼10ns.

[3]Since we are detecting a single Rydberg atom at a time, the same measurement had to be conducted multiple times for statistical accuracy. Similar ionization time for 38F and 39D Rydberg state will result in the overlapped distribution of the ion signal detection time.
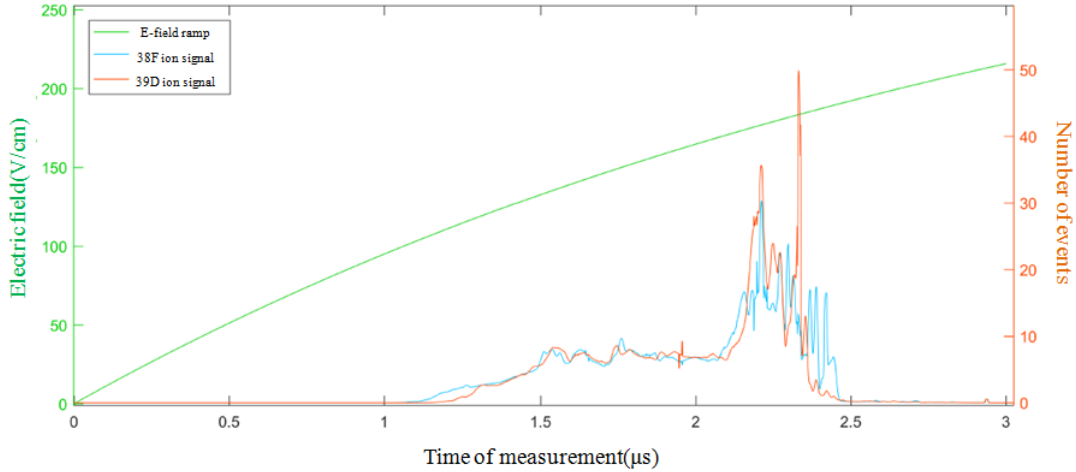
Figure 4.19: Simulation of an ionization E-field ramping (Shown in green, $0\rightarrow200$V/cm in 3μs) and its corresponding ion detection for 38F and 39D Rydberg states sum over 200 events. Both signals overlap completely and could not be differentiated, making state detection impossible. Simulation obtained by courtesy of Dr. Markus Stecker, for more information refer to his PHD thesis.

4.3.3   State Selective De-Excitation

To overcome the impossibility to discriminate between 39D and 38F states detection, an optical de-excitation scheme to depopulate the 39D state just before ramping the ionization field was implemented. Hence, ideally the only ions detected will be contributed by the 38F Rydberg state. Our de-excitation light which is called "blowing light" here, is a 480nm light with pulse width of 1μs. Blowing light is on resonance with $5^2P_{3/2}$(F=3)$\leftrightarrow$39$D_{5/2}$(m_j=1/2) transition state with 30mW of laser power. With lifetime of only 30ns, the $5^2P_{3/2}$ state then quickly decay to $5^2S_{1/2}$ ground state, effectively emptying the $39D_{5/2}$(m_j=1/2) state. Figure 4.20 shows the difference in the ion counts without and with blowing light.

With the implementation of the blowing light, interaction between cavity MW photons and 39D Rydberg atoms was able to be detected, through the presence of 38F Rydberg atoms. In the next section, a measurement showing the first hint of Rydberg atom-cavity coupling will be described.
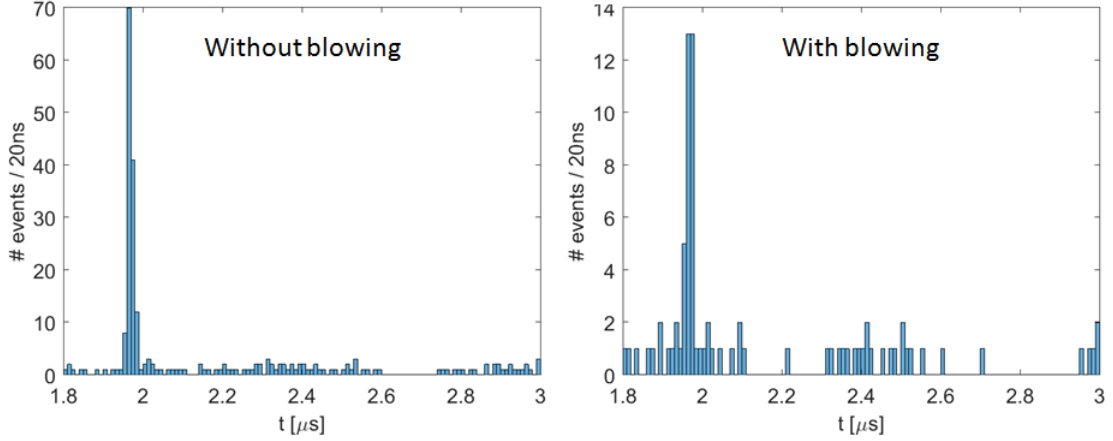
Figure 4.20: The figure shown above is the histogram of the ion counts over 300 pulse sequences, plotted with 20ns timing window. Here $39D_{5/2}(m_j=1/2)$ Rydberg state is prepared and held for $2\mu s$ before ionization take place. E-field ramping is set such that ions arrived at $\sim 2\mu s$ at the detector. With 300 excitation-detection events, there were ~ 150 Rydberg atoms detected, this gives a single Rydberg atom excitation probability of about 0·5 for each event. The difference between histograms is with blowing light set off/on. Here, we achieve a high blowing efficiency of 80%. Blowing efficiency is not perfect mainly due to the exposure of background RF noises: During the $2\mu s$ hold time, undesirable RF noises in our ground conductor is capable of driving $39D_{5/2}(m_j=1/2)$ to other m_j sub-states, making it transparent to blowing light. In addition to that, black body radiation and spontaneous decay of 39D Rydberg state also contributed to a reduction in blowing efficiency.

4.4 Coupling a single Rydberg Atom to Cavity MW

4.4.1 Experimental Procedure

In this experiment, a single Rydberg atom of $39D_{5/2}(m_j=1/2)$ state was prepared at $\sim 40\mu m$ above the CPW resonator gap. The E-field was compensated to $F=8.2$V/cm such that stark shifted resonance frequency to 38F state is $\omega_{\mathrm{Ryd}}=20.55$GHz. Chip temperature was set to 4.5K ,this corresponds to the 3rd harmonic cavity resonance frequency of $\omega_{\mathrm{Cav}}\approx 20.55$GHz coinciding with ω_{Ryd}. Next, a MW pulse ω_{drive} of 250ns is used to drive the resonator[4]. Lastly, the presence of 38F Rydberg state was detected. The MW pulse frequency is set as variable here, with 2MHz steps.

Timing sequence for Rydberg atom excitation and detection Since we used only one single Rydberg atom at a time for cavity interaction, the same mea-

---

[4]Due to the deterioration of the MW connections and amplifier inside the vacuum chamber, MW field strength in the CPW resonator could not be accurately estimated. MW pulse width of 250ns was chosen such that pulse time > cavity rise/decay time$\sim$50ns

surement had to be done multiple times for statistical accuracy. Here, 300 identical measurements were conducted within a single experimental cycle, utilizing the same atomic ensemble.
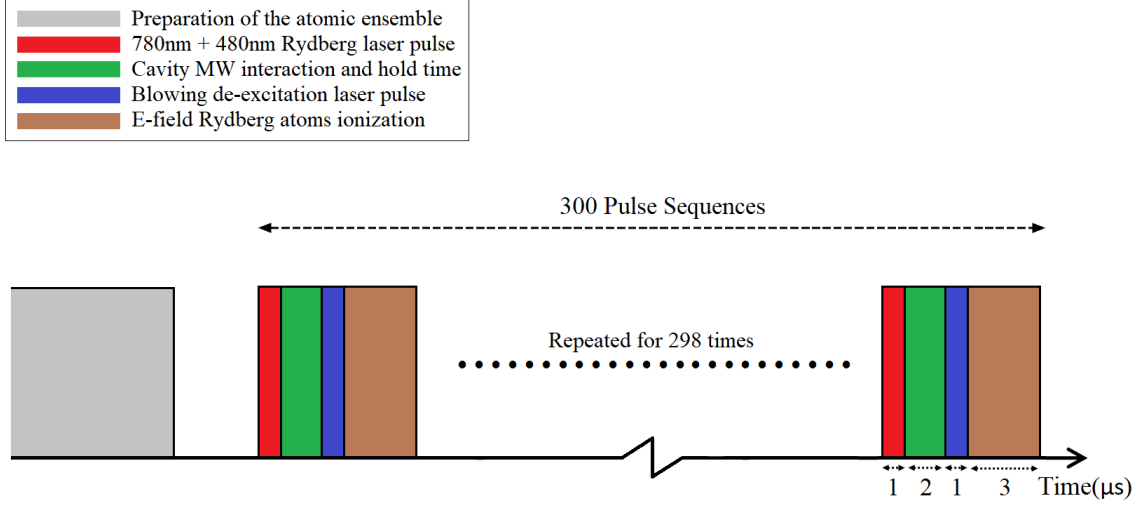
Figure 4.21: The timing sequence of Rydberg excitation, cavity MW interaction, optical de-excitation and detection for a single experiment cycle. Atoms were prepared and trapped at $\sim 40\mu$m above the CPW resonator (gray). During the trap holding time, a single Rydberg atom was created by optical excitation for 1μs (red), followed by 2μs of interaction and wait time (green), 1μs of blowing light (blue), and E-field ionization within 3μs (brown). This process was repeated for 300 times with a repetition rate of 30kHz before the atoms were released from the CPW resonator and the experiment cycle was completed.

Shown in figure 4.21 is the timing sequences of the experimental cycle. Gray color area indicates the process of the atomic cloud preparation (MOT loading $\mapsto$ Sisyphus cooling $\mapsto$ optical pumping $\mapsto$ magnetic quadrupole trapping $\mapsto$ magnetic transfer $\mapsto$ Ioffe trap $\mapsto$ RF cooling $\mapsto$ Optical dipole trapping $\mapsto$ transfer to atom chip Z-trap $\mapsto$ Z-trap shifting via external bias B-field $\mapsto$ persistent SC trap within CPW resonator). After the preparation, atoms were trapped at $\sim 40\mu$m above the CPW resonator, and will be trapped here until the end of the experiment cycle, with a typical holding time of 15ms.

During the holding time, 300 pulse sequences [Rydberg excitation (red) $\mapsto$ interaction time (green) $\mapsto$ blowing light (blue) $\mapsto$ E-field ionization (brown)] were conducted, with a repetition rate of 30kHz. With the probability of 0.5 to excite a single Rydberg atom, we managed to excite ~ 150 Rydberg atoms in a single experiment cycle.

In chapter 4.3.3, the blowing efficiency was characterized. The only difference there was with blowing light turn off/on, the timing of the Rydberg excitation to the E-field ionization was still the same: 2μs of waiting time with 1μs of extra waiting time for the case of blowing light turn off, else, 2μs of waiting time with 1μs of blowing light. Then, came the E-field ionization. As mentioned, a blowing efficiency of 80% was archived.

4.4.2 Observation and Discussion

Figure 4.22 shows the result of this measurement. The increased in ion counts at $\omega_{\text{drive}} \sim 20.55\text{GHz}$ is the presence of 38F Rydberg atoms, where a single Rydberg atom at 39D state was excited by a cavity MW photon into the 38F Rydberg state. This result demonstrated that Rydberg atoms interact with cavity MW photons, indicating atom-cavity coupling. 3rd harmonic cavity linewidth at 4.5k ($\kappa \sim 30\text{MHz}$) also agreed well with the excitation linewidth shown here. In this position using 39D Rydberg state with improved coupling strength of factor $\sim \frac{n^2}{\alpha}$,we estimate a single atom-single cavity photon coupling strength of $g/2\pi=40\text{kHz}$. Although this is a large increase with respect to the ground state atom coupling of $g/2\pi=0.5\text{Hz}$, it is still not in the strong coupling regime where at least $\sim$MHz is required.
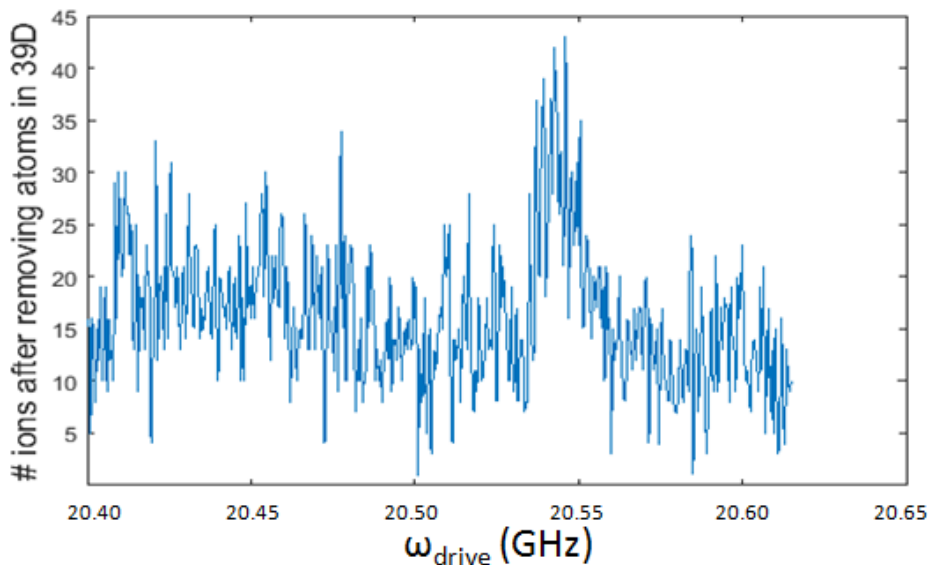
Figure 4.22: Remaining ion counts sum over 300 events after the blowing scheme versus frequency of MW pulse. As we can see in the plot, there is a background ion count due to the inefficient of blowing. Fluctuations are also an issue that will have to be resolved in the near future. However, the increased in ion counts at $\omega_{\text{drive}} \sim 20.55\text{GHz}$ is undeniably the presence of 38F Rydberg atoms, where we set the cavity resonance frequency (via temperature of the chip) to coincide with the Rydberg transition frequency ($\omega_{\text{Cav}} \approx \omega_{\text{Ryd}} \approx 20.55\text{GHz}$).

The interaction of Rydberg atoms with MW cavity photons had to be re-validated using other methods to assure only the cavity MW photons were interacted with the Rydberg atoms. These methods includes:

1. Driving the cavity with MW frequency ω_{drive}, where $\omega_{\text{drive}} \neq \omega_{\text{cav}}$ and $\omega_{\text{drive}} = \omega_{\text{Ryd}}$. If only the cavity photons can be seen by the Rydberg atoms, one shall see no Rydberg atom in 38F state. This can be done by either changing the cavity temperature, or using another compensation E-field for a different ω_{Ryd}.

2. Rabi oscillation measurement. Intensity inside the cavity is greater compare to outside the cavity by the Q-factor. Hence much higher Rabi oscillation frequency will be measured if Rydberg atoms only interact with the cavity photons.

4.5   Chapter Closing

In this chapter, the presence of stray E-fields close to the vicinity of the chip surface was detected. Stray E-fields limit the preparation of very high Rydberg states, resulting in 39D state as the only candidate available for atom-cavity coupling. The complication arose due to the state selective detection of 39D and 38F is then addressed and tackle via "blowing" scheme. Finally, measurement of atom-cavity MW interaction was shown.

This chapter also concludes the contribution of the author during these two years of research experience in Tübingen. Even though a lot had been accomplished regarding atom-cavity coupling, the goal of strong coupling regime is yet to be reached. In the final chapter, the outlook of this experiment will be discussed.

Chapter 5

Conclusion and Outlook

5.1 Conclusion

In this thesis, coupling of ^{87}Rb ground state atoms to a superconducting CPW resonator was demonstrated. The coupling of Rydberg atoms to a superconducting CPW resonator was also shown to be plausible. These are important steps towards the implementation of a cold atom quantum memory for microwave photons.

An atom chip consisting of two main structures was used for the experiment: A Z-trap for magnetic trapping of neutral ^{87}Rb atoms and a coplanar waveguide (CPW) resonator for atom-cavity coupling. The CPW resonator was an inductively coupled superconducting half wavelength resonator, with a fundamental mode resonance frequency of 6.84GHz and a linewidth of $2\pi \cdot 3$MHz (Q-factor of $\sim 10^3$) at a temperature of 6K. In addition, the CPW resonator has a third harmonic mode resonance frequency of ~ 20.55GHz at a temperature of 4.5K .For Rydberg atom-cavity coupling, the third harmonic mode was used.

Measurements of resonant Rabi oscillations as a function of chip temperature revealed the interaction of ground state ^{87}Rb atoms with the cavity microwave (MW) photons. When the transmission frequency of the resonator was shifted closer to the atomic transition (via changing chip temperature), higher Rabi frequency was measured.

Direct evidence of atom-cavity coupling was done through off-resonant MW dressing. MW field strengths in the cavity were measured with AC Stark shift and Lorentzian curves were observed. Similar patterns of the Lorentzian curves and the cavity transmission proved the coupling of ^{87}Rb ground state atoms to the CPW resonator. Trapped at a distance $\sim 20\mu$m above the CPW resonator, a single ground state atom-single cavity photon coupling strength of $\sim 2\pi \cdot 0.5$Hz was estimated.

By scanning the MW frequency in the cavity, excitation from $39D$ to $38F$ Rydberg state was observed when the resonance condition was fulfilled. This demonstrated the interaction of MW photons and Rydberg atoms. Trapped at a distance $\sim 40\mu m$ above the CPW resonator, a single $39D$ Rydberg state atom-single cavity photon coupling strength of $\sim 2\pi \cdot 40$kHz was estimated.

5.2 Outlook

To be a good quantum memory, it is essential to write a single photon into an atomic ensemble, preserve its coherence for long storage times and then retrieve the information of this photon, while maintaining a high write/retrieve efficiency. Hence, it is required to strongly coupling an atomic ensemble to a superconducting resonator. Making sure, a single photon will interact with an atomic ensemble in a resonator before escaping the cavity.

In the experiments reported in this thesis, the strong coupling regime is not yet reached. To achieve strong coupling, the coupling strength $g/2\pi$ needs to be larger than the cavity linewidth of $\sim 2\pi \cdot 3\mathrm{MHz}$ [1]. The collective effect of Rydberg atoms can be used to improve the coupling strength, this however, has to be carefully implemented due to the long Rydberg-Rydberg interaction length. The strong coupling regime can also be achieved by using higher Rydberg state, and by trapping Rydberg atom closer to the CPW resonator. These, however requires the stray E-fields on the chip surface to be further reduced.

Coating the chip surface with a layer of rubidium has been shown to improve the homogeneity of the stray E-field [161], nevertheless, this will hinder the functionality of the CPW resonator. Since Rubidium adsorbate is the main contributor for stray E-field, Light-induced atomic desorption (LIAD) can be an effective method for desorbing Rb from the chip [162]. However, LIAD is only effective on a dielectric surface, where the majority area of the chip currently used is metallic. It is possible to coat a layer of dielectric on top of the atom chip, but the localized charges on the dielectric surface is an upcoming issue. Another possible method is to dress the Rydberg atoms with microwave fields to modify the polarizability [163], reducing the AC Stark shift. In the appendix, the possibility of adding additional compensation electrodes on the orthogonal axis was considered.

Other than reducing stray E-field on the surface, stability of the experiment had to be improved. Our group is currently developing STIRAP method for coherent excitation of Rydberg atoms. This will greatly reduce the stability requirement of 480nm and 780nm lasers in terms of intensity fluctuations. Phase locking of 480nm and 780nm lasers to a frequency comb had also been implemented [2]. Other than that, the polarizations of 480nm and 780nm have to be considered [3]. It was observed that the electrical ground noise in the laboratory is surprisingly large in the RF range, a cleaner electrical ground is necessary to reduce undesirable Rydberg transition between Rydberg m_j states.

With these problems solved, Strong coupling of Rydberg atoms to a CPW resonator can be achieved.

---

[1] Cavity linewidth is equivalent to cavity photons loss rate κ. Here, we neglect the atoms lifetime.

[2] It was previously locked to a wave meter with a resolution of 2MHz and significant frequency long term drifts.

[3] Linear polarized light was used previously for all Rydberg experiments, without considering in details about σ_+ and σ_- component.

Appendices

Appendix A

E-fields compensation parallel to the chip surface

In the present setup, external E-field can only be applied perpendicular to the chip surface. In this section, the idea of inserting additional electrodes for E-fields compensation along the atom chip surface was taken into consideration. Note that in the appendix, we re-define the axis notation, unlike in the main text where z-axis is the direction perpendicular to the atom chip.

A.1 Compensation with macroscopic wire

Consider the case of two long electrically insulated copper wires laying above an atom chip. The wires are separated by a distance of 4mm, and have a diameter of 200μm each. The atom chip is electrically grounded, and an electric potential is applied to each of the wires, with potential V_1 and V_2, shown in figure A.1

Figure A.1: Two long insulated copper wires laying above an electrically grounded atom chip, with electric potential V_1 and V_2 applied to each of them. The wires are 200μm in diameter, and separated by a distance of 4mm. The X and Y axis indicate the area of interest for the E-fields, with the Y-axis perpendicular and the X-axis parallel to the atom chip.

With a potential $V_1 = -150V$ and $V_2 = +150V$ applied to the wires, the electric

fields in the x-component were simulated using Comsol[1], as shown in figure A.2.
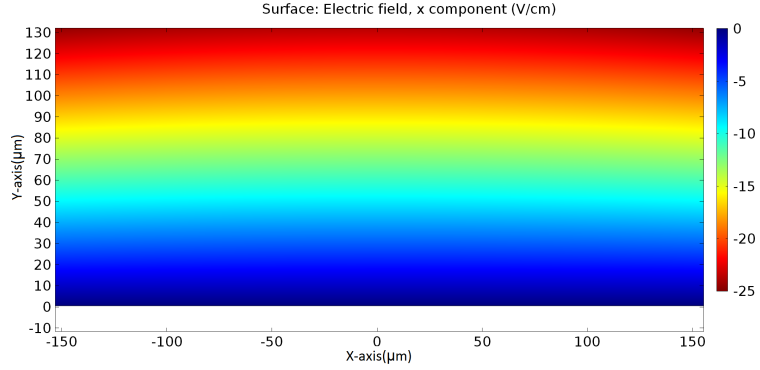
Figure A.2: Simulation of the E-field in x-component with $V_1 = -150V$ and $V_2 = +150V$. An E-field in the range of $\sim$7V/cm was simulated at the position $\sim$40μm above the chip, similar in range to the uncompensated stray E-fields previously detected in the experiment. However, at the same time, a high E-field gradient in the y-direction was created.

With the uncompensated stray E-fields due to absorbate in the ranges of $\sim$7V/cm at position $\sim$40μm above the CPW resonator[2], these E-fields created will be capable in canceling the stray E-fields, further reducing the DC Stark shift of the Rydberg atoms. Besides that, the E-field gradient created in the y-direction is also capable in reducing the absorbate E-field gradient, increasing the uniformity of the overall E-fields.

For compensation of the E-field gradient in x-direction, the case of using different magnitude in electrode potential were considered, with $V_1 = -100V$ and $V_2 = +200V$, shown in figure A.3. Here, no significant E-field gradient was observed.
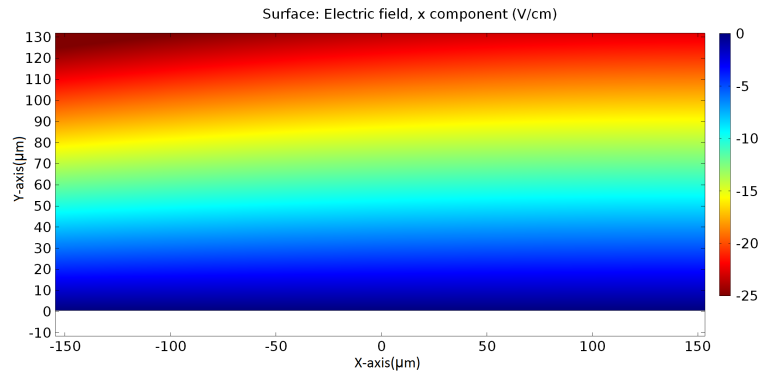
Figure A.3: Simulation of the E-field in x-component with $V_1 = -100V$ and $V_2 = +200V$. E-field gradient in x-direction created was negligible, even with high magnitude difference $\Delta(|V_2| - |V_1|)$=100V.

---

[1]Here we only interested in the E-field region close to the chip surface. With potential=$\pm$150V, E-field created will be huge in further distances.

[2]For more details regarding stray E-fields close to the chip surface, refer back to chapter 4.1

A.2 Compensation with microscopic atom chip electrodes

In this section, the use of microscopic atom chip electrodes is considered. Compared with macroscopic wires, the atom chip electrodes can be located closer to each other without obstructing chip structures, such as the Z-trap wire and CPW resonator. Hence, much smaller potentials can be used to obtain the same compensation E-field. Of course, to implement this idea, modification of the current chip design would be required.

Consider the case of two long electrically insulated copper strip electrodes laying on the surface of the atom chip. The strips are separated by a distance of 1mm, and have a width of 100μm each. The atom chip is electrically grounded, and an electric potential is applied to each of the strips, with potentials V_1 and V_2, as shown in figure A.4
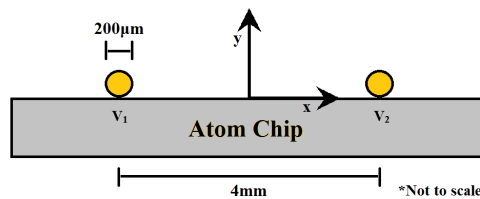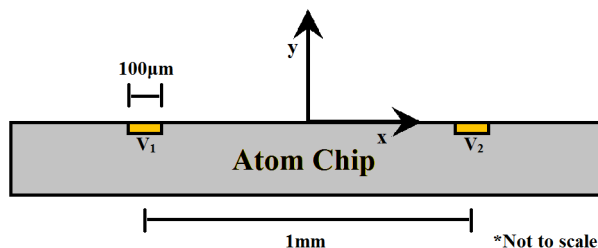

Figure A.4: Two long insulated copper strip electrodes laying on the same surface with the electrically grounded atom chip, with electric potential V_1 and V_2 applied to each of them. The strips are 100μm in width, and separated by a distance of 1mm. X and Y axis indicate the area of interest for the E-fields, with the Y-axis perpendicular and the X-axis parallel with the atom chip.

With potential $V_1 = -20V$ and $V_2 = +20V$ applied to the strips, the electric fields in the x-component were simulated using Comsol, as shown in figure A.5. Compared with the previous case of macroscopic wires, E-field in the similar ranged was created, with a lower electrode potential. A higher E-field gradient in the x-direction was observed, this will not be a problem since the E-field was still fairly uniform within the atomic cloud size of $\sim 50\mu$m.

For compensation of the E-field gradient in x-direction, the case of using different magnitude in electrode potential were considered, with $V_1 = -10V$ and $V_2 = +30V$, shown in figure A.6. Compared with the case of macroscopic wires, strip electrodes are better at compensating the stray E-field gradients, improving the uniformity of the E-field in the x-direction.
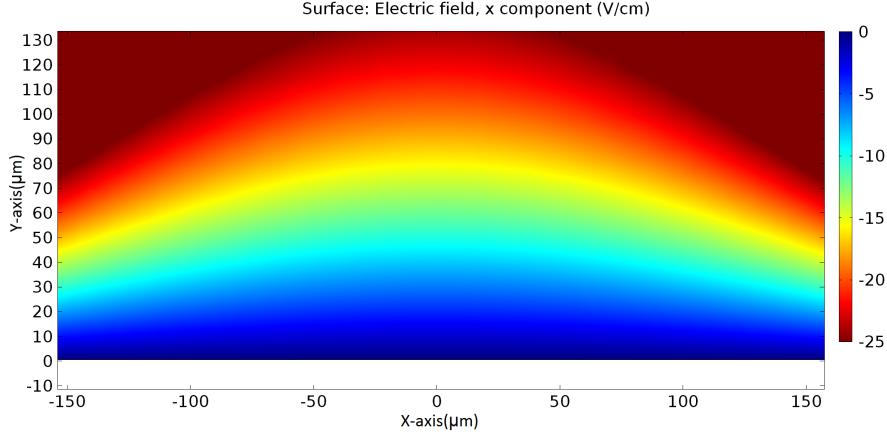
Figure A.5: Simulation of the E-field in x-component with $V_1 = -20V$ and $V_2 = +20V$. Here, similar range of E-fields are created using much smaller and manageable electric potentials. Here, we observe a higher E-gradient in the x-direction. This will not be a problem since E-field within 50μm in the x-direction is still fairly constant.
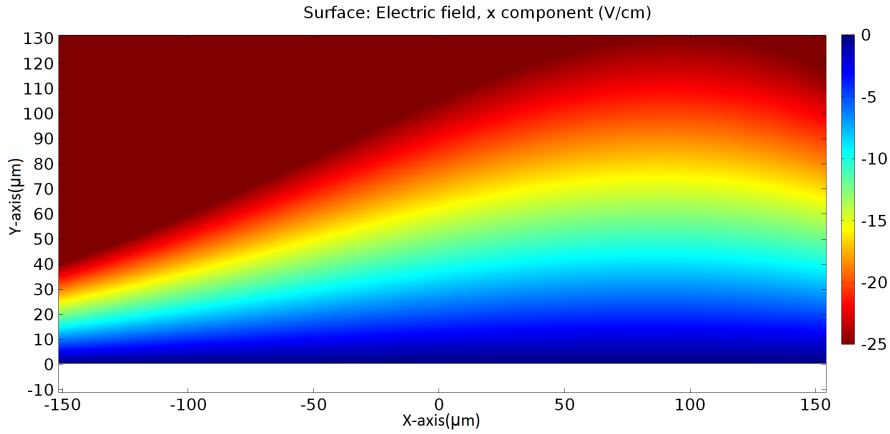
Figure A.6: Simulation of the E-field in x-component with $V_1 = -10V$ and $V_2 = +30V$. Unlike the case of using macroscopic wires in previous section, the E-field gradient in x-direction created is higher. Hence, capable in compensating the stray E-field gradient in the x-direction.

In concluding this section: It is possible to further reduce the stray E-fields by compensating the orthogonal direction. First, this can be done by laying two electrode wires above the current chip. High voltages had to be used in this case, ranging from magnitudes of 100V and above. Second, by modifying the current chip design, additional electrodes can be implemented into the chip. E-field compensation using on-chip electrodes required voltage in the range 10V. This also comes with additional benefits in compensation of E-field gradient on the atom chip's parallel axis. In both cases, the effect of high E-fields close to the vicinity of CPW resonator needs to be further investigated.

67

Appendix B

Towards atom-cavity coupling with higher Rydberg states

With the implementation of E-field compensation in all three axes, it is possible to compensate surrounding E-fields to less than 1V/cm. In this section, we consider the case of Rydberg atom-cavity coupling in E-fields of <1V/cm with the CPW resonator at the 3rd harmonic mode $\omega_{\text{Res}} \sim 20.5\text{GHz}$. Shown in figure B.1.
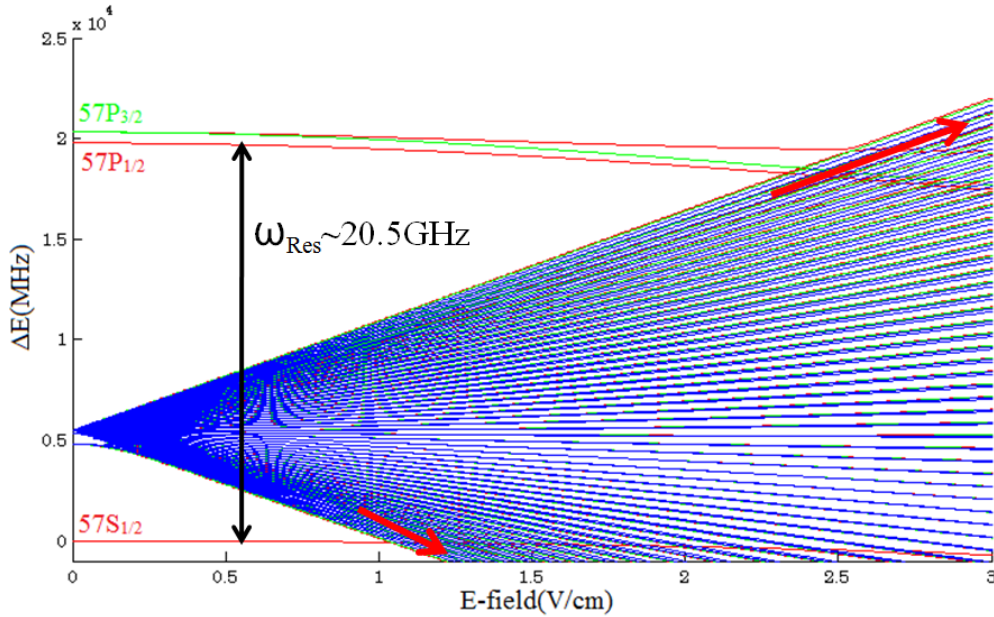
Figure B.1: Stark map of $57S$ and $57P$ Rydberg state. With ambient E-field less than 1V/cm, coupling of $57S_{1/2}$ Rydberg state to a CPW resonator with the 3rd harmonic mode $\omega_{\text{Res}} \sim 20.5\text{GHz}$ will be possible. Since the time evolution of $57S_{1/2}$ and $57P_{3/2}$ states in E-field evolved separately (shown by red arrow), SFI will be an ideal method in detecting both states, without the requirement of a blowing laser[1]. Trapped at $\sim 20\mu$m above the CPW resonator gap, single Rydberg atom-single photon coupling strength of $g \sim 1\text{MHz}$ was estimated.

---

[1]For Selective Field Ionization (SFI) and its limitation, refer back to chapter 4.3

Appendix C

Publication of data in chapter 3

H. Hattermann, D. Bothner, L. Y. Ley, B. Ferdinand, D. Wiedmaier, L. Sárkány,
R. Kleiner, D. Koelle & J. Fortágh
Coupling ultracold atoms to a superconducting coplanar waveguide resonator

Coupling ultracold atoms to a superconducting coplanar waveguide resonator

H. Hattermann[1], D. Bothner[1,2], L.Y. Ley[1], B. Ferdinand[1], D. Wiedmaier[1], L. Sárkány[1], R. Kleiner[1], D. Koelle[1] & J. Fortágh[1]

Ensembles of trapped atoms interacting with on-chip microwave resonators are considered as promising systems for the realization of quantum memories, novel quantum gates, and interfaces between the microwave and optical regime. Here, we demonstrate coupling of magnetically trapped ultracold Rb ground-state atoms to a coherently driven superconducting coplanar resonator on an integrated atom chip. When the cavity is driven off-resonance from the atomic transition, the microwave field strength in the cavity can be measured through observation of the AC shift of the atomic hyperfine transition frequency. When driving the cavity in resonance with the atoms, we observe Rabi oscillations between hyperfine states, demonstrating coherent control of the atomic states through the cavity field. These observations enable the preparation of coherent atomic superposition states, which are required for the implementation of an atomic quantum memory.

[1] CQ Center for Quantum Science in LISA+, Physikalisches Institut, Eberhard Karls Universität Tübingen, Auf der Morgenstelle 14, D-72076 Tübingen, Germany. [2] Present address: Kavli Institute of Nanoscience, Delft University of Technology, PO Box 5046, 2600 GA, Delft, The Netherlands. Correspondence and requests for materials should be addressed to H.H. (email: hattermann@pit.physik.uni-tuebingen.de)

ybrid quantum systems of superconductors and atomic
spin ensembles have been proposed[1-3] for quantum
information processing to overcome the limited
coherence of superconducting qubits[4,5]. In the envisioned hybrid
system, information is processed by fast superconducting circuits
and stored in a cloud of cold atoms, which serves as a quantum
memory[6-8]. Information is transferred between the two quantum
systems using a superconducting coplanar waveguide resonator
as a quantum bus. In recent years, coupling between super-
conducting structures and spin systems such as nitrogen vacancy
centers[9-13] and ions in solid-state systems[14,15] has been observed.
Cold atoms coupled to superconducting resonators would,
furthermore, enable the implementation of novel quantum
gates[16-19], the realization of a microwave-to-optical transdu-
cer[20,21], and on-chip micromasers[22]. The interaction between
Rydberg atoms and three-dimensional superconducting micro-
wave resonators has been a rich research topic, especially with
regard to atom–photon interactions on the fundamental level[23].
Research on planar superconducting structures, however, holds
the promise of switchable interactions between the subsystems,
integration with scalable solid-state circuitry[24-26], and long
information storage times in the atomic ensemble. While long
coherence times in cold atoms have been studied extensively[27-31]
and trapping and manipulation of atoms in the vicinity of
superconducting chips has been demonstrated in a series of
experiments[32-37], coupling between trapped atoms and planar
superconducting resonators has not been shown yet.

In this article, we demonstrate magnetic coupling of ultracold
magnetically trapped atoms to a superconducting coplanar
waveguide resonator operated at temperatures around 6 K. The
cavity is near resonant with the atomic hyperfine splitting of ^{87}Rb
and coherently driven by an external microwave synthesizer. We
investigate both the dispersive and the resonant coupling regime.
By driving the cavity off-resonantly with respect to the atoms, the
atomic states reveal an AC-Zeeman shift under the influence
of the microwave (MW) field[38]. This leads to a shift of the
atomic transition frequency, which is measured by Ramsey
interferometry. We use the AC-Zeeman shift to reconstruct the
microwave intensity in the coplanar resonator. In contrast, when
the cavity is driven at a frequency corresponding to an atomic
transition, Rabi oscillations between atomic hyperfine states are
observed.

Our measurements present a vital step toward the realization of
an atom–superconductor hybrid system, paving the way toward
the implementation of an atomic quantum memory coupled to a
superconducting quantum circuit and the realization of
microwave-to-optical transducers.

Results

Atomic ensembles trapped in a coplanar waveguide resonator.
For our experiments, we magnetically trap an ensemble of
ultracold ^{87}Rb atoms in the state $5S_{1/2}F = 1$, $m_F = -1 := |1, -1\rangle$
close to a coplanar microwave resonator on an integrated atom
chip. The chip comprises two essential structures: i) a Z-shaped
wire for magnetic trapping of neutral atoms and ii) a super-
conducting coplanar waveguide (CPW) resonator (Fig. 1a, b).

The CPW resonator is an inductively coupled half-wavelength
cavity[39] with a fundamental mode resonance frequency of
$\omega_{Res} \approx 2\pi \cdot 6.84$ GHz and a linewidth of $\kappa \approx 2\pi \cdot 3$ MHz corre-
sponding to a quality factor of $Q \approx 2200$ in the temperature range
($T = 6$–7 K) relevant for the experiments described here. By
varying the temperature of the atom chip, the resonance
frequency of the microwave cavity can be tuned by about 30
MHz, where the atomic hyperfine transition frequency $\omega_{HF} = 2\pi$
$\cdot 6.8347$ GHz lies within this tuning range. Details on the chip

design and fabrication methods can be found in Supplementary
Note 1 of this article, and details on the cavity parameters
and their temperature dependence in Supplementary Notes 2
and 3.

With the coupling inductors (Fig. 1c, d), the microwave cavity
gap close to the Z trap provides a closed superconducting loop on
the chip, in which the total magnetic flux is conserved. The other
resonator gap does not form a closed loop, as the lower ground
plane has been cut to avoid flux trapping. We take advantage of
the flux conservation by freezing a well-defined amount of
magnetic flux into the closed loop during the chip cooldown. A
conservative magnetic trapping potential for the Rb atoms in the
vicinity of the cavity mode is formed by the combination of flux-
conserving loop currents and a homogeneous external field[31,40].
A homogeneous offset field along the y-axis $B_{off} = 0.323$ mT is
additionally applied to ensure a nonzero magnetic field amplitude
in the trap minimum to avoid spin-flip losses.

$N_{at} \sim 10^5$ atoms are magnetically trapped at a distance of ~20
μm above one of the CPW gaps and close to one of the ends of
the cavity, where the antinodes of the standing microwave
magnetic fields are located, cf. Fig. 1b, e. At this position, the
magnetic MW field of the transversal wave in the cavity is
oriented perpendicular to the quantization axis of the atomic
spins (y direction). Figure 1f depicts the coupling to the magnetic
MW field of the cavity, obtained from finite-element simulations
(Supplementary Note 4), in a cross-sectional view of the
resonator. Solid white lines indicate the calculated positions of
equal atomic density for an atomic cloud of 800 nK. From the
MW field amplitude at the position of the atoms, we estimate an
average single-atom single-photon coupling strength of
$g = \vec{\mu} \cdot \vec{B}_{ph} \approx 2\pi \cdot 0.5$ Hz. The magnetic MW field and thus the
coupling can be considered constant along the atomic cloud with
an extension of ~100 μm in y direction, which is about two orders
of magnitude smaller than the cavity and thus the wavelength.
For the experiments described in this article, the cavity is driven
by an external microwave synthesizer. In the limit of high photon
numbers $n_{ph} \gg N_{at}$ explored in this article, the cavity field can be
treated classically, and the collective coupling between an atom
and the cavity is small compared to the damping rate. In the
classical regime, the atoms couple individually to the cavity field,
hence, the Rabi frequency is independent of the number of atoms
in the cavity[41].

Sensing the cavity field with cold atoms.
When driving the
resonator at a frequency ω_{dress} off-resonant to the atoms, the
atomic transition is shifted by the MW field. This AC-Zeeman
shift can be experimentally detected and used to reconstruct the
intensity of the cavity field. We measure the frequency of the
atomic transition between the magnetically trapped states $|1, -1\rangle$
and $|2, 1\rangle$ using time-domain Ramsey interferometry. The two
states exhibit the same first-order Zeeman shift, thereby strongly
reducing the sensitivity of the transition frequency to magnetic
fields. For the Ramsey measurements, the atoms are prepared in a
coherent superposition driven by a pulsed MW field ω_{extMW} from
an external antenna and an additional radio frequency of ω_{RF} fed
to the Z-shaped trapping wire (green arrows in Fig. 2a). After a
variable time T_{Ramsey}, a second MW + RF pulse is applied and the
relative population in the two states is measured. The populations
in the two states oscillate with the difference between the atomic
frequency and the external frequency, $\omega_{at} - (\omega_{extMW} + \omega_{RF})$.
During the Ramsey sequence, the CPW cavity is driven by a field
with a variable angular frequency ω_{dress} that is off-resonant to the
atomic transition (Fig. 2b). This leads to an AC shift of the
levels which depends on the detuning Δ between ω_{dress} and
the atomic transition frequency. For a simple two-level system,
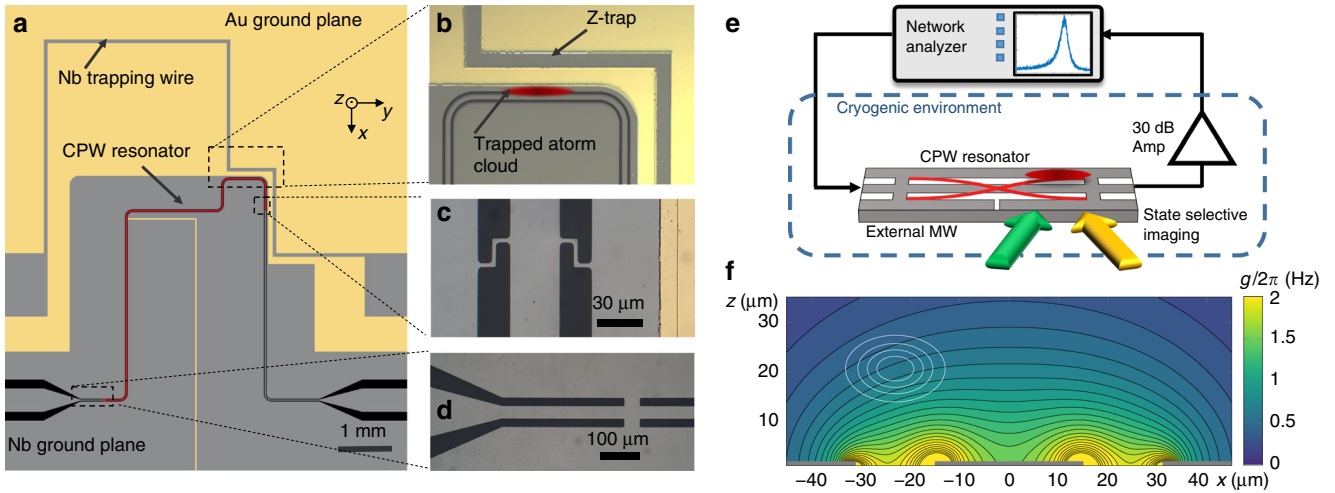
Fig. 1 A superconducting atom chip for coupling ultracold atoms to a coplanar resonator. **a** Schematic top view of the superconducting atom chip, comprising a Z-shaped trapping wire and a coplanar microwave resonator (center conductor marked in red). Parts of the niobium ground planes have been replaced by gold to circumvent the Meissner effect and facilitate magnetic trapping. The slit in the lower ground plane prevents the formation of a closed superconducting loop. **b** Optical microscope image of the trapping region with the position of the atoms trapped close to the antinode of the resonator. During the measurements, trapping is purely provided by persistent supercurrents around the upper cavity gap and external fields. **c** Microscope image of the coupling inductances at the output of the resonator and **d** at the input of the resonator. **e** Scheme of the measurement setup. Atoms are coupled to a driven coplanar waveguide resonator and detected by state-selective absorption imaging. For Ramsey experiments in the dispersive regime, additional external microwave fields are used to manipulate the atoms. **f** Simulated coupling strength $g/2\pi$ (Hz) between a single ground-state atom and a single photon in the cavity, resonant to the $|1, -1\rangle \rightarrow |2, 0\rangle$ transition. The white lines indicate positions of equal density for an atomic cloud of temperature $T_{at} = 800$ nK in the trap, corresponding to 20, 40, 60, and 80% of the density in the center
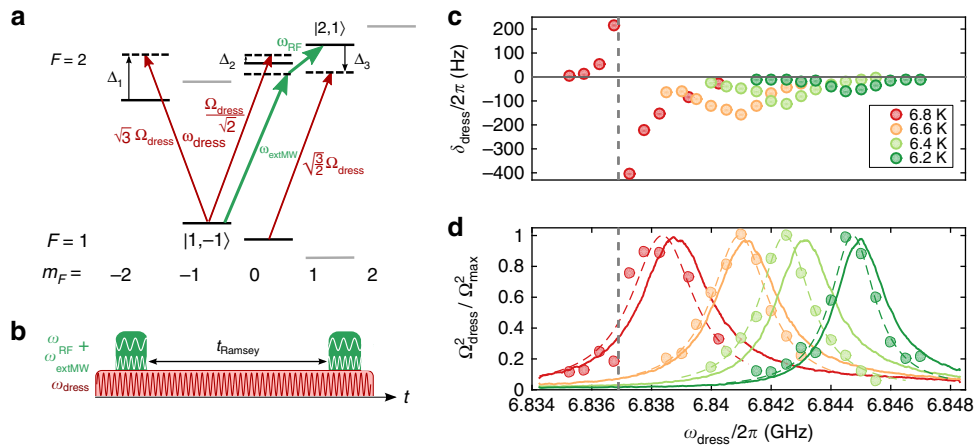
Fig. 2 Probing the off-resonant cavity field with cold atoms. **a** Level scheme of the ^{87}Rb ground-state manifold. The external MW and RF frequencies used for driving the two-photon transitions for the Ramsey scheme (green) and the off-resonant coupling of the cavity field to the relevant states are shown (red). **b** Experimental timing for the Ramsey sequence. The cavity field (red) is driven throughout the interferometric sequence. **c** Measured shift of the Ramsey frequency vs. frequency of the field in the superconducting microwave resonator for different chip temperatures. The sign change in the 6.8 K curve occurs at crossing the $|1, 0\rangle \rightarrow |2, 1\rangle$ transition, i.e., when $\Delta_3 = 0$, as indicated by dashed vertical line. **d** Data points: Calculated microwave intensity Ω^2_{dress} based on the measurements of δ_{dress}. The colored dashed lines are Lorentzian fits to the data points. The solid lines are the measured transmission spectra of the microwave resonator

the off-resonant field shifts the atomic states by $\delta_{\text{dress}} = \pm \frac{\Omega^2_{\text{dress}}}{\Delta}$, where Ω_{dress} denotes the Rabi frequency of the dressing field and $\Delta = \omega_{\text{dress}} - \omega_0$ is the detuning between the dressing field and the atomic transition frequency. The plus (minus) sign is valid for the ground (excited) state. The level scheme of the atoms involving all relevant fields is depicted in Fig. 2a. For a MW field which is linearly polarized perpendicular to the quantization axis, as it is in our case, the cavity field induces σ^- and σ^+-transitions with equal field strength, as depicted by the red arrows. This field hence couples the state $|1, -1\rangle$ to the states $|2, -2\rangle$ and $|2, 0\rangle$. The

state $|2, 1\rangle$, on the other hand, is coupled to state $|1, 0\rangle$. This leads to a shift in the two-photon transition frequency $|1, -1\rangle \rightarrow |2, 1\rangle$ by

$$\delta_{\text{dress}} = -\Omega^2_{\text{dress}} \cdot \left(\frac{3}{\Delta_1} + \frac{1/2}{\Delta_2} + \frac{3/2}{\Delta_3} \right), \quad (1)$$

which is measured in our experiment (Supplementary Note 5 for details). Here, $\Delta_i, i \in \{1, 2, 3\}$ denotes the detuning to the relevant atomic hyperfine transition. The numerical factors in the

numerator are determined by the Clebsch–Gordan coefficients of the transitions.

For the measurement, the power of the microwave fed to the resonator and the magnetic offset field ($B_{off} = 0.315 \pm 0.003$ mT) is held constant.

The measured frequency shift δ_{dress} in the Ramsey experiment is shown in Fig. 2c. As visible in the curve measured at $T = 6.8$ K, the dressing shift changes sign when the frequency of the dressing field is crossing an atomic resonance. Variation of the dressing frequency affects the shift in two ways, via the detuning to the atomic transitions and via a change in the microwave intensity in the resonator. Knowing the detuning to all involved levels, the normalized power of the microwave in the resonator, which is proportional to the square of the resonant Rabi frequency Ω_{dress}^2, can be deduced from the dressing shift. The calculated Rabi frequencies Ω_{dress} according to Eq. (1) are shown as circles in Fig. 2d. The measurement was repeated for different temperatures of the superconducting chip, corresponding to different cavity resonance frequencies. The result is compared with transmission spectra measured using a programmable network analyzer (solid lines in Fig. 2d). All curves are normalized to their maxima for the sake of comparability. Lorentzian curves (dashed lines) fitted to the data points match the transmission spectra closely in center frequency and peak width, which is on the order of $\kappa/2\pi \approx 2 - 3$ MHz. We note that there is a slight systematic offset between the reconstructed Rabi frequencies and the transmission curves. Possible explanations are trapping of Abrikosov vortices during the Ramsey measurement due to cycling of applied magnetic fields, which are known to shift the resonator frequency to lower values, or a small temperature difference (<50 mK) between the two measurements.

Coherent control of atomic states with cavity fields. When the electromagnetic cavity field is resonant with one of the (allowed) atomic transitions, the atoms undergo coherent Rabi oscillations between the ground and excited state (Fig. 3a). The observation of these oscillations demonstrates coherent control over the internal atomic degrees of freedom. The Rabi frequency is given by $\Omega_0 = \vec{\mu} \cdot \vec{B}_{MW}$, where $\vec{\mu}$ is the atomic magnetic moment and $\vec{B}_{MW}$ is the amplitude of the oscillating magnetic MW field. For the observation of these oscillations, we drive the cavity with a frequency of $\omega_0 = 2\pi \cdot 6.83242$ GHz, which is in resonance with the atomic transition $|1, -1\rangle \rightarrow |2, 0\rangle$, but detuned roughly by twice the cavity linewidth κ from the cavity resonance ($\omega_{cav} \approx 2\pi \cdot 6.839$ GHz) at a chip temperature $T = 6.9$ K (Fig. 3b, c). By state-selective absorption imaging of the atoms, we observe resonant Rabi oscillations between the states $|1, -1\rangle$ and $|2, 0\rangle$ with a Rabi frequency $\Omega_0 \approx 2\pi \cdot 20$ kHz. By variation of the chip temperature between $T = 6.7$ and 7.0 K, the cavity frequency is shifted with respect to the atomic transition (Fig. 3d). This leads to a measurable change in the resonant Rabi frequency due to the altered MW power in the cavity, as visible in Fig. 3e. Here, the Rabi frequency increases with higher temperatures, as the cavity frequency approaches the atomic transition frequency. For temperatures around $T = 7.2$ K, the cavity resonance is shifted to coincide with the atomic resonance. However, at this temperature, the critical current of the superconducting coupling inductances is too low to support a stable magnetic trap.

We observe a damping in the single-photon Rabi oscillations with a time constant of $\tau \approx 50$ μs. This damping is a result of the dephasing due to the inhomogeneous MW field of the cavity and the fact that Rabi oscillations are driven between two states with different magnetic moments. The magnetically trapped state $|1, -1\rangle$ is subjected to an energy shift of $\sim 2\pi\hbar \cdot 7$ MHz/mT, while
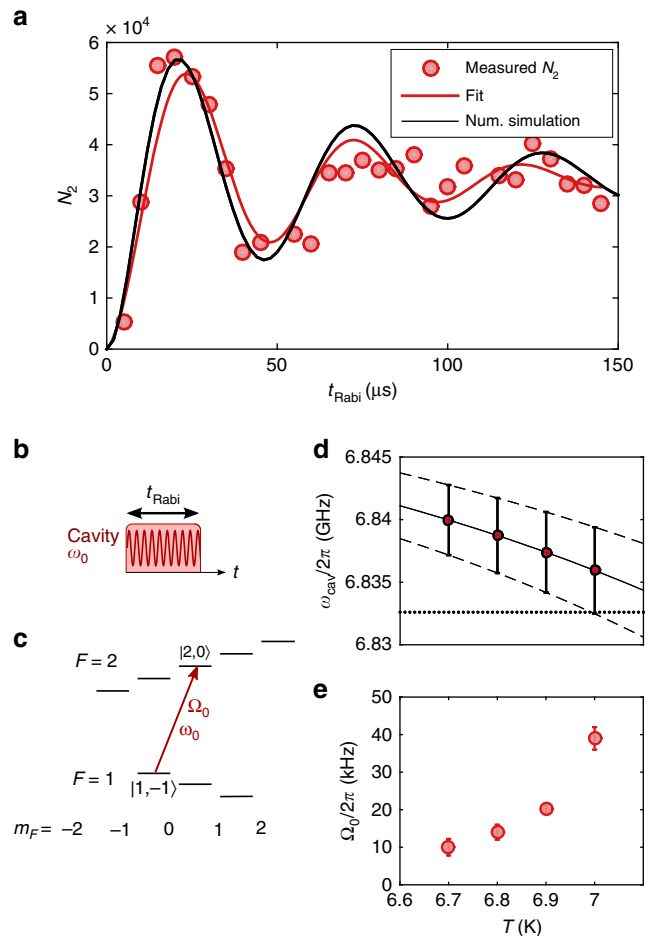
Fig. 3 Cavity-driven Rabi oscillations. **a** Measurement of the atoms in state $|2, 0\rangle$ reveals resonant Rabi oscillations between $|1, -1\rangle$ and $|2, 0\rangle$ for a cavity-driving frequency of $\omega_0 = 2\pi \cdot 6.83242$ GHz. The chip temperature was set to $T = 6.9$ K. The red solid line is a fit to the damped oscillation, and the black line shows the result of the numerical simulations. **b** Timing sequence and **c** level scheme for the driven one-photon Rabi oscillations. **d** Temperature dependence of the cavity resonance frequency. The circles and error bars indicate the peak and the width ($\pm\kappa$) of the cavity line obtained from fits to the resonator transmission data. The solid and dashed lines indicate the fitted temperature dependence of the cavity frequency and linewidth (Supplementary Note 3 for details). The horizontal dotted line indicates the driving frequency, corresponding to the atomic resonance. **e** Temperature dependence of the Rabi frequency. While the cavity is driven at the same frequency ω_0 for all measurements, the temperature dependence of the cavity resonance leads to a change in the microwave intensity. Error bars indicate the confidence interval of the Rabi frequency measurement

the untrapped state $|2, 0\rangle$ is in first order insensitive to magnetic fields. As a consequence, the resonance frequency between the two states is not uniform across the cloud, and the atoms are only exactly on resonance at the center of the trap. A numerical simulation of a thermal cloud at $T_{at} = 2$ μK trapped in a harmonic magnetic potential 20 μm above the cavity gap shows a damping time in excellent agreement with our measurement. We can estimate the number of photons in the resonator using the measured Rabi frequency and the simulated coupling strength per photon. Assuming a Rabi frequency of 20 kHz, we estimate the number of photons in the cavity $n_{Ph} \approx 1.6 \times 10^9$, so that the thermal occupation of the cavity ($n_{th} \sim 20$) is negligible.
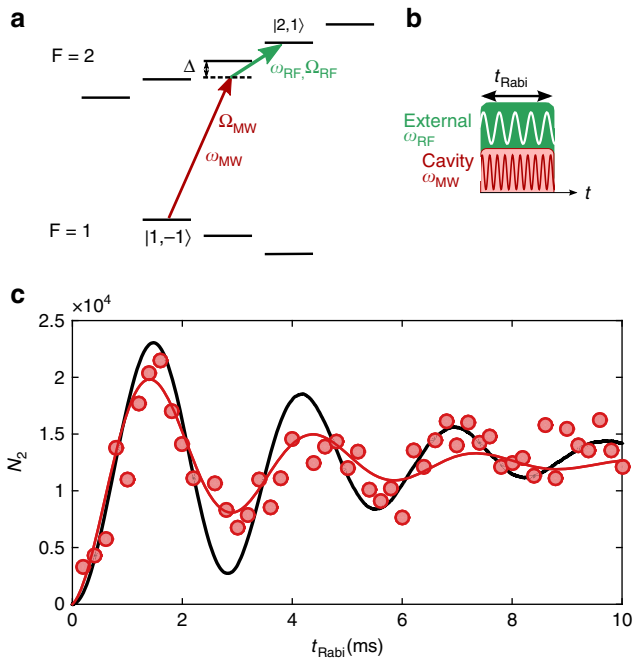
Fig. 4 Two-photon Rabi oscillations. **a** Level scheme and **b** timing sequence for the two-photon Rabi oscillations between the trapped states $|1, -1\rangle$ and $|2, 1\rangle$. **c** Observation of two-photon Rabi oscillations between states $|1, -1\rangle$ and $|2, 1\rangle$ (circles), and fit of the damped oscillation (red), yielding a damping time of $\tau = 5$ ms due to the inhomogeneity of the MW field amplitude across the cloud. The black solid line shows a numerical simulation of the state evolution for an ensemble of thermal atoms moving in the trap

In order to exploit the long coherence times of cold atoms, it is necessary to create superpositions between appropriate atomic states, which can both be trapped in the cavity. For ^{87}Rb, such a state combination consists of the hyperfine levels $|1, -1\rangle$ and $|2, 1\rangle$, which can both be trapped magnetically and exhibit excellent coherence properties. To this end, we start with an atomic cloud at a lower temperature of $T_{at} = 800$ nK and $N_{at} \sim 3 \times 10^4$ atoms in the state $|1, -1\rangle$. In order to prepare a coherent superposition of the two states, we drive the cavity with the MW field ω_{MW} and employ an additional external RF field ω_{RF}, with a detuning of $\Delta = 2\pi \cdot 300$ kHz to the intermediate state $|2, 0\rangle$ (cf. Fig. 4a). If the two corresponding Rabi frequencies are small compared to the intermediate detuning, i.e., $\Omega_{MW}, \Omega_{RF} \ll \Delta$, the population of the intermediate state can be neglected. In this case, the two-photon Rabi frequency Ω_{2Ph} can be calculated by adiabatic elimination of the intermediate state $\Omega_{2Ph} = \Omega_{MW}\Omega_{RF}/2\Delta$[42]. By driving the two fields with variable pulse lengths (Fig. 4b), we observe Rabi oscillations with $\Omega_{2Ph} = 2\pi \cdot 340$ Hz, and a dephasing on the order of $\tau \sim 5$ ms (Fig. 4c). A numerical simulation of an ensemble of noninteracting atoms in a magnetic trap reveals damping on the same timescale. As in the one-photon case, the dephasing is mainly due to the variation of the microwave field strength over the size of the atomic cloud (Supplementary Note 6).

Discussion

To make the presented cold atom–superconductor hybrid device a useful high-coherence quantum resource, several aspects need to be addressed and optimized. In particular, dephasing during the Rabi pulses should be reduced and the coupling between atoms and the cavity increased.

Dephasing due to inhomogeneous coupling, as seen in the experiment above, can be a limitation for the high-fidelity creation of superposition states needed in information processing. The inhomogeneity seen by the atomic ensemble can be reduced by reducing the cloud temperature, yielding smaller cloud extension in the trap (Supplementary Note 6). Several experiments have furthermore shown that reliable superpositions or quantum gates can be achieved in spite of this temporal or spatial variation of Rabi frequencies, as the related dephasing can be overcome using more elaborate MW and RF pulses using optimal control theory[43,44].

Furthermore, future experiments should be performed at chip temperatures in the mK regime to reduce the number of thermal photons, so, different ways to tune the cavity frequency need to be employed. Tuning the cavity could be achieved by various means, such as using nonlinear kinetic inductances[45], SQUIDs[46,47], or mechanical elements, as demonstrated in ref. [48].

For our geometry, we have estimated the coupling between a single atom and a single cavity photon to be $g \approx 2\pi \cdot 0.5$ Hz. Various means can be used to increase the coupling strength between the atoms and the cavity field. By decreasing the width of the gap W between the center conductor and ground planes of the cavity, the magnetic field per photon could be increased according to $B_{ph} \propto 1/W^2$, but would require the atoms to be trapped closer to the chip surface. By changing the resonator layout from CPW to lumped element resonator, the inductance and dimensions of the resonator could be decreased, leading to a significant enhancement of the current per photon and hence magnetic field B_{ph}. Finally, the electric field of the cavity mode could be used to couple neighboring Rydberg states, exploiting the large electric dipole moments of Rydberg states[49]. A similar experiment has been demonstrated with flying Rydberg atoms above a CPW transmission line[50]. For our geometry, the transition between the states $57S_{1/2}$ and $57P_{3/2}$ lies close to the third harmonic of our resonator. The dipole matrix element of this transition is $d \sim 2700$ ea_0, yielding a single-photon single-atom coupling strength of $g/2\pi \approx 0.1$ MHz.

In summary, we have experimentally demonstrated coupling of ultracold ground-state atoms to a driven superconducting CPW resonator. Coupling was shown both in resonant Rabi oscillation and in dressing the frequency of an atomic clock state pair. Future measurements will explore collective effects of cold atoms to the cavity mode and work toward strong coupling between the superconducting resonator and Rydberg atoms. These experiments are the first step toward the implementation of cold atoms as a quantum resource in a hybrid quantum architecture.

Methods

Atomic cloud preparation. The atomic ensemble is prepared in a room-temperature setup and transported to a position below the superconducting atom chip using an optical dipole trap that is moved using a lens mounted on an air-bearing translation stage (cf. ref. [51] for details). Atoms are subsequently trapped in a magnetic trap generated by currents in the Z-shaped Nb wire and an external homogeneous bias field. The Z-wire configuration leads to a Ioffe-Pritchard- type magnetic microtrap with a nonzero offset field B_{off} at the trap minimum. We load ~10^6 atoms at a temperature of ~1 μK into the magnetic chip trap. After adiabatic compression, the cloud is transferred into the mode volume of the resonator by rotating the external bias field and switching off the current in the Z trap. Screening currents in the resonator, which conserve the flux in the closed superconducting loop, lead to the formation of a magnetic trap with oscillation frequencies $\omega_x = 2\pi \cdot 400$ s^{-1}, $\omega_y = 2\pi \cdot 25$ s^{-1}, and $\omega_z = 2\pi \cdot 600$ s^{-1} below the gap of the waveguide cavity, 20 μm from the chip surface. During the transfer into the tight trap, the atomic cloud is heated up to a temperature of $T_{at} \approx 2$ μK. At the cavity position, we perform radiofrequency evaporation to further cool the atomic ensemble.

Experimental cycle and state-selective detection. In order to measure the atomic state, the following experimental cycle is repeated every ~26 s. After preparation of an atomic cloud, transporting it to the superconducting chip, and loading into the cavity, as described above, all atoms are in the hyperfine state $|1, -1\rangle$. Subsequently, we apply one MW (+RF) pulse of variable length t_{Rabi} for the measurement of Rabi oscillations, or two $\pi/2$-pulses of fixed length with a variable hold time t_{Ramsey} in-between for the Ramsey interferometry sequence. At the end of the sequence, we can measure the number of atoms in both of the states. First, the number of atoms in $F = 2$ is measured by illuminating the cloud with light resonant to the $5S_{1/2}, F = 2 \rightarrow 5P_{3/2}$, and $F = 3$ transition. The shadow of the atoms is imaged on a CCD camera and the measured optical density is used to determine the atom number. We then pump the atoms from $F = 1$ into $F = 2$ by illumination with a laser resonant to the $5S_{1/2}, F = 1 \rightarrow 5P_{3/2}$, and $F = 2$ transition. From the $5P_{3/2}, F = 2$ state, the atoms decay into $5P_{1/2}, F = 2$ in ~30 ns, and the atoms are imaged on a second CCD camera as described above.

References

1. Xiang, Z.-L., Ashhab, S., You, J. Q. & Nori, F. Hybrid quantum circuits: Superconducting circuits interacting with other quantum systems. *Rev. Mod. Phys.* **85**, 623–653 (2013).
2. André, A. et al. A coherent all-electrical interface between polar molecules and mesoscopic superconducting resonators. *Nat. Phys.* **2**, 636–642 (2006).
3. Henschel, K., Majer, J., Schmiedmayer, J. & Ritsch, H. Cavity QED with an ultracold ensemble on a chip: Prospects for strong magnetic coupling at finite temperatures. *Phys. Rev. A* **82**, 033810 (2010).
4. Kim, Z. et al. Decoupling a Cooper-pair box to enhance the lifetime to 0.2 ms. *Phys. Rev. Lett.* **106**, 120501 (2011).
5. Paik, H. et al. Observation of high coherence in Josephson junction qubits measured in a three-dimensional circuit QED architecture. *Phys. Rev. Lett.* **107**, 240501 (2011).
6. Verdú, J. et al. Strong magnetic coupling of an ultracold gas to a superconducting waveguide cavity. *Phys. Rev. Lett.* **103**, 043603 (2009).
7. Patton, K. R. & Fischer, U. R. Hybrid of superconducting quantum interference device and atomic Bose–Einstein condensate: an architecture for quantum information processing. *Phys. Rev. A* **87**, 052303 (2013).
8. Patton, K. R. & Fischer, U. R. Ultrafast quantum random access memory utilizing single Rydberg atoms in a Bose–Einstein condensate. *Phys. Rev. Lett.* **111**, 240504 (2013).
9. Kubo, Y. et al. Strong coupling of a spin ensemble to a superconducting resonator. *Phys. Rev. Lett.* **105**, 140502 (2010).
10. Kubo, Y. et al. Hybrid quantum circuit with a superconducting qubit coupled to a spin ensemble. *Phys. Rev. Lett.* **107**, 220501 (2011).
11. Amsüss, R. et al. Cavity QED with magnetically coupled collective spin states. *Phys. Rev. Lett.* **107**, 060502 (2011).
12. Putz, S. et al. Protecting a spin ensemble against decoherence in the strong-coupling regime of cavity QED. *Nat. Phys.* **10**, 720–724 (2014).
13. Grezes, C. et al. Towards a spin-ensemble quantum memory for superconducting qubits. *Comptes Rendus Phys.* **17**, 693–704 (2016).
14. Schuster, D. I. et al. High-cooperativity coupling of electron-spin ensembles to superconducting cavities. *Phys. Rev. Lett.* **105**, 140501 (2010).
15. Probst, S. et al. Anisotropic rare-earth spin ensemble strongly coupled to a superconducting resonator. *Phys. Rev. Lett.* **110**, 157001 (2013).
16. Petrosyan, D. et al. Reversible state transfer between superconducting qubits and atomic ensembles. *Phys. Rev. A* **79**, 040304 (2009).
17. Petrosyan, D. & Fleischhauer, M. Quantum information processing with single photons and atomic ensembles in microwave coplanar waveguide resonators. *Phys. Rev. Lett.* **100**, 170501 (2008).
18. Pritchard, J. D., Isaacs, J. A., Beck, M. A., McDermott, R. & Saffman, M. Hybrid atom-photon quantum gate in a superconducting microwave resonator. *Phys. Rev. A* **89**, 010301 (2014).
19. Sárkány, L., Fortágh, J. & Petrosyan, D. Long-range quantum gate via Rydberg states of atoms in a thermal microwave cavity. *Phys. Rev. A* **92**, 030303 (2015).
20. Hafezi, M. et al. Atomic interface between microwave and optical photons. *Phys. Rev. A* **85**, 020302 (2012).
21. Gard, B. T., Jacobs, K., McDermott, R. & Saffman, M. Microwave-to-optical frequency conversion using a cesium atom coupled to a superconducting resonator. *Phys. Rev. A* **96**, 013833 (2017).
22. Yu, D., Kwek, L. C., Amico, L. & Dumke, R. Theoretical description of a micromaser in the ultrastrong-coupling regime. *Phys. Rev. A* **95**, 053811 (2017).
23. Haroche, S. & Raimond, J. *Exploring the Quantum: Atoms, Cavities, and Photons*. (Oxford Univ. Press, Oxford, 2006).
24. Wallraff, A. et al. Strong coupling of a single photon to a superconducting qubit using circuit quantum electrodynamics. *Nature* **431**, 162–167 (2004).
25. DiCarlo, L. et al. Preparation and measurement of three-qubit entanglement in a superconducting circuit. *Nature* **467**, 574–578 (2010).
26. Lucero, E. et al. Computing prime factors with a Josephson phase qubit quantum processor. *Nat. Phys.* **8**, 719–723 (2012).
27. Treutlein, P., Hommelhoff, P., Steinmetz, T., Hänsch, T. W. & Reichel, J. Coherence in microchip traps. *Phys. Rev. Lett.* **92**, 203005 (2004).
28. Deutsch, C. et al. Spin self-rephasing and very long coherence times in a trapped atomic ensemble. *Phys. Rev. Lett.* **105**, 020401 (2010).
29. Kleine Büning, G. et al. Extended coherence time on the clock transition of optically trapped rubidium. *Phys. Rev. Lett.* **106**, 240801 (2011).
30. Dudin, Y. O., Li, L. & Kuzmich, A. Light storage on the time scale of a minute. *Phys. Rev. A* **87**, 031801 (2013).
31. Bernon, S. et al. Manipulation and coherence of ultra-cold atoms on a superconducting atom chip. *Nat. Commun.* **4**, 2380 (2013).
32. Nirrengarten, T. et al. Realization of a superconducting atom chip. *Phys. Rev. Lett.* **97**, 200405 (2006).
33. Mukai, T. et al. Persistent supercurrent atom chip. *Phys. Rev. Lett.* **98**, 260407 (2007).
34. Roux, C. et al. Bose–Einstein condensation on a superconducting atom chip. *Europhys. Lett.* **81**, 56004 (2008).
35. Minniberger, S. et al. Magnetic conveyor belt transport of ultracold atoms to a superconducting atomchip. *Appl. Phys. B* **116**, 1017–1021 (2014).
36. Müller, T. et al. Programmable trap geometries with superconducting atom chips. *Phys. Rev. A* **81**, 053624 (2010).
37. Weiss, P. et al. Sensitivity of ultracold atoms to quantized flux in a superconducting ring. *Phys. Rev. Lett.* **114**, 113003 (2015).
38. Sárkány, L., Weiss, P., Hattermann, H. & Fortágh, J. Controlling the magnetic-field sensitivity of atomic-clock states by microwave dressing. *Phys. Rev. A* **90**, 053416 (2014).
39. Bothner, D., Wiedmaier, D., Ferdinand, B., Kleiner, R. & Koelle, D. Improving superconducting resonators in magnetic fields by reduced field-focussing and engineered flux screening. *Phys. Rev. Appl.* **8**, 034025 (2017).
40. Bothner, D. et al. Inductively coupled superconducting half wavelength resonators as persistent current traps for ultracold atoms. *New J. Phys.* **15**, 093024 (2013).
41. Chiorescu, I., Groll, N., Bertaina, S., Mori, T. & Miyashita, S. Magnetic strong coupling in a spin-photon system and transition to classical regime. *Phys. Rev. B* **82**, 024413 (2010).
42. Gentile, T. R., Hughey, B. J., Kleppner, D. & Ducas, T. W. Experimental study of one- and two-photon Rabi oscillations. *Phys. Rev. A* **40**, 5103–5115 (1989).
43. Schulte-Herbrüggen, T., Spörl, A., Khaneja, N. & Glaser, S. J. Optimal control for generating quantum gates in open dissipative systems. *J. Phys. B: At. Mol. Opt. Phys.* **44**, 154013 (2011).
44. Dolde, F. et al. High-fidelity spin entanglement using optimal control. *Nat. Commun.* **5**, 3371 (2014).
45. Vissers, M. R. et al. Frequency-tunable superconducting resonators via nonlinear kinetic inductance. *Appl. Phys. Lett.* **107**, 062601 (2015).
46. Palacios-Laloy, A. et al. Tunable resonators for quantum circuits. *J. Low. Temp. Phys.* **151**, 1034–1042 (2008).
47. Sandberg, M. et al. Tuning the field in a microwave resonator faster than the photon lifetime. *Appl. Phys. Lett.* **92**, 203501 (2008).
48. Kim, Z. et al. Thin-film superconducting resonator tunable to the ground-state hyperfine splitting of 87rb. *AIP Adv.* **1**, 042107 (2011).
49. Yu, D. et al. Charge-qubit21atom hybrid. *Phys. Rev. A* **93**, 042329 (2016).
50. Hogan, S. D et al.Driving rydberg-rydberg transitions from a coplanar microwave waveguide. *Phys. Rev. Lett.* **108**, 063004 (2012).
51. Cano, D. et al. Experimental system for research on ultracold atomic gases near superconducting microstructures. *Eur. Phys. J. D.* **63**, 17–23 (2011).

Author contributions

D.K., R.K., J.F., and H.H. designed and mounted the experiment. D.B., D.W., B.F., and H. H. developed and fabricated the superconducting chip. H.H. and L.Y.L. carried out the experiments. H.H., D.B., L.Y.L., and B.F. analyzed the data. H.H., D.B., and B.F. performed the numerical simulations. L.S. provided the microwave dressing theory. D.K.,

SUPPLEMENTARY NOTE 1. ATOM CHIP DESIGN AND FABRICATION

Our atom chip combines two structures, a $Y = 100\,\mu$m wide Z-shaped superconducting Nb strip for the application of directed and low frequency currents as well as a superconducting coplanar waveguide resonator with a resonance frequency of $\omega_{\mathrm{Res}} \approx 2\pi \cdot 6.85\,$GHz, near-resonant with the ground state hyperfine transition frequency of ^{87}Rb atoms. All structures are patterned onto a $h_{\mathrm{S}} = 330\,\mu$m thick sapphire substrate by means of optical lithography, thin film deposition and microfabrication . A schematic of the atom trapping region on the chip is shown in Supplementary Figure 1a and a cross-sectional view along the dotted line in 1a is shown in 1b. The full chip layout is shown in Fig. 1a of the main paper.

The coplanar microwave resonator has a centre conductor width of $S = 30\,\mu$m and two ground planes, which are separated from the centre conductor by a gap of $W = 16\,\mu$m, targeting a characteristic impedance $Z_0 = 50\,\Omega$. In order to facilitate the magnetic trapping of atoms closely above the gaps of the waveguide structure, the magnetic field distorting superconducting ground planes had to be removed partially. As we observe strong parasitic resonances when parts of the ground planes are missing (probably due to a parasitic mutual inductance between the trapping wire and the waveguide structure and due to the excitation of chip resonances), we substituted the removed superconducting parts by a normal-conducting Au metallization layer, restoring a good ground connection along the whole resonator. Thus, the trapping wire is embedded into one of the ground planes and galvanically connected to all metallization parts on the chip. As superconductor we use niobium, and as normal conductor we use gold on top of a thin adhesion layer of titanium. The thicknesses of the three films are $h_{\mathrm{Nb}} = 500\,$nm, $h_{\mathrm{Au}} = 400\,$nm, and $h_{\mathrm{Ti}} = 4\,$nm, cf. Supplementary Figure 1b. Between the superconducting parts and the normal-conducting parts, there is a $O = 10\,\mu$m wide overlap region, ensuring a low contact resistance.

In order to minimize additional microwave losses induced by the presence of the normal conductor, we only replaced the superconductor by gold in the trapping region ($\sim 15\%$ of the total resonator length) and kept also a $G = 50\,\mu$m part of the ground plane in this region superconducting. The normal conducting region in between this remaining superconducting part of the ground plane and the superconducting trapping wire is $D + 2O = 120\,\mu$m wide, cf. Supplementary Figure 1b.
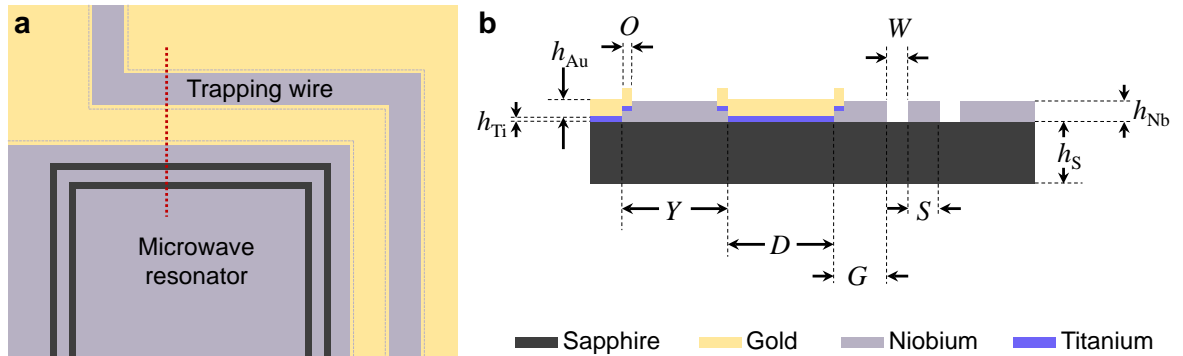
Supplementary Figure 1: **Atom chip layout and parameters. a** Schematic top view of the trapping region of the atom chip. A Z-shaped atom trapping wire passes by a coplanar microwave resonator structure. The trapping wire and the core region of the microwave resonator consist of superconducting Nb, the two structures are galvanically connected by a normal conducting gold layer in order to guarantee well-defined microwave properties. **b** Cross section along the red dotted line in 1a, depicting and defining all relevant materials, thicknesses and geometrical parameters of the device. Resonator centre conductor width $S = 30\,\mu$m, gap size $W = 16\,\mu$m, width of the superconducting ground plane $G = 50\,\mu$m. The Z-wire is $Y = 100\,\mu$m wide, the normal conducting region between resonator and Z-wire is $D = 100\,\mu$m wide. The thicknesses of the three films are $h_{\mathrm{Nb}} = 500\,$nm, $h_{\mathrm{Au}} = 400\,$nm, and $h_{\mathrm{Ti}} = 4\,$nm. Between the superconducting parts and the normal-conducting parts, there is a $O = 10\,\mu$m wide overlap. The chip substrate is $h_{\mathrm{S}} = 330\,\mu$m thick. Thicknesses are not to scale.

The device fabrication is schematically shown in Supplementary Figure 2. It starts with the DC magnetron sputtering of the Nb onto a bare r-cut Sapphire substrate. By means of optical lithography and SF_6 reactive ion etching, we pattern the superconducting parts. Next, we cover most of the superconducting parts – except for the $10\,\mu$m wide overlap region – with photoresist and deposit the normal conducting metal on top. To do so, we first remove 200 nm of the Nb in the overlap region by another SF_6 reactive ion etching step in order to get rid of photoresist residues and a possible native oxide layer on top of the Nb and in addition to reduce the substrate-Nb step height. Then, we in-situ deposited the Ti adhesion layer by means of electron beam evaporation and the Au layer by DC magnetron sputtering. We finalized the fabrication by lifting off the normal conducting parts in hot acetone supported by ultrasound.
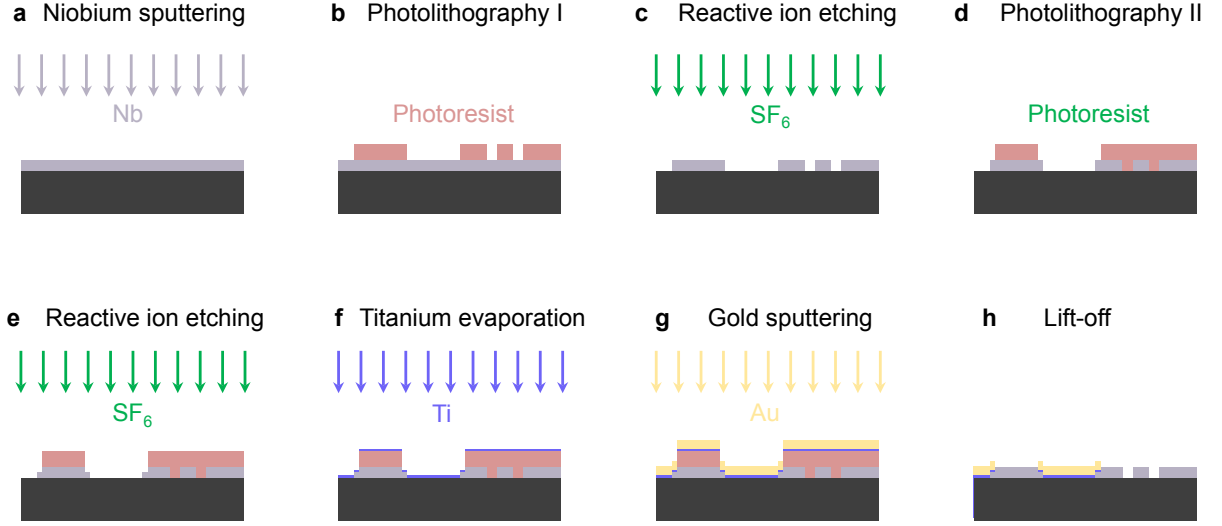
Supplementary Figure 2: **Atom chip fabrication**. Schematic fabrication sequence of the chip used in this experiment. Thicknesses are not to scale. **a** DC magnetron sputtering of Nb onto a Sapphire substrate. **b** Photolithopgraphy and **c** reactive ion etching defining the superconducting chip parts. **d** Protection of the superconducting parts with photoresist, except for a $O = 10\,\mu$m wide overlap edge region. **e** Removal of the native oxide in the overlap region and reduction of the substrate-Nb step height by reactive ion etching. **f** Electron beam evaporation of a titanium adhesion layer. **g** DC magnetron sputtering of Au. Steps **e-g** are performed in-situ. **h** Ultrasound assisted lift-off of Au/Ti in warm acetone.

SUPPLEMENTARY NOTE 2. CAVITY PARAMETERS

The microwave resonator used in this experiment is a half wavelength ($\lambda/2$) transmission line cavity based on a coplanar waveguide with charactersitic impedance $Z_0 \approx 50\,\Omega$ and attenuation constant α. The transmission line cavity has a length $l_0 \approx 9.3\,$mm and a fundamental mode resonance frequency $\omega_{\rm Res} = 2\pi \cdot 6.85\,$GHz at a temperature of $\sim 5\,$K. Around its resonance frequency, the waveguide resonator can be modelled as an inductively coupled series RLC circuit, cf. Supplementary Figure 3a and 3b with the equivalent lumped element resistance R, inductance L and capacity R [1]:

$$R = Z_0 \alpha l_0, \qquad L = \frac{\pi Z_0}{2\tilde{\omega}_{\rm Res}}, \qquad C = \frac{2}{\pi \tilde{\omega}_{\rm Res} Z_0} \tag{1}$$

where α is the attenuation constant of the coplanar waveguide and $\tilde{\omega}_{\rm Res}$ is the "uncoupled" resonance frequency, i.e., the resonance frequency corresponding only to the electrical length of the cavity.

For driving the resonator and reading out its frequency dependent response, the cavity is weakly coupled to two feedlines by shunt inductors between the centre conductor and the ground planes at both ends, cf. Fig. 1 of the main paper. The shunt inductors at the input port are shown in Supplementary Figure 3c. Each of the two superconducting shunts to ground is $36\,\mu$m wide and $16\,\mu$m long. With the software package 3D-MLSI [2], we determined each of the two shunt inductances to be $L_1 = 2.94\,$pH, giving a total input port coupling inductance $L_{\rm in} = L_1/2 = 1.47\,$pH.

At the output port, cf. Supplementary Figure 3e, the shunt inductors are $4\,\mu$m wide and $30\,\mu$m long, giving an inductance per shunt of $L_2 = 12.88\,$pH. Thus, the total inductance at the output port is $L_{\rm out} = L_2/2 = 6.44\,$pH.

For $\tilde{\omega}_{\rm Res} L_{\rm in}, \tilde{\omega}_{\rm Res} L_{\rm out} \ll Z_0$ the resonance frequency of the coupled circuit is shifted due to the coupling inductors according to

$$\omega_{\rm Res} = \frac{1}{\sqrt{(L + L_{\rm in} + L_{\rm out})C}}. \tag{2}$$

The external linewidth of the resonator due to losses through the input port is given by [1]

$$\kappa_{\rm ex1} = \omega_{\rm Res} \frac{\pi}{2} \frac{L_{\rm in}^2}{L^2} \approx 2\pi \cdot 7\,{\rm kHz}. \tag{3}$$
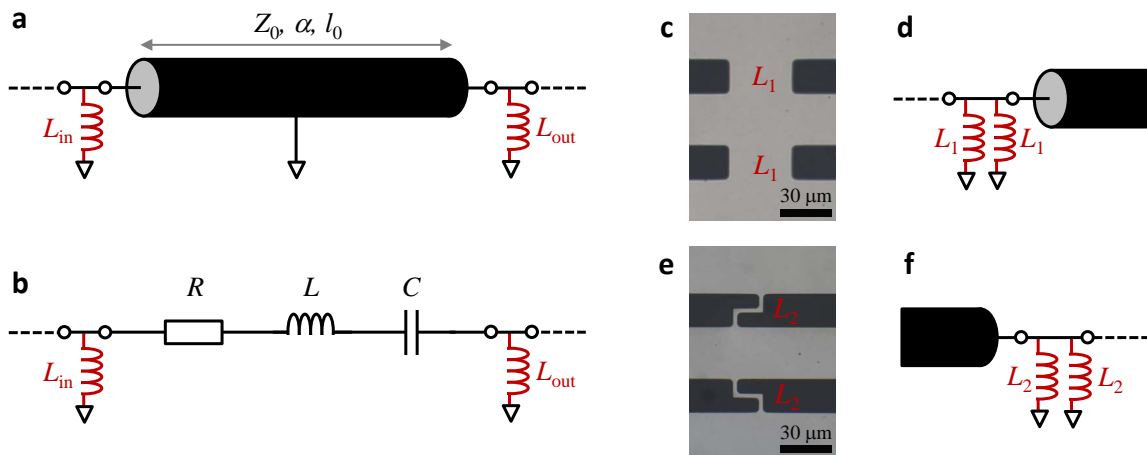
Supplementary Figure 3: **Resonator parameters and description**. **a** Schematic of an inductively coupled transmission line cavity as used in this experiment. The transmission line resonator is characterized by its characteristic impedance Z_0, its length l_0 and its attenuation constant α. The cavity is coupled at both ends to transmission feedlines via shunt inductors $L_{\rm in}$ and $L_{\rm out}$. **b** Lumped element circuit equivalent of 3a with the equivalent resistor R, the equivalent inductor L and the equivalent capacitor C. **c** [**e**] shows an optical image of the input [output] coupling inductors of our device and **d** [**f**] shows its circuits equivalent. As in the coplanar waveguide geometry we have two parallel shunt inductors L_1 [L_2] to ground at the input [output] port, the total input [output] coupling inductance is given by $L_{\rm in} = L_1/2$ [$L_{\rm out} = L_2/2$].

For the output port, we find

$$\kappa_{\rm ex2} = \omega_{\rm Res} \frac{\pi}{2} \frac{L_{\rm out}^2}{L^2} \approx 2\pi \cdot 134\,{\rm kHz}. \tag{4}$$

These linewidths correspond to a total external linewidth

$$\kappa_{\rm ex} = 2\pi \cdot 141\,{\rm kHz} \tag{5}$$

or a total external quality factor

$$Q_{\rm ex} = \frac{\omega_{\rm Res}}{\kappa_{\rm ex}} \approx 5 \cdot 10^4. \tag{6}$$

In liquid helium, at temperature $T_s = 4.2\,{\rm K}$, we measure a total quality factor of $Q \approx 10000$, indicating that the majority of the losses is due to thermal quasiparticles in the superconductor as well as due to dissipation in the normal conducting parts and the interfaces between the different metals.

SUPPLEMENTARY NOTE 3.   CAVITY TEMPERATURE DEPENDENCE

A.   Temperature calibration

The magnetic penetration depth $\lambda_{\rm L}$ in a BCS superconductor shows a temperature dependence, which can be approximately captured by [3]

$$\lambda_{\rm L}(T) = \frac{\lambda_{\rm L}(T = 0)}{\sqrt{1 - \left(\frac{T_s}{T_c}\right)^4}} \tag{7}$$

with the sample temperature T_s and the superconducting transition temperature T_c. The origin of this temperature dependence is the temperature dependence of the superconducting charge carrier density.

The total inductance of a superconducting resonator is given by the sum of the temperature independent geometric inductance L_g and the kinetic inductance, $L_k(T)$, which takes into account the kinetic energy of the superconducting charge carriers. For superconductors with a thickness larger than twice the penetration depth, the kinetic inductance is related to the magnetic penetration depth via

$$L_k(T) = \chi_g \mu_0 \lambda_{\mathrm{L}}(T), \tag{8}$$

where χ_g is a geometrical factor, taking into account the spatial distribution of the superconducting current density. In our samples, we have $h_{\mathrm{Nb}} = 500\,\mathrm{nm}$ and typically $\lambda_{\mathrm{L}}(T = 0) \sim 100\,\mathrm{nm}$. Thus, up to $T_s/T_c \approx 0.95$, which is much larger than all values of T_s/T_c in our experiment, $h_{\mathrm{Nb}} > 2\lambda_{\mathrm{T}}$ is fulfilled.

In general, also the coupling inductors have a kinetic contribution, but due to $L \gg L_{\mathrm{in}}, L_{\mathrm{out}}$ in our device, we neglect this small correction here. With the temperature dependent kinetic inductance, the resonance frequency is given by

$$\omega_{\mathrm{Res}}(T) = \frac{\omega_{\mathrm{Res0}}}{\sqrt{1 + \frac{L_k(T)}{L_0}}}, \tag{9}$$

where $L_0 = L_g + L_{\mathrm{in}} + L_{\mathrm{out}}$ is the inductance of the cavity without the kinetic contribution and $\omega_{\mathrm{Res0}} = 1/\sqrt{L_0 C}$ is the resonance frequency for $L_k = 0$ (not for $T = 0$).
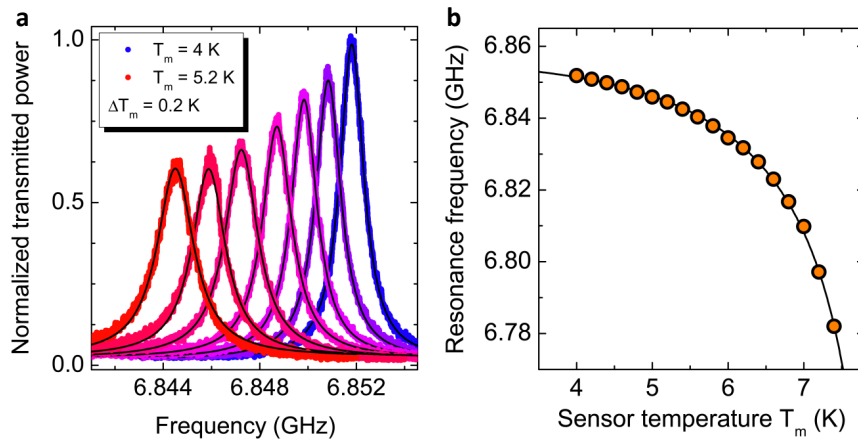
Supplementary Figure 4: **Temperature calibration**. **a** Cavity transmission spectra measured for sensor temperatures $4\,\mathrm{K} \leq T_m \leq 5.2\,\mathrm{K}$ in steps of $\Delta T_m = 0.2\,\mathrm{K}$. With increasing temperature, the resonance frequency shifts to lower values. Black lines are Lorentzian fits. **b** Cavity resonance frequency $\omega_{\mathrm{Res}}/2\pi$ vs sensor temperature. Circles are data extracted from the measurements and the black line is an analytical approximation curve (for details see text).

In our experiment, we take advantage of the temperature dependence of the cavity resonance frequency to tune it close to the atomic transition frequency. Figure 4a shows (smoothed) transmission spectra for different temperatures measured with the sensor mounted to the helium flow cryostat, which also hosts the chip. We observe the resonance frequency shifting towards lower values with increasing temperature. In Supplementary Figure 4b, we plot the extracted resonance frequency vs the measured temperature T_m.

As the thermometer is positioned inside the coldfinger of the flow cryostat $\sim 10\,\mathrm{cm}$ from the chip itself, we expect the sample temperature T_s to be different from the sensor temperature T_m by an offset temperature T_{off}, i.e.,

$$T_s = T_m + T_{\mathrm{off}}. \tag{10}$$

We note that we use a calibrated sensor and thus that the offset is not related to uncertainty of the sensor measurement, but due to the nature of the setup [4]. The chip and the microwave amplifier are mounted on a $10\,\mathrm{cm}$ high sample holder of oxygen-free high-conductivity copper. The cooling power of the chip is mainly limited by the thermal conductivity through the interfaces between the cryostat and the chip holder and between chip holder and the sapphire chip. Due to the requirement to have optical access to the chip region, $5\,\mathrm{mm}$ high slits have been cut into the thermal shield at $20\,\mathrm{K}$, which encloses the coldfinger tip and the sample holder in order to minimize the thermal

radiation from the room temperature environment. The final temperature of the chip is given by a combination of the cooling power from the coldfinger and the heating power due to thermal radiation from the environment. We find a very good agreement between the experimentally determined resonance frequencies shown in Supplementary Figure 4b, the transition temperature of our Nb $T_c = 9.2\,\mathrm{K}$ and Supplementary Eq. (9) when we assume $T_{\mathrm{off}} = 1.05\,\mathrm{K}$, $\omega_{\mathrm{Res0}} = 2\pi \cdot 6.94378\,\mathrm{GHz}$ and a kinetic inductance participation ratio $L_k(T=0)/L_0 = 0.02589$. The result is shown as black line in Supplementary Figure 4b and gives us a rough estimate for the temperature offset between sample and sensor.

B. Temperature fine calibration and full cavity characterization

As the offset temperature T_{off} is not exactly constant between $5\,\mathrm{K}$ and $9\,\mathrm{K}$ and as all our experiments are done within a limited temperature window of $\sim 1\,\mathrm{K}$, we performed a more detailed cavity characterization in the corresonding temperature interval. The results of this detailed cavity characterization are shown in Supplementary Figure 5. In Supplementary Figure 5a, we plot the resonance frequency vs the sample temperature, where the sample temperature was determined from the analytical approximation shown as black line. To achieve the best match in this temperature region, we had to adjust the offset temperature to $T_{\mathrm{off}} = 1.09\,\mathrm{K}$, but kept all other parameters used above.
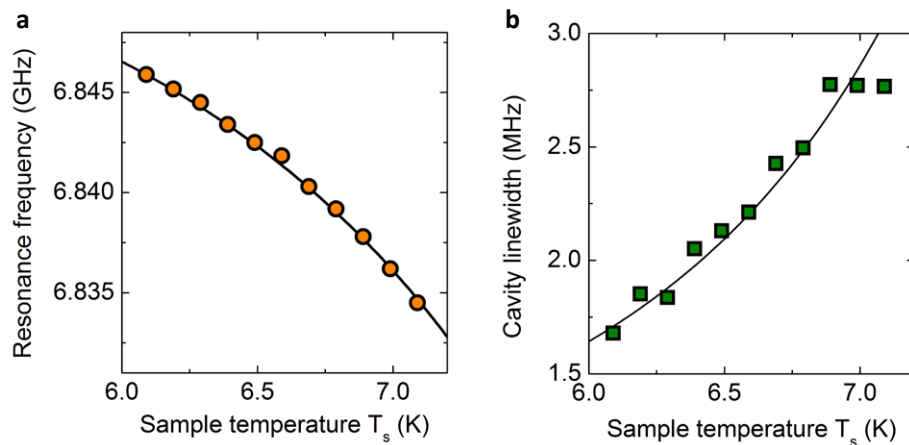
Supplementary Figure 5: **Temperature dependence of the cavity parameters**. **a** Cavity resonance frequency $\omega_{\mathrm{Res}}/2\pi$ vs sample temperature. Circles are data extracted from the measurements and the black line is an analytical approximation curve (details see text). **b** Cavity linewidth $\kappa/2\pi$ vs sample temperature extracted from Lorentzian fits. Squares are experimental data and the black line is an approximation based on the two-fluid model (details see text). The data point at $6.99\,\mathrm{K}$ is linearly interpolated from points at $6.89\,\mathrm{K}$ and $7.09\,\mathrm{K}$.

In addition to the resonance frequency, we also extracted the resonance linewidth κ for each temperature, which is shown in Supplementary Figure 5b. From the two-fluid model [3, 5], it follows that the surface resistance of a superconductor is given by

$$R_s = \frac{1}{2}\omega^2 \mu_0^2 \sigma_1 \lambda_{\mathrm{L}}^3 \tag{11}$$

where $\sigma_1 \propto n_n/n_e$ is the real part of the complex two-fluid conductivity with the quasiparticle density n_n and the total electron density n_e. From the temperature dependence of λ_{L} and the two-fluid model, the temperature dependence of the superconducting charge carrier density is given by

$$\frac{n_s(T)}{n_e} = 1 - \left(\frac{T_s}{T_c}\right)^4. \tag{12}$$

This leads to the quasiparticle density fraction

$$\frac{n_n(T)}{n_e} = \left(\frac{T_s}{T_c}\right)^4. \tag{13}$$

Taking the relation $\kappa_s \propto R_s$ for the quasiparticle induced losses and assuming $\omega_{\text{Res}}, L_{\text{tot}} \approx \text{const.}$, which for this consideration is reasonable as their relative change is only $\sim 10^{-2}$, we get as cavity linewidth temperature dependence

$$\kappa(T) = \kappa_0 + \kappa_1 \left(\frac{T_s}{T_c}\right)^4 \cdot \left[1 - \left(\frac{T_s}{T_c}\right)^4\right]^{-\frac{3}{2}} \tag{14}$$

with a temperature independent contribution κ_0 and the scaling factor κ_1. Figure 5b shows an approximation to the data using this expression with $\kappa_0 = 2\pi \cdot 850\,\text{kHz}$ and $\kappa_1 = 2\pi \cdot 3.25\,\text{MHz}$ ($T_{\text{off}} = 1.09\,\text{K}$) as lines.

C. Influence of the magnetic trapping fields

Applying an external magnetic field can shift the cavity frequency as well as the cavity linewidth due to Meissner screening currents [6] and the presence of Abrikosov vortices [7, 8]. In our experiment, we apply only small fields in the $100\,\mu\text{T}$ range, but due to the fact that we also apply a field during the transition to the superconducting state, we will trap some vortices in the cavity leads [9]. As the magnetic field distribution including vortices is very complicated for our device, we describe the field-induced property shifts phenomenologically by slightly adjusting the kinetic inductance participation ratio L_k/L_0 and the parameter κ_1.

In Supplementary Figure 6a, we plot the zero magnetic field data points and the analytic expressions (lines) as derived in the previous section and in 6b we show the experimental data obtained within the full magnetic trapping field configuration. For comparison, we also plot the lines of 6a in 6b, but in grey, demonstrating that the magnetic fields indeed lead to a small resonance frequency downshift and a slight increase of the linewidth. Both effects can be captured by using $L_k(B_{\text{trap}})/L_0 = 0.02593$ and $\kappa_1(B) = 1.3\kappa_1(0)$. The result is shown as black dashed lines in 6b and is in excellent agreement with the data.
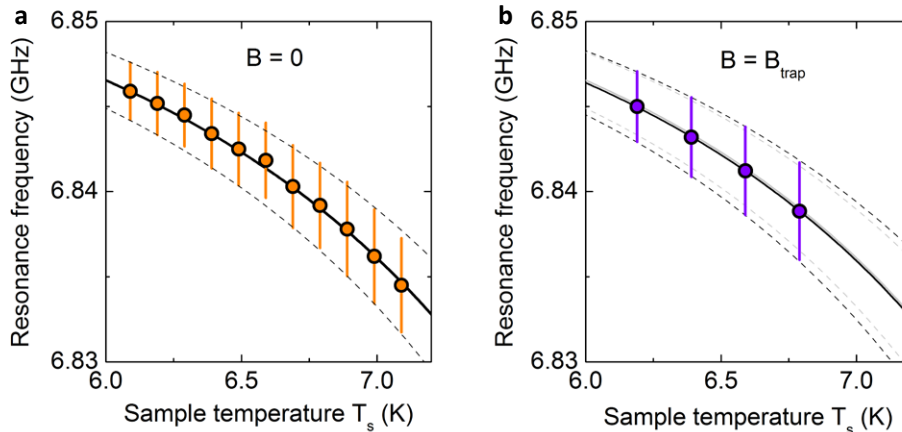
Supplementary Figure 6: **Temperature and magnetic field dependence of the cavity parameters in the experimentally relevant range**. **a** Cavity resonance frequency and linewidth vs sample temperature in zero magnetic field. Circles show the resonance frequency values, error bars on both sides of the points indicate the range $(\omega_{\text{Res}} \pm \kappa)/2\pi$. Lines show corresponding analytical approximations as described in the main text. **b** Cavity resonance frequency and linewidth vs sample temperature with magnetic trapping fields applied. Circles show the resonance frequency values, error bars on both sides of the points indicate the range $(\omega_{\text{cav}} \pm \kappa)/2\pi$. Gray lines show the corresponding analytical approximations for $B = 0$ as in a, and black lines indicate slightly modified expressions as described in the main text.

SUPPLEMENTARY NOTE 4.   MAGNETIC FIELD SIMULATIONS

The magnetic field simulations in this work have been performed using the software package 3D-MLSI [2]. For the calculations of the RF magnetic field, simplified versions of our real chip were used, as the full structure was too large to be computed to the full extent. We do not expect the modifications (e.g. shortening the Z-shaped trapping wire to the trapping region), however, to have a significant impact onto the final results.

A. Coupling per photon and atom

The microwave current of the fundamental mode along the resonator is given by

$$I(l) = I_0 \cos\left(2\pi\frac{l}{\lambda_0}\right) \tag{15}$$

where l is the coordinate along the resonator starting from the input port with $l = 0$, $\lambda_0 \approx 18.7\,\text{mm}$ is the resonance wavelength and I_0 is the amplitude in the current antinodes. To calculate the coupling rate g between a single photon and a single atom in the cavity, we estimate the zero point fluctuations of the microwave current in the resonator and at the position of the atoms (current antinode) by

$$\frac{1}{2}\hbar\omega_{\text{cav}} = \int_0^{\lambda_0/2} L' I_{\text{zpf}}^2 \cos^2\left(2\pi\frac{l}{\lambda_0}\right) dl \tag{16}$$

$$= \frac{\lambda_0}{4} L' I_{\text{zpf}}^2 \tag{17}$$

where the inductance per unit length is $L' = 409\,\text{nH/m}$ (kinetic inductance contributions are neglected here due to their smallness) and $I_{\text{zpf}} = I_{\text{zpf0}}/\sqrt{2}$ is the root mean square of the zero point fluctuation amplitude I_{zpf0}. With $\omega_{\text{cav}} = 2\pi \cdot 6.84\,\text{GHz}$ and $\lambda_0 \approx 18.7\,\text{mm}$ we get

$$I_{\text{zpf}} = \sqrt{\frac{2\hbar\omega_{\text{cav}}}{\lambda_0 L'}} \approx 33.5\,\text{nA}. \tag{18}$$

To relate this to the coupling, we calculate the magnetic field B_{ph} related to this current at the position of the atoms by means of finite element simulations using the software package 3D-MLSI [2].

Finally, we take into account the position of the atomic cloud along the resonator, which reduces the effective magnetic field to $\sim 0.95 B_{\text{ph}}$. Supplementary Figure 7 shows the magnetic microwave field zero point fluctuations obtained from these simulations in a cross-section of the coplanar waveguide at the position of the atoms.
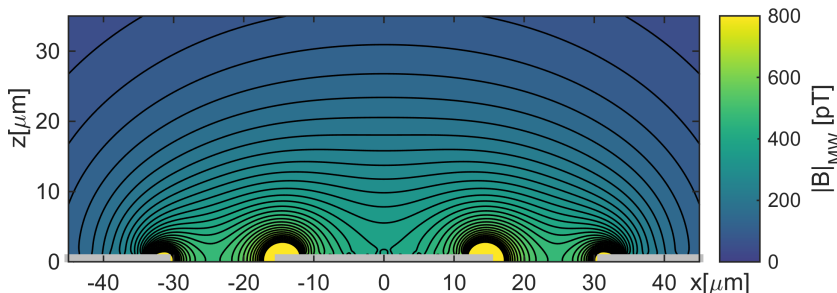
Supplementary Figure 7: **Single-photon microwave magnetic field in the resonator**. The magnetic microwave field zero point fluctuation amplitude $|B| = |B_{\text{ph}}|\,[\text{nT}]$ obtained by finite element simulations above the coplanar microwave structure. The coplanar waveguide structure is indicated by the grey bars at the bottom. The thickness of the CPW is not to scale.

From the magnetic microwave field, we calculate the single-atom coupling rate as

$$g = \frac{|B_{\text{ph}}(x,y)| \cdot |\mu|}{\hbar} \tag{19}$$

with the magnitude of the dipole transition matrix element $|\mu| = 0.25\mu_{\text{B}}$. The result is shown in Fig. 1f of the main paper.

B. The radio-frequency magnetic field

For the two-photon experiments and the corresponding simulations, we also need the magnetic field of the radio-frequency (RF) current, which is sent through the Z-shaped trapping wire. Thus, we calculate the magnetic field for

a current of $I_{RF} = 1\,\mathrm{mA}$ on the trapping wire and show the result at the position of the atoms in Supplementary Figure 8.

Supplementary Figure 8: **Magnetic field of a current through the trapping wire in the resonator**. The plot shows the magnetic field $|B_{RF}|\,[\mu\mathrm{T}]$ generated in the microwave cavity, when a current of $I_{RF} = 1\,\mathrm{mA}$ is flowing through the trapping wire. The grey bars at the bottom indicate the position of the resonator leads. The centre bar shows the centre conductor, the left bar corresponds to the $50\,\mu$m ground plane towards the trapping wire and the right bar corresponds to the large purely superconducting ground. The magnetic field is mainly guided through the right resonator gap due to the closed superconducting loop around the left gap (defined by centre conductor, ground and the coupling inductors).

SUPPLEMENTARY NOTE 5. RECONSTRUCTION OF THE CAVITY FIELD WITH RAMSEY INTERFEROMETRY

In order to measure the cavity field strength as depicted in Fig. 2 in the main article, we prepare the atoms in a superposition of the states $|1, -1\rangle$ and $|2, 1\rangle$ with a two-photon $\pi/2$-pulse using external radio- and MW frequencies ω_{RF} and ω_{extMW}. After a variable waiting time T_{Ramsey}, a second $\pi/2$-pulse is irradiated and the population in the two hyperfine states is measured. The two-photon detuning with respect to the atomic transition frequency is chosen to be $\omega_{Ramsey} = \omega_{at} - (\omega_{RF} + \omega_{extMW}) = -2\pi \cdot 500\,\mathrm{Hz}$. The presence of a microwave field in the cavity shifts the atomic transition frequency to $\omega_{at} + \delta_{dress}$, so the measured frequency in the Ramsey sequence changes. Supplementary Figure 9 shows two exemplary Ramsey measurements taken at a chip temperature of 6.4 K. The first

Supplementary Figure 9: **Recorded Ramsey fringes for different resonator driving frequencies.** Shown are two exemplary measurements for dressing frequencies, both recorded at a chip temperature of 6.4 K. Top: $\omega_{dress} = 2\pi \cdot 6.838\,\mathrm{GHz}$ yielding a shift of $\delta_{dress}/2\pi = -68.8\,\mathrm{Hz}$. Bottom: $\omega_{dress} = 2\pi \cdot 6.843\,\mathrm{GHz}$, yielding a shift of $\delta_{dress}/2\pi = -21.2\,\mathrm{Hz}$.

measurement yields a shift of $\delta_{dress}/2\pi = -68.8\,\mathrm{Hz}$ for a driving field of $\omega_{dress} = 2\pi \cdot 6.838\,\mathrm{GHz}$, the second one yields $\delta_{dress}/2\pi = -21.2\,\mathrm{Hz}$ for $\omega_{dress} = 2\pi \cdot 6.843\,\mathrm{GHz}$. b7b1c3ff

SUPPLEMENTARY NOTE 6. SIMULATED RABI OSCILLATIONS IN THE CAVITY

A. One photon Rabi oscillations

Numerical simulations of the coherent Rabi oscillations of atomic ensembles in the cavity yield further insight into the observed dephasing rates. We assume a thermal ensemble of atoms with a temperature of $T_a = 2000\,\text{nK}$ trapped in a harmonic magnetic trap with $\omega_x = 2\pi \cdot 400\,\text{s}^{-1}$, $\omega_y = 2\pi \cdot 25\,\text{s}^{-1}$, $\omega_z = 2\pi \cdot 600\,\text{s}^{-1}$. The centre of the trap is assumed $20\,\mu\text{m}$ from the chip surface, as depicted in Fig. 1f in the main article.

For the one-photon Rabi oscillation, the Rabi frequency is much higher than the oscillation frequency of the atoms in the trapping potential, i.e. $\Omega_0 \gg \omega_z$. We therefore can assume a static Gaussian density distribution of atoms in the trap, and use a total atom number of 1.2×10^5 atoms for the simulations. We use the numerically calculated field strength depicted in Supplementary Figure 7, multiplied by a constant numerical factor to match the observed Rabi oscillation frequency. For each position $\mathbf{r}_i$, the probability to find atoms in the excited state is computed as

$$p_2(\mathbf{r}_i, t) = \frac{\Omega_0(\mathbf{r}_i)^2}{\tilde{\Omega}(\mathbf{r}_i)^2} \sin^2\left(\frac{\tilde{\Omega}(\mathbf{r}_i)^2}{2} t\right),\tag{20}$$

where $\tilde{\Omega}(\mathbf{r}_i)^2 = \Omega_0(\mathbf{r}_i)^2 + \Delta(\mathbf{r}_i)$ is the generalized Rabi frequency, and $\Delta(\mathbf{r}_i)$ the magnetic-field dependent detuning of the microwave to the atomic transition. The probability $p_2(\mathbf{r}_i, t)$ is multiplied with the local atomic density $n_{\text{at}}(\mathbf{r}_i)$ and summation over all atoms yields the total atom number in the excited state. The simulated results closely match the observed dephasing of the Rabi oscillations, as seen in Fig. 3a in the main paper.

B. Two-photon Rabi oscillations

For the simulated two-photon Rabi oscillations, we assume a three level system of states $|1, -1\rangle$, $|2, 0\rangle$, and $|2, 1\rangle$.

States $|1, -1\rangle$ and $|2, 0\rangle$ are coupled by the cavity microwave field with the Rabi frequency Ω_{MW}. An additional radio frequency Ω_{RF} couples the state $|2, 0\rangle$ to the state $|2, 1\rangle$. Both the microwave and the radio frequency field are detuned to the transition to the intermediate state $|2, 0\rangle$ by the detuning $\pm\Delta$, c.f. Fig. 5b in the main article. The inhomogeneity of the cavity field Ω_{MW} is the same as for the one-photon case above. The spatial dependence of the radio-frequency field Ω_{RF} is simulated with the software package 3D-MLSI by applying a current in the Z-shaped wire and calculating the Meissner screening currents close to the resonator, c.f. 8. As the effective Rabi frequency is much lower as in the one-photon case, the assumption of static atoms no longer holds. The motion of atoms through the spatially inhomogeneous MW and RF field leads to a time dependence of the Rabi frequency seen by each atom.
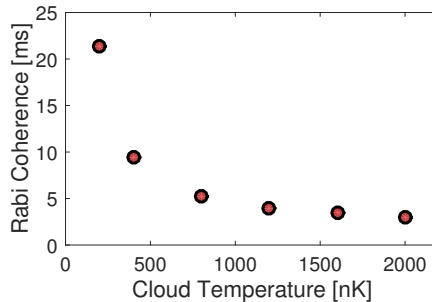
Supplementary Figure 10: **Simulated coherence of the Rabi oscillations as a function of the cloud temperature.** The simulations assume trapping frequencies as in the experiment, i.e. $\omega_y = 2\pi \cdot 25\,\text{s}^{-1}$, $\omega_x = 2\pi \cdot 400\,\text{s}^{-1}$, $\omega_z = 2\pi \cdot 600\,\text{s}^{-1}$. The high coherence for low temperatures shows that the inhomogeneity of the MW field is the primary source of the dephasing.

.

To account for this, we randomly initialize 5000 non-interacting particles in the state $|1, -1\rangle$ in the harmonic potential with a distribution corresponding to a temperature of $800\,\text{nK}$. We then simulate the movement of the atoms through the potential and the evolution of the three states with a Runge-Kutta calculation of fourth order. Stability of the simulations was ensured by changing the time steps in the calculations. The main source of the dephasing in the Rabi oscillations is the inhomogeneity of the MW field. This can be seen from simulations with colder and thus

smaller clouds, as visible in Supplementary Figure 10.

<div style="text-align:center">———————————</div>

SUPPLEMENTARY REFERENCES

[1] Bothner, D. et al., Inductively coupled superconducting half wavelength resonators as persistent current traps for ultracold atoms, *New J. Phys.* **15**, 093024 (2013)

[2] Khapaev, M. M., Kupriyanov, M. Y., Goldobin, E., and Siegel, M., Current distribution simulation for superconducting multi-layered structures, *Supercond. Sci. Technol.* **16**, 24 (2003)

[3] Tinkham, M. *Introduction to Superconductivity: Second Edition*, Dover Books on Physics (Dover Publications, 2004)

[4] Cano, D. et al., Experimental system for research on ultracold atomic gases near superconducting microstructures, *Eur. Phys. J. D* **63**, 17-23 (2010)

[5] Buckel, W. and Kleiner,R. *Superconductivity: fundamentals and applications* (Wiley-VCH, 2004)

[6] Healey, J. E., Lindström, T., Colclough, M. S., Muirhead, C. M., and Tzalenchuk, A. Ya., Magnetic field tuning of coplanar microwave resonators, *Appl. Phys. Lett.* **93**, 043513 (2008)

[7] Song, C. et al., Microwave response of vortices in superconducting thin films of Re and Al, *Phys. Rev. B* **79**, 174512 (2009)

[8] Bothner, D. et al., Magnetic hysteresis effects in superconducting coplanar microwave resonators, *Phys. Rev. B* **86**, 014517 (2012)

[9] Stan, G., Field, S. B., and Martinis, J. M., Critical field for complete vortex expulsion from narrow superconducting strips, *Phys. Rev. Lett.* **92**, 097003 (2004)

Bibliography

[1] W. Kozaczuk, *Enigma: how the German machine cipher was broken, and how it was read by the Allies in World War Two.* Univ Pubns of Amer, 1984.

[2] A. M. Turing, "On computable numbers, with an application to the entscheidungsproblem," *Proceedings of the London Mathematical Society*, vol. s2-42, no. 1, pp. 230–265, 1937. [Online]. Available: http://dx.doi.org/10.1112/plms/s2-42.1.230

[3] M. Davis, "The definition of universal turing machine," *Proceedings of the American Mathematical Society*, vol. 8, no. 6, pp. 1125–1126, 1957.

[4] C. E. Shannon, "A universal turing machine with two internal states," *Automata studies*, vol. 34, pp. 157–165, 1956.

[5] J. von Neumann, "First draft of a report on the edvac," *IEEE Annals of the History of Computing*, vol. 15, no. 4, pp. 27–75, 1993.

[6] R. R. Schaller, "Moore's law: past, present and future," *IEEE spectrum*, vol. 34, no. 6, pp. 52–59, 1997.

[7] J. Weizenbaum, "On the impact of the computer on society," *Science*, vol. 176, no. 4035, pp. 609–614, 1972.

[8] C. Mackenzie, *Coded character sets: history and development*, ser. The Systems programming series. Addison-Wesley Pub. Co., 1980. [Online]. Available: https://books.google.de/books?id=6-tQAAAAMAAJ

[9] C. H. Bennett and R. Landauer, "The fundamental physical limits of computation," vol. 253, pp. 48–56, 07 1985.

[10] R. Feynman, "Simulating physics with computers," *International Journal of Theoretical Physics*, vol. 21, pp. 467–488, 1982. [Online]. Available: http://dx.doi.org/10.1007/BF02650179

[11] S. Haroche and J.-M. Raimond, "Quantum computing: dream or nightmare?" *Physics Today*, vol. 49, no. 8, pp. 51–54, 1996.

[12] C. Moore and M. Nilsson, "Parallel quantum computation and quantum codes," *SIAM Journal on Computing*, vol. 31, no. 3, pp. 799–815, 2001. [Online]. Available: https://doi.org/10.1137/S0097539799355053

[13] D. Deutsch, "Quantum theory, the church–turing principle and the universal quantum computer," *Proc. R. Soc. Lond. A*, vol. 400, no. 1818, pp. 97–117, 1985.

[14] I. Deutsch, Barenco, and Ekert, *Proc. Roy. Soc. Lond.*, vol. x, p. 669, 1995.

[15] D. R. Simon, "On the power of quantum computation," *SIAM Journal on Computing*, vol. 26, pp. 116–123, 1994.

[16] D. Deutsch and R. Jozsa, "Rapid solution of problems by quantum computation," *Proceedings of the Royal Society of London. Series A: Mathematical and Physical Sciences*, vol. 439, no. 1907, pp. 553–558, 1992. [Online]. Available: http://rspa.royalsocietypublishing.org/content/439/1907/553.abstract

[17] G. Brassard and P. Hoyer, "An exact quantum polynomial-time algorithm for simon's problem," in *Theory of Computing and Systems, 1997., Proceedings of the Fifth Israeli Symposium on.* IEEE, 1997, pp. 12–23.

[18] P. Shor, "Polynomial-time algorithms for prime factorization and discrete logarithms on a quantum computer," *SIAM Journal on Computing*, vol. 26, no. 5, pp. 1484–1509, 1997. [Online]. Available: http://epubs.siam.org/doi/abs/10.1137/S0097539795293172

[19] L. K. Grover, "A fast quantum mechanical algorithm for database search," in *Proceedings of the twenty-eighth annual ACM symposium on Theory of computing*, ser. STOC '96. New York, NY, USA: ACM, 1996, pp. 212–219. [Online]. Available: http://doi.acm.org/10.1145/237814.237866

[20] A. W. Harrow, A. Hassidim, and S. Lloyd, "Quantum algorithm for linear systems of equations," *Physical review letters*, vol. 103, no. 15, p. 150502, 2009.

[21] "Quantum computers are about to get real," https://www.sciencenews.org/article/quantum-computers-are-about-get-real, society for Science & the Public, Magazine issue: Vol. 191, No. 13, July 8, 2017, p. 28.

[22] G. Arun and V. Mishra, "A review on quantum computing and communication," in *2014 2nd International Conference on Emerging Technology Trends in Electronics, Communication and Networking*, Dec 2014, pp. 1–5.

[23] J. Gea-Banacloche, "Quantum computers: A status update," *Proceedings of the IEEE*, vol. 98, no. 12, pp. 1983–1985, 2010.

[24] H. Häffner, C. F. Roos, and R. Blatt, "Quantum computing with trapped ions," *Phys. Rep.*, vol. 469, pp. 155–203, Dec. 2008.

[25] D. Jonathan, M. B. Plenio, and P. L. Knight, "Fast quantum gates for cold trapped ions," *Phys. Rev. A*, vol. 62, p. 42307, 2000.

[26] R. Blatt and D. Wineland, "Entangled states of trapped atomic ions," *Nature*, vol. 453, pp. 1008–1015, Jun. 2008.

[27] J. Chiaverini, J. Britton, D. Leibfried, E. Knill, M. D. Barrett, R. B. Blakestad, W. M. Itano, J. D. Jost, C. Langer, R. Ozeri, T. Schaetz, and D. J. Wineland, "Implementation of the semiclassical quantum fourier transform in a scalable system," *Science*, vol. 308, no. 5724, pp. 997–1000, 2005. [Online]. Available: http://www.sciencemag.org/content/308/5724/997.abstract

[28] T. Monz, K. Kim, W. Hänsel, M. Riebe, A. S. Villar, P. Schindler, M. Chwalla, M. Hennrich, and R. Blatt, "Realization of the quantum toffoli gate with trapped ions," *Phys. Rev. Lett.*, vol. 102, p. 040501, Jan 2009. [Online]. Available: http://link.aps.org/doi/10.1103/PhysRevLett.102.040501

[29] J. I. Cirac and P. Zoller, "Quantum computations with cold trapped ions," *Phys. Rev. Lett.*, vol. 74, pp. 4091–4094, May 1995. [Online]. Available: http://link.aps.org/doi/10.1103/PhysRevLett.74.4091

[30] C. Monroe, D. M. Meekhof, B. E. King, W. M. Itano, and D. J. Wineland, "Demonstration of a fundamental quantum logic gate," *Phys. Rev. Lett.*, vol. 75, pp. 4714–4717, Dec 1995. [Online]. Available: http://link.aps.org/doi/10.1103/PhysRevLett.75.4714

[31] T. Monz, P. Schindler, J. T. Barreiro, M. Chwalla, D. Nigg, W. A. Coish, M. Harlander, W. Hänsel, M. Hennrich, and R. Blatt, "14-qubit entanglement: Creation and coherence," *Phys. Rev. Lett.*, vol. 106, p. 130506, Mar 2011. [Online]. Available: http://link.aps.org/doi/10.1103/PhysRevLett.106.130506

[32] W. S. Warren, "The usefulness of nmr quantum computing," *Science*, vol. 277, no. 5332, pp. 1688–1690, 1997. [Online]. Available: http://www.sciencemag.org/content/277/5332/1688.short

[33] J. A. Jones and M. Mosca, "Implementation of a quantum algorithm on a nuclear magnetic resonance quantum computer," *J. Chem. Phys.*, vol. 109, pp. 1648–1653, Aug. 1998.

[34] L. M. K. Vandersypen, M. Steffen, G. Breyta, C. S. Yannoni, M. H. Sherwood, and I. L. Chuang, "Experimental realization of Shor's quantum factoring algorithm using nuclear magnetic resonance," *Nature*, vol. 414, pp. 883–887, Dec. 2001.

[35] J. L. O'Brien, "Optical quantum computing," *Science*, vol. 318, no. 5856, pp. 1567–1570, 2007. [Online]. Available: http://www.sciencemag.org/content/318/5856/1567.abstract

[36] A. Politi, M. J. Cryan, J. G. Rarity, S. Yu, and J. L. O'Brien, "Silica-on-silicon waveguide quantum circuits," *Science*, vol. 320, no. 5876, pp. 646–649, 2008. [Online]. Available: http://www.sciencemag.org/content/320/5876/646.abstract

[37] A. Politi, J. C. F. Matthews, and J. L. O'Brien, "Shor's quantum factoring algorithm on a photonic chip," *Science*, vol. 325, no. 5945, p. 1221,

89

2009. [Online]. Available: http://www.sciencemag.org/content/325/5945/1221.abstract

[38] J. L. O'Brien, G. J. Pryde, A. G. White, and T. C. Ralph, "High-fidelity z-measurement error encoding of optical qubits," *Phys. Rev. A*, vol. 71, p. 060303, Jun 2005. [Online]. Available: http://link.aps.org/doi/10.1103/PhysRevA.71.060303

[39] D. Loss and D. P. DiVincenzo, "Quantum computation with quantum dots," *Phys. Rev. A*, vol. 57, pp. 120–126, Jan 1998. [Online]. Available: http://link.aps.org/doi/10.1103/PhysRevA.57.120

[40] A. Imamoḡlu, D. D. Awschalom, G. Burkard, D. P. DiVincenzo, D. Loss, M. Sherwin, and A. Small, "Quantum information processing using quantum dot spins and cavity qed," *Phys. Rev. Lett.*, vol. 83, pp. 4204–4207, Nov 1999. [Online]. Available: http://link.aps.org/doi/10.1103/PhysRevLett.83.4204

[41] X. Li, Y. Wu, D. Steel, D. Gammon, T. H. Stievater, D. S. Katzer, D. Park, C. Piermarocchi, and L. J. Sham, "An all-optical quantum gate in a semiconductor quantum dot," *Science*, vol. 301, no. 5634, pp. 809–811, 2003. [Online]. Available: http://www.sciencemag.org/content/301/5634/809.abstract

[42] M. Saffman, T. G. Walker, and K. Mølmer, "Quantum information with rydberg atoms," *Rev. Mod. Phys.*, vol. 82, no. 3, pp. 2313–2363, Aug 2010.

[43] M. Saffman and T. G. Walker, "Analysis of a quantum logic device based on dipole-dipole interactions of optically trapped rydberg atoms," *Phys. Rev. A*, vol. 72, p. 022347, Aug 2005. [Online]. Available: http://link.aps.org/doi/10.1103/PhysRevA.72.022347

[44] M. Saffman, "Quantum computing with atomic qubits and rydberg interactions: progress and challenges," *J. Phys. B: At., Mol. and Opt. Phys.*, vol. 49, no. 20, p. 202001, 2016. [Online]. Available: http://stacks.iop.org/0953-4075/49/i=20/a=202001

[45] E. Urban, T. A. Johnson, T. Henage, L. Isenhower, D. D. Yavuz, T. G. Walker, and M. Saffman, "Observation of Rydberg blockade between two atoms," *Nat. Phys.*, vol. 5, pp. 110–114, Feb. 2009.

[46] A. Gaëtan, Y. Miroshnychenko, T. Wilk, A. Chotia, M. Viteau, D. Comparat, P. Pillet, A. Browaeys, and P. Grangier, "Observation of collective excitation of two individual atoms in the Rydberg blockade regime," *Nat. Phys.*, vol. 5, pp. 115–118, Feb. 2009.

[47] D. Jaksch, J. I. Cirac, P. Zoller, S. L. Rolston, R. Côté, and M. D. Lukin, "Fast quantum gates for neutral atoms," *Phys. Rev. Lett.*, vol. 85, p. 2208, 2000.

[48] M. D. Lukin, M. Fleischhauer, R. Cote, L. M. Duan, D. Jaksch, J. I. Cirac, and P. Zoller, "Dipole blockade and quantum information processing in mesoscopic atomic ensembles," *Phys. Rev. Lett.*, vol. 87, no. 3, p. 037901, Jun 2001.

[49] T. Wilk, A. Gaëtan, C. Evellin, J. Wolters, Y. Miroshnychenko, P. Grangier, and A. Browaeys, "Entanglement of two individual neutral atoms using rydberg blockade," *Phys. Rev. Lett.*, vol. 104, p. 010502, Jan 2010. [Online]. Available: http://link.aps.org/doi/10.1103/PhysRevLett.104.010502

[50] L. Isenhower, E. Urban, X. L. Zhang, A. T. Gill, T. Henage, T. A. Johnson, T. G. Walker, and M. Saffman, "Demonstration of a neutral atom controlled-not quantum gate," *Phys. Rev. Lett.*, vol. 104, p. 010503, Jan 2010. [Online]. Available: http://link.aps.org/doi/10.1103/PhysRevLett.104.010503

[51] J. Weber, W. Koehl, J. Varley, A. Janotti, B. Buckley, C. Van de Walle, and D. D. Awschalom, "Quantum computing with defects," *Proceedings of the National Academy of Sciences*, vol. 107, no. 19, pp. 8513–8518, 2010.

[52] F. Jelezko, T. Gaebel, I. Popa, M. Domhan, A. Gruber, and J. Wrachtrup, "Observation of coherent oscillation of a single nuclear spin and realization of a two-qubit conditional quantum gate," *Physical Review Letters*, vol. 93, no. 13, p. 130501, 2004.

[53] L. DiCarlo, J. M. Chow, J. M. Gambetta, L. S. Bishop, B. R. Johnson, D. I. Schuster, J. Majer, A. Blais, L. Frunzio, S. M. Girvin, and R. J. Schoelkopf, "Demonstration of two-qubit algorithms with a superconducting quantum processor," *Nature*, vol. 460, no. 7252, pp. 240–244, JUL 9 2009.

[54] A. Fedorov, L. Steffen, M. Baur, M. P. da Silva, and A. Wallraff, "Implementation of a Toffoli gate with superconducting circuits," *Nature*, vol. 481, pp. 170–172, Jan. 2012.

[55] M. D. Reed, L. Dicarlo, S. E. Nigg, L. Sun, L. Frunzio, S. M. Girvin, and R. J. Schoelkopf, "Realization of three-qubit quantum error correction with superconducting circuits," *Nature*, vol. 482, pp. 382–385, Feb. 2012.

[56] E. Lucero, R. Barends, Y. Chen, J. Kelly, M. Mariantoni, A. Megrant, P. O'Malley, D. Sank, A. Vainsencher, J. Wenner, T. White, Y. Yin, A. N. Cleland, and J. M. Martinis, "Computing prime factors with a Josephson phase qubit quantum processor," *Nat. Phys.*, vol. 8, pp. 719–723, Oct. 2012.

[57] "List of companies involved in quantum computing or communication," https://en.wikipedia.org/wiki/List_of_companies_involved_in_quantum_computing_or_communication.

[58] M. H. Devoret and R. J. Schoelkopf, "Superconducting circuits for quantum information: an outlook," *Science*, vol. 339, no. 6124, pp. 1169–1174, 2013.

[59] A. Wallraff, D. Schuster, A. Blais, L. Frunzio, R. Huang, J. Majer, S. Kumar, S. Girvin, and R. Schoelkopf, "Strong coupling of a single photon to a superconducting qubit using circuit quantum electrodynamics," *Nature*, vol. 431, no. 7005, pp. 162–167, SEP 9 2004.

[60] M. A. Sillanpää, J. I. Park, and R. W. Simmonds, "Coherent quantum state storage and transfer between two phase qubits via a resonant cavity," *Nature*, vol. 449, pp. 438–442, Sep. 2007.

[61] J. Majer, J. M. Chow, J. M. Gambetta, J. Koch, B. R. Johnson, J. A. Schreier, L. Frunzio, D. I. Schuster, A. A. Houck, A. Wallraff, A. Blais, M. H. Devoret, S. M. Girvin, and R. J. Schoelkopf, "Coupling superconducting qubits via a cavity bus," *Nature*, vol. 449, pp. 443–447, Sep. 2007.

[62] A. Wallraff, D. Schuster, A. Blais, L. Frunzio, J. Majer, M. Devoret, S. Girvin, and R. Schoelkopf, "Approaching unit visibility for control of a superconducting qubit with dispersive readout," *Physical review letters*, vol. 95, no. 6, p. 060501, 2005.

[63] L. DiCarlo, M. D. Reed, L. Sun, B. R. Johnson, J. M. Chow, J. M. Gambetta, L. Frunzio, S. M. Girvin, M. H. Devoret, and R. J. Schoelkopf, "Preparation and measurement of three-qubit entanglement in a superconducting circuit," *Nature*, vol. 467, pp. 574–578, Sep. 2010.

[64] R. K. Hoffmann, "Handbook of microwave integrated circuits," *Norwood, MA, Artech House, Inc., 1987, 544 p. Translation.*, 1987.

[65] L. Frunzio, A. Wallraff, D. Schuster, J. Majer, and R. Schoelkopf, "Fabrication and characterization of superconducting circuit qed devices for quantum computation," *IEEE transactions on applied superconductivity*, vol. 15, no. 2, pp. 860–863, 2005.

[66] D. P. DiVincenzo, "The Physical Implementation of Quantum Computation," *Fortschritte der Physik*, vol. 48, pp. 771–783, 2000.

[67] Y. Wang, Y. Li, Z.-q. Yin, and B. Zeng, "16-qubit ibm universal quantum computer can be fully entangled," *arXiv preprint arXiv:1801.03782*, 2018.

[68] Z. Kim, B. Suri, V. Zaretskey, S. Novikov, K. D. Osborn, A. Mizel, F. C. Wellstood, and B. S. Palmer, "Decoupling a Cooper-pair box to enhance the lifetime to 0.2 ms," *Phys. Rev. Lett.*, vol. 106, p. 120501, Mar 2011. [Online]. Available: http://link.aps.org/doi/10.1103/PhysRevLett.106.120501

[69] H. Paik, D. I. Schuster, L. S. Bishop, G. Kirchmair, G. Catelani, A. P. Sears, B. R. Johnson, M. J. Reagor, L. Frunzio, L. I. Glazman, S. M. Girvin, M. H. Devoret, and R. J. Schoelkopf, "Observation of high coherence in Josephson junction qubits measured in a three-dimensional circuit QED architecture," *Phys. Rev. Lett.*, vol. 107, p. 240501, Dec 2011. [Online]. Available: http://link.aps.org/doi/10.1103/PhysRevLett.107.240501

[70] A. T. A. M. de Waele, "Basic operation of cryocoolers and related thermal machines," *Journal of Low Temperature Physics*, vol. 164, no. 5, p. 179, Jun 2011. [Online]. Available: https://doi.org/10.1007/s10909-011-0373-x

[71] C. Simon, M. Afzelius, J. Appel, A. Boyer de la Giroday, S. J. Dewhurst, N. Gisin, C. Y. Hu, F. Jelezko, S. Kröll, J. H. Müller, J. Nunn, E. S. Polzik, J. G. Rarity, H. De Riedmatten, W. Rosenfeld, A. J. Shields, N. Sköld, R. M. Stevenson, R. Thew, I. A. Walmsley, M. C. Weber, H. Weinfurter, J. Wrachtrup, and R. J. Young, "Quantum memories," *Eur. Phys. J. D*, vol. 58, pp. 1–22, 2010, 10.1140/epjd/e2010-00103-y. [Online]. Available: http://dx.doi.org/10.1140/epjd/e2010-00103-y

[72] K. Heshami, D. G. England, P. C. Humphreys, P. J. Bustard, V. M. Acosta, J. Nunn, and B. J. Sussman, "Quantum memories: emerging applications and recent advances," *Journal of modern optics*, vol. 63, no. 20, pp. 2005–2028, 2016.

[73] M. Rigol, V. Dunjko, and M. Olshanii, "Thermalization and its mechanism for generic isolated quantum systems," *Nature*, vol. 452, no. 7189, p. 854, 2008.

[74] M. Göppl, A. Fragner, M. Baur, R. Bianchetti, S. Filipp, J. Fink, P. Leek, G. Puebla, L. Steffen, and A. Wallraff, "Coplanar waveguide resonators for circuit quantum electrodynamics," *Journal of Applied Physics*, vol. 104, no. 11, p. 113904, 2008.

[75] D. Petrosyan, G. Bensky, G. Kurizki, I. Mazets, J. Majer, and J. Schmiedmayer, "Reversible state transfer between superconducting qubits and atomic ensembles," *Phys. Rev. A*, vol. 79, p. 040304, Apr 2009. [Online]. Available: http://link.aps.org/doi/10.1103/PhysRevA.79.040304

[76] S. Saito, X. Zhu, R. Amsüss, Y. Matsuzaki, K. Kakuyanagi, T. Shimo-Oka, N. Mizuochi, K. Nemoto, W. J. Munro, and K. Semba, "Towards realizing a quantum memory for a superconducting qubit: Storage and retrieval of quantum states," *Physical review letters*, vol. 111, no. 10, p. 107008, 2013.

[77] D. I. Schuster, A. P. Sears, E. Ginossar, L. DiCarlo, L. Frunzio, J. J. L. Morton, H. Wu, G. A. D. Briggs, B. B. Buckley, D. D. Awschalom, and R. J. Schoelkopf, "High-cooperativity coupling of electron-spin ensembles to superconducting cavities," *Phys. Rev. Lett.*, vol. 105, p. 140501, Sep 2010. [Online]. Available: http://link.aps.org/doi/10.1103/PhysRevLett.105.140501

[78] Y. Kubo, F. R. Ong, P. Bertet, D. Vion, V. Jacques, D. Zheng, A. Dréau, J.-F. Roch, A. Auffeves, F. Jelezko, J. Wrachtrup, M. F. Barthe, P. Bergonzo, and D. Esteve, "Strong coupling of a spin ensemble to a superconducting resonator," *Phys. Rev. Lett.*, vol. 105, p. 140502, Sep 2010. [Online]. Available: http://link.aps.org/doi/10.1103/PhysRevLett.105.140502

[79] R. Amsüss, C. Koller, T. Nöbauer, S. Putz, S. Rotter, K. Sandner, S. Schneider, M. Schramböck, G. Steinhauser, H. Ritsch, J. Schmiedmayer,

and J. Majer, "Cavity QED with magnetically coupled collective spin states," *Phys. Rev. Lett.*, vol. 107, p. 060502, Aug 2011. [Online]. Available: http://link.aps.org/doi/10.1103/PhysRevLett.107.060502

[80] P. C. Maurer, G. Kucsko, C. Latta, L. Jiang, N. Y. Yao, S. D. Bennett, F. Pastawski, D. Hunger, N. Chisholm, M. Markham, D. J. Twitchen, J. I. Cirac, and M. D. Lukin, "Room-temperature quantum bit memory exceeding one second," *Science*, vol. 336, no. 6086, pp. 1283–1286, 2012. [Online]. Available: http://www.sciencemag.org/content/336/6086/1283.abstract

[81] P. Bushev, A. K. Feofanov, H. Rotzinger, I. Protopopov, J. H. Cole, C. M. Wilson, G. Fischer, A. Lukashenko, and A. V. Ustinov, "Ultralow-power spectroscopy of a rare-earth spin ensemble using a superconducting resonator," *Phys. Rev. B*, vol. 84, p. 060501, Aug 2011. [Online]. Available: http://link.aps.org/doi/10.1103/PhysRevB.84.060501

[82] A. André, D. Demille, J. M. Doyle, M. D. Lukin, S. E. Maxwell, P. Rabl, R. J. Schoelkopf, and P. Zoller, "A coherent all-electrical interface between polar molecules and mesoscopic superconducting resonators," *Nat. Phys.*, vol. 2, no. 9, pp. 636–642, SEP 2006.

[83] A. Shalabney, C. Genet, G. Pupillo, J. George, J. Hutchison, and T. W. Ebbesen, "Coherent coupling of molecular resonators with a microcavity mode," *Nature communications*, vol. 6, p. 5981, 2015.

[84] A. G. Radnaev, Y. O. Dudin, R. Zhao, H. H. Jen, S. D. Jenkins, A. Kuzmich, and T. A. B. Kennedy, "A quantum memory with telecom-wavelength conversion," *Nat. Phys.*, vol. 6, pp. 894–899, Nov. 2010.

[85] Y. O. Dudin, R. Zhao, T. A. B. Kennedy, and A. Kuzmich, "Light storage in a magnetically dressed optical lattice," *Phys. Rev. A*, vol. 81, p. 041805, Apr 2010. [Online]. Available: http://link.aps.org/doi/10.1103/PhysRevA.81.041805

[86] H. P. Specht, C. Nölleke, A. Reiserer, M. Uphoff, E. Figueroa, S. Ritter, and G. Rempe, "A single-atom quantum memory," *Nature*, vol. 473, pp. 190–193, May 2011.

[87] M. Brune, S. Haroche, J. M. Raimond, L. Davidovich, and N. Zagury, "Manipulation of photons in a cavity by dispersive atom-field coupling: Quantum-nondemolition measurement and generation of schrödinger cat" states"," *Phys. Rev. A*, vol. 45, p. 5192, 1993.

[88] M. Brune, F. Schmidt-Kaler, A. Maali, J. Dreyer, E. Hagley, J. Raimond, and S. Haroche, "Quantum rabi oscillation: A direct test of field quantization in a cavity," *Physical review letters*, vol. 76, no. 11, p. 1800, 1996.

[89] S. Camerer, M. Korppi, A. Jöckel, D. Hunger, T. W. Hänsch, and P. Treutlein, "Realization of an optomechanical interface between ultracold

atoms and a membrane," *Phys. Rev. Lett.*, vol. 107, p. 223001, Nov 2011. [Online]. Available: http://link.aps.org/doi/10.1103/PhysRevLett.107.223001

[90] A. D. O'Connell, M. Hofheinz, M. Ansmann, R. C. Bialczak, M. Lenander, E. Lucero, M. Neeley, D. Sank, H. Wang, M. Weides, J. Wenner, J. M. Martinis, and A. N. Cleland, "Quantum ground state and single-phonon control of a mechanical resonator," *Nature*, vol. 464, pp. 697–703, Apr. 2010.

[91] A. A. Abdumalikov Jr, O. Astafiev, Y. Nakamura, Y. A. Pashkin, and J. Tsai, "Vacuum rabi splitting due to strong coupling of a flux qubit and a coplanar-waveguide resonator," *Physical review b*, vol. 78, no. 18, p. 180502, 2008.

[92] E. J. Pritchett and M. R. Geller, "Quantum memory for superconducting qubits," *Physical Review A*, vol. 72, no. 1, p. 010301, 2005.

[93] M. Mariantoni, H. Wang, T. Yamamoto, M. Neeley, R. C. Bialczak, Y. Chen, M. Lenander, E. Lucero, A. D. O'Connell, D. Sank *et al.*, "Implementing the quantum von neumann architecture with superconducting circuits," *Science*, vol. 334, no. 6052, pp. 61–65, 2011.

[94] Y. Kubo, C. Grezes, A. Dewes, T. Umeda, J. Isoya, H. Sumiya, N. Morishita, H. Abe, S. Onoda, T. Ohshima, V. Jacques, A. Dréau, J.-F. Roch, I. Diniz, A. Auffeves, D. Vion, D. Esteve, and P. Bertet, "Hybrid quantum circuit with a superconducting qubit coupled to a spin ensemble," *Phys. Rev. Lett.*, vol. 107, p. 220501, Nov 2011. [Online]. Available: https://link.aps.org/doi/10.1103/PhysRevLett.107.220501

[95] P. Rabl, D. DeMille, J. M. Doyle, M. D. Lukin, R. J. Schoelkopf, and P. Zoller, "Hybrid quantum processors: Molecular ensembles as quantum memory for solid state circuits," *Phys. Rev. Lett.*, vol. 97, p. 033003, Jul 2006. [Online]. Available: http://link.aps.org/doi/10.1103/PhysRevLett.97.033003

[96] Z.-L. Xiang, S. Ashhab, J. You, and F. Nori, "Hybrid quantum circuits: Superconducting circuits interacting with other quantum systems," *Reviews of Modern Physics*, vol. 85, no. 2, p. 623, 2013.

[97] D. Cano, B. Kasch, H. Hattermann, D. Koelle, R. Kleiner, C. Zimmermann, and J. Fortágh, "Impact of the meissner effect on magnetic microtraps for neutral atoms near superconducting thin films," *Phys. Rev. A*, vol. 77, p. 063408, Jun 2008. [Online]. Available: http://link.aps.org/doi/10.1103/PhysRevA.77.063408

[98] B. Kasch, H. Hattermann, D. Cano, T. E. Judd, S. Scheel, C. Zimmermann, R. Kleiner, D. Koelle, and J. Fortágh, "Cold atoms near superconductors: atomic spin coherence beyond the johnson noise limit," *New J. Phys.*, vol. 12, no. 6, p. 065024, 2010. [Online]. Available: http://stacks.iop.org/1367-2630/12/i=6/a=065024

[99] T. Nirrengarten, A. Qarry, C. Roux, A. Emmert, G. Nogues, M. Brune, J.-M. Raimond, and S. Haroche, "Realization of a superconducting atom chip," *Phys. Rev. Lett*, vol. 97, no. 20, p. 200405, 2006. [Online]. Available: http://link.aps.org/abstract/PRL/v97/e200405

[100] C. Roux, A. Emmert, A. Lupascu, T. Nirrengarten, G. Nogues, M. Brune, J. M. Raimond, and S. Haroche, "Bose-Einstein condensation on a superconducting atom chip," *Europhys. Lett.*, vol. 81, no. 5, p. 56004, 2008.

[101] T. Mukai, C. Hufnagel, A. Kasper, T. Meno, A. Tsukada, K. Semba, and F. Shimizu, "Persistent supercurrent atom chip," *Phys. Rev. Lett*, vol. 98, no. 26, p. 260407, 2007. [Online]. Available: http://link.aps.org/abstract/PRL/v98/e260407

[102] A. Emmert, A. Lupaşcu, M. Brune, J.-M. Raimond, S. Haroche, and G. Nogues, "Microtraps for neutral atoms using superconducting structures in the critical state," *Phys. Rev. A*, vol. 80, p. 061604, Dec 2009. [Online]. Available: http://link.aps.org/doi/10.1103/PhysRevA.80.061604

[103] C. Hufnagel, T. Mukai, and F. Shimizu, "Stability of a superconductive atom chip with persistent current," *Phys. Rev. A*, vol. 79, p. 053641, May 2009. [Online]. Available: http://link.aps.org/doi/10.1103/PhysRevA.79.053641

[104] F. Shimizu, C. Hufnagel, and T. Mukai, "Stable neutral atom trap with a thin superconducting disc," *Phys. Rev. Lett.*, vol. 103, p. 253002, Dec 2009. [Online]. Available: http://link.aps.org/doi/10.1103/PhysRevLett.103.253002

[105] S. Bernon, H. Hattermann, D. Bothner, M. Knufinke, P. Weiss, F. Jessen, D. Cano, M. Kemmler, R. Kleiner, D. Koelle, and J. Fortágh, "Manipulation and coherence of ultra-cold atoms on a superconducting atom chip," *Nat. Commun.*, vol. 4, Aug. 2013.

[106] B. Kasch, "Atomic spin coherence in superconductiong microtraps," Ph.D. dissertation, Universität Tübingen, 2010.

[107] S. Scheel, P. K. Rekdal, P. L. Knight, and E. A. Hinds, "Atomic spin decoherence near conducting and superconducting films," *Phys. Rev. A*, vol. 72, no. 4, p. 042901, 2005. [Online]. Available: http://link.aps.org/abstract/PRA/v72/e042901

[108] S. Scheel, R. Fermani, and E. A. Hinds, "Feasibility of studying vortex noise in two-dimensional superconductors with cold atoms," *Phys. Rev. A*, vol. 75, p. 064901, Jun 2007. [Online]. Available: http://link.aps.org/doi/10.1103/PhysRevA.75.064901

[109] R. Zhao, Y. O. Dudin, S. D. Jenkins, C. J. Campbell, D. N. Matsukevich, T. A. B. Kennedy, and A. Kuzmich, "Long-lived quantum memory," *Nat. Phys.*, vol. 5, pp. 100–104, Feb. 2009.

[110] D. Steck, "Rubidium 87 D line data," *http://steck.us/alkalidata*, Aug 2010. [Online]. Available: http://steck.us/alkalidata

[111] M. Hafezi, Z. Kim, S. L. Rolston, L. A. Orozco, B. L. Lev, and J. M. Taylor, "Atomic interface between microwave and optical photons," *Phys. Rev. A*, vol. 85, p. 020302, Feb 2012. [Online]. Available: http://link.aps.org/doi/10.1103/PhysRevA.85.020302

[112] H. J. Kimble, "The quantum internet," *Nature*, vol. 453, pp. 1023–1030, Jun. 2008.

[113] S. Ritter, C. Nölleke, C. Hahn, A. Reiserer, A. Neuzner, M. Uphoff, M. Mücke, E. Figueroa, J. Bochmann, and G. Rempe, "An elementary quantum network of single atoms in optical cavities," *Nature*, vol. 484, pp. 195–200, Apr. 2012.

[114] B. Zhao, Y.-A. Chen, X.-H. Bao, T. Strassel, C.-S. Chuu, X.-M. Jin, J. Schmiedmayer, Z.-S. Yuan, S. Chen, and J.-W. Pan, "A millisecond quantum memory for scalable quantum networks," *Nat. Phys.*, vol. 5, pp. 95–99, Feb. 2009.

[115] M. Fox, *Quantum Optics : An Introduction*, ser. Oxford Master Series in Physics. Oxford University Press, Oxford, 2006. [Online]. Available: http://books.google.de/books?id=Q-4dIthPuL4C

[116] J. Verdú, H. Zoubi, C. Koller, J. Majer, H. Ritsch, and J. Schmiedmayer, "Strong magnetic coupling of an ultracold gas to a superconducting waveguide cavity," *Phys. Rev. Lett.*, vol. 103, p. 043603, Jul 2009. [Online]. Available: http://link.aps.org/doi/10.1103/PhysRevLett.103.043603

[117] M. Mack, F. Karlewski, H. Hattermann, S. Höckh, F. Jessen, D. Cano, and J. Fortágh, "Measurement of absolute transition frequencies of ^{87}Rb to nS and nD rydberg states by means of electromagnetically induced transparency," *Phys. Rev. A*, vol. 83, p. 052515, May 2011. [Online]. Available: http://link.aps.org/doi/10.1103/PhysRevA.83.052515

[118] S. Haroche, "Cavity quantum electrodynamics: a review of rydberg atom-microwave experiments on entanglement and decoherence," in *AIP Conference Proceedings*, vol. 464, no. 1. AIP, 1999, pp. 45–66.

[119] P. Nordlander, "Energies and lifetimes of atomic rydberg states near metal surfaces," *Physical Review B*, vol. 53, no. 7, p. 4125, 1996.

[120] C. E. Theodosiou, "Lifetimes of alkali-metal—atom rydberg states," *Physical Review A*, vol. 30, no. 6, p. 2881, 1984.

[121] M. Mack, J. Grimmel, F. Karlewski, L. Sárkány, H. Hattermann, and J. Fortágh, "All-optical measurement of rydberg-state lifetimes," *Physical Review A*, vol. 92, no. 1, p. 012517, 2015.

[122] R. Unanyan, M. Fleischhauer, B. Shore, and K. Bergmann, "Robust creation and phase-sensitive probing of superposition states via stimulated raman adiabatic passage (stirap) with degenerate dark states," *Optics Communications*, vol. 155, no. 1-3, pp. 144–154, 1998.

[123] T. Chaneliere, D. Matsukevich, S. Jenkins, S.-Y. Lan, T. Kennedy, and A. Kuzmich, "Storage and retrieval of single photons transmitted between remote quantum memories," *Nature*, vol. 438, no. 7069, p. 833, 2005.

[124] D. G. England, K. A. Fisher, J.-P. W. MacLean, P. J. Bustard, R. Lausten, K. J. Resch, and B. J. Sussman, "Storage and retrieval of thz-bandwidth single photons using a room-temperature diamond quantum memory," *Physical review letters*, vol. 114, no. 5, p. 053602, 2015.

[125] R. Heidemann, U. Raitzsch, V. Bendkowsky, B. Butscher, R. Löw, L. Santos, and T. Pfau, "Evidence for coherent collective rydberg excitation in the strong blockade regime," *Physical Review Letters*, vol. 99, no. 16, p. 163601, 2007.

[126] T. Cubel, B. Teo, V. Malinovsky, J. R. Guest, A. Reinhard, B. Knuffman, P. Berman, and G. Raithel, "Coherent population transfer of ground-state atoms into rydberg states," *Physical Review A*, vol. 72, no. 2, p. 023405, 2005.

[127] J. Deiglmayr, M. Reetz-Lamour, T. Amthor, S. Westermann, A. De Oliveira, and M. Weidemüller, "Coherent excitation of rydberg atoms in an ultracold gas," *Optics communications*, vol. 264, no. 2, pp. 293–298, 2006.

[128] R. Folman, P. Krüger, D. Cassettari, B. Hessmo, T. Maier, and J. Schmiedmayer, "Controlling cold atoms using nanofabricated surfaces: atom chips," *Physical Review Letters*, vol. 84, no. 20, p. 4749, 2000.

[129] W. H"ansel, P. Hommelhoff, T. W. H"ansch, and J. Reichel, "Bose-einstein condensation in a microelectronic trap," *Nature*, vol. 413, p. 498, 2001.

[130] A. Haase, D. Cassettari, B. Hessmo, and J. Schmiedmayer, "Trapping neutral atoms with a wire," *Physical Review A*, vol. 64, no. 4, p. 043405, 2001.

[131] J. Reichel and V. Vuletic, *Atom Chips*. Wiley, 2011. [Online]. Available: https://books.google.de/books?id=IpBfSI7sS20C

[132] I. Wolff, *Coplanar Microwave Integrated Circuits*. Wiley, 2006. [Online]. Available: https://books.google.de/books?id=G7ls2iKLTpIC

[133] D. Cano, "Meissner effect in superconducting microtraps," Ph.D. dissertation, Universität Tübingen, 2008.

[134] M. M. Khapaev, M. Y. Kupriyanov, E. Goldobin, and M. Siegel, "Current distribution simulation for superconducting multi-layered structures," *Superconductor Science and Technology*, vol. 16, no. 1, p. 24, 2003. [Online]. Available: http://stacks.iop.org/0953-2048/16/i=1/a=305

[135] H. Hattermann, "Interfacing cold atoms and superconductors," Ph.D. dissertation, Universität Tübingen, 2013.

[136] D. Cano, H. Hattermann, B. Kasch, C. Zimmermann, R. Kleiner, D. Koelle, and J. Fortágh, "Experimental system for research on ultracold atomic gases near superconducting microstructures," *Eur. Phys. J. D*, vol. 63, pp. 17–23, Jun. 2011.

[137] S. Haroche and J. Raimond, *Exploring the Quantum: Atoms, Cavities, and Photons*, ser. Oxford graduate texts in mathematics. Oxford University Press, Oxford, 2006. [Online]. Available: http://books.google.de/books?id= QY6YuU-Qi-AC

[138] R. Doll and M. Näbauer, "Experimental proof of magnetic flux quantization in a superconducting ring," *Physical Review Letters*, vol. 7, no. 2, p. 51, 1961.

[139] P. Weiss, M. Knufinke, S. Bernon, D. Bothner, L. Sárkány, C. Zimmermann, R. Kleiner, D. Koelle, J. Fortágh, and H. Hattermann, "Sensitivity of ultracold atoms to quantized flux in a superconducting ring," *Phys. Rev. Lett.*, vol. 114, p. 113003, Mar 2015. [Online]. Available: http://link.aps.org/doi/10.1103/PhysRevLett.114.113003

[140] D. Bothner, M. Knufinke, H. Hattermann, R. Wölbing, B. Ferdinand, P. Weiss, S. Bernon, J. Fortágh, D. Koelle, and R. Kleiner, "Inductively coupled superconducting half wavelength resonators as persistent current traps for ultracold atoms," *New Journal of Physics*, vol. 15, no. 9, p. 093024, 2013.

[141] D. A. Smith, S. Aigner, S. Hofferberth, M. Gring, M. Andersson, S. Wildermuth, P. Krüger, S. Schneider, T. Schumm, and J. Schmiedmayer, "Absorption imaging of ultracold atoms on atom chips," *Opt. Express*, vol. 19, no. 9, pp. 8471–8485, Apr 2011. [Online]. Available: http://www.opticsexpress.org/abstract.cfm?URI=oe-19-9-8471

[142] *Atomic Physics*. Oxford University press, 2004.

[143] T. R. Gentile, B. J. Hughey, D. Kleppner, and T. W. Ducas, "Experimental study of one- and two-photon Rabi oscillations," *Phys. Rev. A*, vol. 40, pp. 5103–5115, Nov 1989. [Online]. Available: http://link.aps.org/doi/10.1103/PhysRevA.40.5103

[144] L. Sárkány, P. Weiss, H. Hattermann, and J. Fortágh, "Controlling the magnetic-field sensitivity of atomic-clock states by microwave dressing," *Phys. Rev. A*, vol. 90, p. 053416, Nov 2014. [Online]. Available: http://link.aps.org/doi/10.1103/PhysRevA.90.053416

[145] T. Schulte-Herbrüggen, A. Spörl, N. Khaneja, and S. Glaser, "Optimal control for generating quantum gates in open dissipative systems," *Journal of Physics B: Atomic, Molecular and Optical Physics*, vol. 44, no. 15, p. 154013, 2011.

[146] F. Dolde, V. Bergholm, Y. Wang, I. Jakobi, B. Naydenov, S. Pezzagna, J. Meijer, F. Jelezko, P. Neumann, T. Schulte-Herbrüggen *et al.*, "High-fidelity spin entanglement using optimal control," *Nature communications*, vol. 5, p. 3371, 2014.

[147] M. Gross and S. Haroche, "Superradiance: An essay on the theory of collective spontaneous emission," *Physics reports*, vol. 93, no. 5, pp. 301–396, 1982.

[148] W. Ketterle and S. Inouye, "Collective enhancement and suppression in bose–einstein condensates," *Comptes Rendus de l'Académie des Sciences-Series IV-Physics*, vol. 2, no. 3, pp. 339–380, 2001.

[149] K. Henschel, J. Majer, J. Schmiedmayer, and H. Ritsch, "Cavity QED with an ultracold ensemble on a chip: Prospects for strong magnetic coupling at finite temperatures," *Phys. Rev. A*, vol. 82, p. 033810, Sep 2010. [Online]. Available: http://link.aps.org/doi/10.1103/PhysRevA.82.033810

[150] A. Tauschinsky, R. M. T. Thijssen, S. Whitlock, H. B. van Linden van den Heuvell, and R. J. C. Spreeuw, "Spatially resolved excitation of rydberg atoms and surface effects on an atom chip," *Phys. Rev. A*, vol. 81, no. 6, p. 063411, Jun 2010.

[151] T. Y. Abi-Salloum, "Electromagnetically induced transparency and autler-townes splitting: Two similar but distinct phenomena in two categories of three-level atomic systems," *Physical Review A*, vol. 81, no. 5, p. 053836, 2010.

[152] M. Fleischhauer, A. Imamoglu, and J. P. Marangos, "Electromagnetically induced transparency: Optics in coherent media," *Rev. Mod. Phys.*, vol. 77, no. 2, pp. 633–673, Jul 2005.

[153] S. Khan, V. Bharti, and V. Natarajan, "Role of dressed-state interference in electromagnetically induced transparency," *Physics Letters A*, vol. 380, no. 48, pp. 4100–4104, 2016.

[154] P. M. Anisimov, J. P. Dowling, and B. C. Sanders, "Objectively discerning autler-townes splitting from electromagnetically induced transparency," *Physical review letters*, vol. 107, no. 16, p. 163604, 2011.

[155] M. L. Zimmerman, M. G. Littman, M. M. Kash, and D. Kleppner, "Stark structure of the rydberg states of alkali-metal atoms," *Physical Review A*, vol. 20, no. 6, p. 2251, 1979.

[156] J. Grimmel, M. Mack, F. Karlewski, F. Jessen, M. Reinschmidt, N. Sándor, and J. Fortágh, "Measurement and numerical calculation of rubidium rydberg stark spectra," *New Journal of Physics*, vol. 17, no. 5, p. 053005, 2015.

[157] H. Hattermann, M. Mack, F. Karlewski, F. Jessen, D. Cano, and J. Fortágh, "Detrimental adsorbate fields in experiments with cold rydberg gases near surfaces," *Phys. Rev. A*, vol. 86, p. 022511, Aug 2012. [Online]. Available: http://link.aps.org/doi/10.1103/PhysRevA.86.022511

[158] K. Chan, M. Siercke, C. Hufnagel, and R. Dumke, "Adsorbate electric fields on a cryogenic atom chip," *Physical review letters*, vol. 112, no. 2, p. 026101, 2014.

[159] F. Robicheaux, C. Wesdorp, and L. Noordam, "Selective field ionization in li and rb: Theory and experiment," *Physical Review A*, vol. 62, no. 4, p. 043404, 2000.

[160] A. Gürtler and W. van der Zande, "l-state selective field ionization of rubidium rydberg states," *Physics Letters A*, vol. 324, no. 4, pp. 315–320, 2004.

[161] C. Hermann-Avigliano, R. C. Teixeira, T. Nguyen, T. Cantat-Moltrecht, G. Nogues, I. Dotsenko, S. Gleyzes, J. Raimond, S. Haroche, and M. Brune, "Long coherence times for rydberg qubits on a superconducting atom chip," *Physical Review A*, vol. 90, no. 4, p. 040502, 2014.

[162] E. Alexandrov, M. Balabas, D. Budker, D. English, D. Kimball, C.-H. Li, and V. Yashchuk, "Light-induced desorption of alkali-metal atoms from paraffin coating," *Physical Review A*, vol. 66, no. 4, p. 042903, 2002.

[163] L. Jones, J. Carter, and J. Martin, "Rydberg atoms with a reduced sensitivity to dc and low-frequency electric fields," *Physical Review A*, vol. 87, no. 2, p. 023423, 2013.